ULB

ECOLE
POLYTECHNIQUE
DE BRUXELLES

Optimization of the implementation of JUNO's real-time core-collapse supernovae monitor

Rosso Félix

Director
Prof. Nicolas Pauly

Co-Director
Prof. Barbara Clerbaux

Supervisor
Dr. Marta Colomer Molla

Academic year
2024–2025

In order to be awarded the Master's programme in
Physics Engineering

Abstract

Félix Rosso

Master of Science in Physics Engineering

Université Libre de Bruxelles – École Polytechnique de Bruxelles

2024–2025

Optimization of the implementation of JUNO's real-time core-collapse supernovae monitor

The detection of core-collapse supernovae (CCSN) via neutrinos provides an opportunity to study the explosion dynamics and trigger an early alert for the following light signal. Even though neutrinos interact extremely weakly with matter, the Jiangmen Underground Neutrino Observatory (JUNO), with its large target medium and excellent energy resolution, makes it an ideal detector for CCSN neutrinos. The neutrino signal is estimated by a $13M_\odot$ CCSN simulation, using the Nakazato model, coupled with a simulation of the IBD channel of JUNO and the electronic response. The background, mainly due to atmospheric muons, is estimated from the data recorded during the commissioning phase of JUNO.

To maximize the real-time detector detector's efficiency, several techniques are used to favor the CCSN signal compared to the background. Their energy spectrum is computed using a mean rate, from hours of data-taking periods and a large number of CCSN simulations, providing statistically good results. Two veto systems of JUNO are under study. The first one cuts secondary interactions by suppressing any hits occurring shortly after (60 μs) a high energy signal is recorded. The second veto uses the water Cherenkov pool of JUNO to tag muons and prevent any corresponding signal in the central detector to be recorded. Then, we introduce two methods to select optimally the energy range and a sliding window method whose parameters are optimized to favor the time characteristics of the CCSN signal. Lastly, a non linear regression on data samples of several days is used to estimate the maximum number of events in a month, due to background. The CCSN threshold is set above this maximum, to ensure less than one false alert per month. The Table 5.1 summarize the results of this work, by showing the CCSN threshold for the two energy range methods and three filling levels of liquid scintillator in the central detector.

Keywords: neutrino physics, JUNO detector, core-collapse supernovae, signal processing, real-time monitoring.

Acknowledgment

I would first like to thank Pr. Barbara Clerbaux for her advice, expertise, and enthusiasm for my work, as well as for helping me take my first steps in the academic field.

Next, I want to thank Pr. Nicolas Pauly for giving me the opportunity to take this master thesis, and for his support during this year.

Last but not least, I would like to address my sincere gratitude to my supervisor Dr. Marta Colomer Molla who helped me in every aspect of this thesis, from the start to the very end and for being continuously available.

Context

The observation of neutrinos from Supernova 1987A confirmed the neutrino-driven nature of core-collapse supernova (CCSN) explosion. Indeed, neutrinos from the Supernova 1987A were detected approximately three hours before the first photons reached Earth. This early signal, offers an opportunity: the possibility of alerting the astronomical community to be ready to observe the light signal when it reaches the Earth.

The Jiangmen Underground Neutrino Observatory (JUNO), currently at the end of its commissioning phase, combines a large target medium, high energy resolution, and efficient veto systems. While JUNO's primary objective is to determine the neutrino mass ordering, its design also makes it a great instrument for detecting the neutrino burst produced by CCSNe. Such a phenomenon happening in our galaxy would generate thousands of interactions events in JUNO within seconds.

The CCSN detection system will allow JUNO to be part of the Supernova Early Warning System (SNEWS), along with other neutrino detectors and gravitational-wave observatories.

Beyond the immediate application to CCSN alerts, the methods and results shown in this work, especially the energy distribution plots of neutrinos and background, will be of benefit to the JUNO's community.

Contents

Introduction

The standard model of particle physics (SM) is one of the greatest achievement of modern physics. It gives a framework for the three fundamental forces (electromagnetic, strong and weak forces) and all discovered particles. However, one family of particle still raises many questions : the neutrino. Neutrino exists in three flavors and can change their flavor while traveling in space-time. This process, called the neutrino oscillation phenomenon, solved the solar neutrino problem and implies that neutrinos are not massless, which was not accounted when the SM was built. Along with other observations, this opened the research for beyond SM physics. The key unknown parameter of neutrinos is their masses which we only know upper and lower bounds. Another property of neutrinos that remains unknown is the neutrino mass ordering, which the JUNO experiment aims to determine.

The Jiangmen Underground Neutrino Observatory (JUNO) is a medium-baseline liquid scintillator neutrino detector located in China, buried 700 meters underground and at 53 km from two nuclear power plants. JUNO aims to determine the neutrino mass ordering over six years of data collection, from reactor antineutrinos $\bar{\nu}_e$, by precisely measuring the oscillation pattern differences of both possible ordering. In addition to reactor $\bar{\nu}_e$, JUNO is also sensitive to other neutrino sources, enabling the study of other phenomena. Among these sources are core-collapse supernovae (CCSN), which are particularly interesting from a neutrino physics perspective, as they release approximately 99% of their energy in the form of neutrinos of all flavors.

CCSN are one of the biggest known cataclysmic phenomenon in the universe. It marks the end of the heavy star lives which occur when gravitational forces overcome the outward pressures. During the collapse, the core's temperature and density increase quickly, which trigger electron capture and generate an enormous neutrino flux, detectable on Earth. To predict the detection rate and energy spectrum of CCSN neutrinos, several simulations have been developed. The rate of CCSN happening close enough that we can detect them via neutrino is dominated by the CCSN rate in our galaxy. However smaller star clusters have a non negligible probability of triggering CCSN at distances up to approximately 60 kpc, in the small Magellan cloud. Our goal is therefore to be able to detect in real-time, a CCSN via neutrinos happening up to 60 kpc from the Earth.

The master thesis is organized as follows. In the first chapter a summary of the standard model of particle physics is given. The neutrino sector is further described and the actual knowledge of neutrino parameters is presented. The Chapter 2 introduces the JUNO experiment, first with an overview of the goals and the architecture of the detectors and then with the possible interactions of neutrinos, atmospheric muons and terrestrial radioactivity, taking place in the active volume. We continue by describing the CCSN phenomenon from a neutrino-emission point of view and the existing simulations, in Chapter 3. The Chapter 4 studies the tools to favor the

CCSN neutrino detections compared to the background. The energy distributions of both the CCSN simulation and the background are plotted. The effects of two veto methods, which aims to reduce the background while nearly not affecting the signal, are analyzed. The last chapter concludes this work by explaining how to build the real-time CCSN monitor, based on the results found in the previous chapter and implementing of a sliding window method.

Chapter 1

The Standard Model & neutrinos

This first chapter dives into the theoretical description of neutrinos. We start by introducing the basic notions of the Standard Model of particle physics and then a complete description of neutrino physics is done. Lastly, a picture of the actual knowledge of neutrino parameters is given.

The notions explained in this chapter are inspired by [1] and [2].

1.1 The standard model of particle physics

The Standard Model (SM) of particle physics is the theoretical framework that currently provides the most complete and experimentally verified description of the fundamental particles and their interactions, without gravity (the latter being described by the theory of general relativity). Developed through the mid-20th century and finalized by the 1970s, the SM uses quantum field theory with the principle of local gauge invariance. The current classification of the elementary particles constituting the SM is represented in Fig. 1.1 (without antimatter).

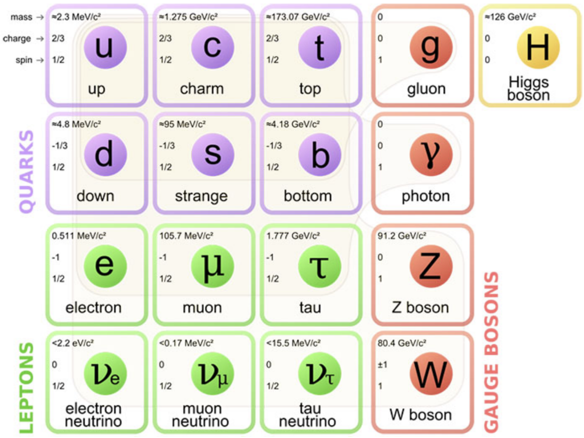

Figure 1.1: Standard Model of particle physics with the three generations of fermions (first three column), the gauge bosons (4th column) and the Higgs boson (5th column). Taken from [3].

The SM classifies all experimentally discovered elementary particles into two categories : fermions and bosons. Fermions are the elementary constituents of matter. They are divided into two subgroups : quarks and leptons. Each group contains six particles, organized in three generations. The first generation includes the up (u) and down (d) quarks, the electron (e^-), and the electron neutrino (ν_e); the second contains the charm (c) and strange (s) quarks, the muon (μ), and the muon neutrino (ν_μ); and the third is made of the top (t) and bottom (b) quarks, the tau (τ), and the tau neutrino (ν_τ). There are thus 3 types of neutrinos which are called flavors. Each fermion also has a corresponding antiparticle with the same mass and spin but opposite quantum numbers (electric charge,...), and are noted with hat. For example the antiparticle of the up quark u, is noted : $\bar{u}$. Stable matter is entirely made of the fermions of the first generation, without the neutrino. The up and down quarks form protons (uud) and neutrons (udd), which together constitute atomic nuclei. Combined with electrons, they make up all atoms.

The dynamics and interactions among these particles are governed by the exchange of bosons, which act as mediators of the fundamental forces. The electromagnetic interaction is mediated by the photon (γ), the weak interaction by the W^+,W^-, and Z^0 bosons, and the strong interaction by eight types of massless gluons (g). These interaction-mediating bosons emerge naturally from the gauge symmetry principles, each of them presenting symmetries of different groups : $U(1)$ for electromagnetism, $SU(2)$ for the weak force, and $SU(3)$ for the strong force [4].

The last particles of the SM is the Higgs boson, which embed the Higgs mechanism. This theoretical mechanism allowed to build the electroweak theory with massive W and Z boson, by introducing the existence of a Higgs field. Through spontaneous symmetry breaking, elementary massive particles (including the Higgs boson) get their masses from their interaction with this field [5, 6, 7]. The Higgs boson has been discovered in 2012 at CERN, confirming this theory [8].

Despite its success in describing a vast range of phenomena with remarkable precision, the Standard Model has known limitations. Three observations could not be explained by the SM : the evidence of massive neutrinos, the matter/antimatter asymmetry and the presence of dark matter in the universe. The SM can be naturally extended to account for massive neutrinos (see section 1.2.3) but the other two observations are currently open problems in physics. Also, it does not contain the gravitation which prevents it from being a theory of everything.

1.2 Neutrinos physics

Neutrinos are among the most mysterious particles of the SM. First of all, they are only sensitive to the weakest of the three interactions described by the SM : the weak interaction. This implies that neutrinos interact extremely weakly with matter. For example, billions of neutrinos pass through our body every second, without interacting [9]. In comparison, it require 2.5 cm of skin to stop a 5 MeV electron (going at 99% of the speed of light), resultin in skin burn [10].
Their second characteristic, which is related to the first one, is that neutrinos are the only particles in the SM whose exact masses remain undetermined. A quick look at the Figure 1.1 shows us that we know upper bounds and we will also see a method to define a lower bound in the last section of this chapter.

1.2.1 Neutrinos flavors

Neutrinos exist in three flavors, and their production is always associated with the corresponding charged leptons.

Electron neutrinos - history of beta decay

The neutrino's history is tightly related to the β decay. For nuclei presenting a proton/neutron imbalance, the β decay is a convenient way to stabilize by transforming one into another through the weak interaction. The charge conservation implies the intervention in the process of a charged particle : electron or positron. Before the discovery of neutrinos, the β decay was described by Eq. 1.1.

$$\beta^- : n \rightarrow p^+ + e^- \qquad \beta^+ : p^+ \rightarrow n + e^+ \tag{1.1}$$

In 1911, Lise Meitner and Otto Hahn performed an experiment which showed that the energy of the electrons emitted by beta decay had a continuous rather than discrete spectrum which was in contradiction with energy conservation. The solution for this energy loss was proposed by Wolgang Pauli in 1930. He suggested that another extremely light particle, undetectable at the time, was emitted during β decay, taking away the missing energy. He called this particle the neutron, but it was later renamed neutrino (little neutron in Italian) by Enrico Fermi [11].

$$\beta^- : n \rightarrow p^+ + e^- + \bar{\nu}_e \qquad \beta^+ : p^+ \rightarrow n + e^+ + \nu_e \tag{1.2}$$

The total energy of the β decay is thus shared between the electron/positron and the antineutrino/neutrino which explains the continuous behavior of the energy spectrum.
We know now from the SM that the β decay process is possible by transforming a down quark into a up quark and vice versa ($d \leftrightarrow u$), through the weak interaction, more precisely its first type : Charged Current (CC), mediated by the $W^\pm$ boson.

$$\beta^- : d \rightarrow u + W^- \rightarrow u + e^- + \bar{\nu}_e \qquad \beta^+ : u \rightarrow d + W^+ \rightarrow d + e^+ + \nu_e \tag{1.3}$$

The other type of weak interaction, mediated by the Z boson, is called the Neutral Current (NC) and in the context of neutrino, consists of elastic scattering reactions. For example :

$$\nu_e + p \xrightarrow{Z} \nu_e + p \tag{1.4}$$

Muon and tau neutrinos

Unlike the electron neutrino ν_e, the muon neutrino ν_μ and the tau neutrino ν_τ are very unlikely to appear in most nuclear processes, because their associated leptons (muon μ and tau τ) are too heavy and thus require more energy (the energy needed to create a particle is given by the famous formula $E = mc^2$). Indeed, the natural nuclear processes release typically less than $Q = 10$ MeV (fission releases about $Q = 200$ MeV in total but from a huge number of smaller processes which are each releasing less than $Q_i = 10$ MeV) [12]. In comparison, the mass of the μ is 105.7 MeV and 1777 MeV for the τ. These energies are reached only in cosmic events (cf. discovery of muon [13]) and in particles colliders (cf. discovery of tau at SLAC with SPEAR collider [14]).

1.2.2 Neutrino oscillation phenomenon

The neutrino oscillation phenomenon is the discovery which solved the solar neutrino problem and implies that at least two of three flavors are massive.

The solar neutrino problem

The first large scale cosmic neutrino detector was build in the late 1960's and is called the Homestake experiment [15]. It aimed to study the thermonuclear reactions in the sun's core by analyzing the neutrinos flux produced through the p-p cycle [16] (Eq. 1.5).

$$4p^+ \to {}^4\mathrm{He}^{2+} + 2e^+ + 2\nu_e \tag{1.5}$$

The results of this experience showed a measured neutrino flux about 1/3 lower than the theoretically predicted one [17]. This problem is called the solar neutrinos problem and led to the discovery of neutrino oscillations.

Neutrino oscillations phenomenon

The neutrino oscillations phenomenon, proposed by Bruno Pontecorvo, suggests that neutrinos change their flavors while traveling in space ($\nu_e \leftrightarrow \nu_\mu$ for example). He first proposed a theory in 1957 where neutrino can transform into anti-neutrino [18], then after the discovery of muon neutrino, extended his idea to flavor oscillation in 1967 [19]. This phenomenon was confirmed by the Super-Kamiokande (SK) project [20], by showing that the proportion of flavors were varying for different traveled distance of atmospheric neutrinos and by the Sudbury Neutrino Observatory (SNO) in 2002 [21], by showing that the solar neutrinos flux of all flavors (e, μ, τ) corresponds to the theoretically calculated proportion of electron neutrinos ν_e produced by the sun. Leaders of both projects jointly received the Physics Nobel Prize in 2015 for the experimental proof of neutrino oscillations.

Let us dig into the theoretical formalism of neutrino oscillations. Neutrinos are created and interact in flavor (e, μ, τ) eigenstates, which are each actually a superposition of three mass eigenstates (ν_1, ν_2, ν_3). Let us imagine a neutrino propagating through space, the quantum phases of these three different mass states evolve as $|\nu_i(t)\rangle = e^{-\frac{iE_i t}{\hbar}}|\nu_i\rangle$, where E_i is the energy of the neutrinos of each mass state. If the masses of the 3 states (m_1, m_2 and m_3) are different, the corresponding energies E_i will also be different and therefore, these three states will evolve at different speeds causing the neutrino's global mass state superposition to change over time. Since different combinations of mass states correspond to different combinations of flavor states, as the neutrino propagates, the changing mass states also cause the global flavor state to change. The state of a neutrino can thus be expressed in the flavor-eigenstates as a function of the mass-eigenstates and vice versa with a basis change through the PMNS (Pontecorvo-Maki-Nakagawa-Sakata) matrix $\mathcal{U}$ which we will detail later.

1.2.3 Mass of neutrinos - theory and measurement

Dirac mass

In the SM formalism, fermions are called Dirac particles and get their masses from their interaction with the Higgs field. For the charged leptons, this interaction is described by the Yukawa Lagrangian. If neutrinos are Dirac particles, the SM need to be corrected by admitting that neutrino have a sterile right-handed component $\nu_{iR}(x)$. In this case, their Yukawa Lagrangian after spontaneous symmetry breaking and standard diagonalization writes (see Appendix A.3.1):

$$\mathcal{L}_Y(x) = -\sum_{i=1}^{3} m_i \bar{\nu}_{iL}(x)\nu_{iR}(x) + \text{h.c.} \tag{1.6}$$

where ν_{iL} and ν_{iR} are the left-handed and right-handed fields of the neutrinos and i are the mass states $\nu_i = (\nu_1, \nu_2, \nu_3)$. From this formalism, the mass is expressed as $m_i = y_i v$, where the

Yukawa constant y_i quantifies the interaction strength of the particle with the Higgs field and v is the Higgs vacuum expectation value (vev).

Formally, neutrinos can be described as Dirac particles and generate their masses from the Higgs mechanism. However their Yukawa constants would be more than 10 orders of magnitude smaller than for the other particles of their respective family [22]. Therefore, it is plausible that neutrinos get their masses from another process.

Majorana mass

Ettore Majorana proposed a theory to describe fermions that are their own antiparticles, having therefore only left-handed field $\psi_L(x)$. The mass giving interaction is described by the Majorana Lagrangian, here for neutrinos (see Appendix A.3.1) :

$$\mathcal{L}_Y = -\frac{1}{2}\sum_{i=1}^{3} m_i \bar{\nu}_i \nu_i \tag{1.7}$$

$$\nu_i = \sum_{l'} U^\dagger_{il} \nu_{lL} + \sum_{l'} (U^\dagger_{il} \nu_{lL})^c \tag{1.8}$$

where $U^\dagger$ is the diagonalization matrix. Let us note that this Lagrangian doesn't conserve the total lepton number, by allowing a neutrino to turn into an antineutrino, which changes the total lepton number by 2, explicitly violating its conservation.

If neutrinos are Majorana particles, neutrinos are their own antiparticles and $\nu_i = \bar{\nu}_i$. From this, we know that charged particles cannot be Majorana as they differ from their associated antiparticle through the charge (example : the electron $e^- \neq e^+$). Neutrinos are the only known particles that can be described by this formalism since they are the only electrically neutral fermions in the SM. To demonstrate the Majorana nature of neutrinos, researchers are looking for processes that violate lepton number conservation, such as neutrinoless double beta decay ($0\nu\beta\beta$) [23]. To date, no such process has been observed.

Experimental measures

Experimentally, the direct measurement of the neutrino masses poses serious challenges as they interact only via the weak interactions and that they are much lighter than any other known particles (the mass of heavy particles can be measured in collider, like the W boson [24]). Other methods have been developed to estimate the neutrino mass, in particular three main ones [25] :

1. Kinematic of beta decay : We saw previously on this chapter that beta decay generates an electron and an outgoing electron-flavored neutrino. By measuring the energy distribution of the outgoing electrons, we can build the source spectrum and compare it with the Fermi's beta decay model spectrum (which consider neutrino being massless) [12]. Fitting the parameters, both spectrum will differ at the maximum energy, the source spectrum being reduced by the neutrino mass energy $E_{\text{max}} = E^{\text{Fermi}}_{\text{max}} - m_{\nu_e}c^2$, allowing to extract the electron neutrino mass. The challenges of this method is the high energy resolution and large statistics needed due to the smallness of m_{ν_e}, but it does not depend on any assumptions. The best results are from the KATRIN experiment [26] and give the constraint $m_{\nu_e} < 0.45$ eV at 90% confidence. This method cannot be used for the other flavors.

2. Cosmology : This method studies how neutrinos mass would affect the formation and the expansion history of the universe and compare it to our models. The primary observable

is the sum of neutrino masses: $M_\nu = \sum_i m_i$. This methods gives, at 95% confidence, the strong upper bound $M_\nu < 0.072$ eV (normal ordering[1]) and $M_\nu < 0.113$ eV (inverted ordering) but presents a strong model dependence and cannot estimate individual flavors neutrino masses [27].

3. Supernovae time-of-flight dispersion : This method uses the fact that massive neutrinos travel slightly slower than light speed and that the dispersion in time-of-arrival of neutrinos from a single source is dependent on neutrino mass. By observing the spread in arrival times of neutrinos from a CCSN explosion, depending on the CCSN model and the precision of the distance measurement, constraints can be placed on neutrino mass. The result from the Supernova 1987A is : $m_{\nu_e} < 5.7$ eV at 95% confidence. For now, this method seems not optimal due to the weak resulting constraint but with recent detectors, if a CCSN happens close to the Earth, it could give significantly better results.

1.2.4 The PMNS matrix

The PMNS matrix $\mathcal{U}$, also called the neutrino mixing matrix, allows to link the flavor-eigenstates to the mass-eigenstates such that :

$$\begin{aligned}
|\nu_e(t)\rangle &= \mathcal{U}_{e1}|\nu_1(t)\rangle + \mathcal{U}_{e2}|\nu_2(t)\rangle + \mathcal{U}_{e3}|\nu_3(t)\rangle \\
|\nu_\mu(t)\rangle &= \mathcal{U}_{\mu1}|\nu_1(t)\rangle + \mathcal{U}_{\mu2}|\nu_2(t)\rangle + \mathcal{U}_{\mu3}|\nu_3(t)\rangle \\
|\nu_\tau(t)\rangle &= \mathcal{U}_{\tau1}|\nu_1(t)\rangle + \mathcal{U}_{\tau2}|\nu_2(t)\rangle + \mathcal{U}_{\tau3}|\nu_3(t)\rangle
\end{aligned} \tag{1.9}$$

The expression of $\mathcal{U}$ can be derived from the weak interaction Lagrangian [28]. A convenient parameterization of this matrix, in the case of Dirac neutrinos writes :

$$\mathcal{U}^D = \begin{pmatrix} c_{12}c_{13} & s_{12}c_{13} & s_{13}e^{-i\delta_{\mathrm{CP}}} \\ -s_{12}c_{23} - c_{12}s_{23}s_{13}e^{i\delta_{\mathrm{CP}}} & c_{12}c_{23} - s_{12}s_{23}s_{13}e^{i\delta_{\mathrm{CP}}} & s_{23}c_{13} \\ s_{12}s_{23} - c_{12}c_{23}s_{13}e^{i\delta_{\mathrm{CP}}} & -c_{12}s_{23} - s_{12}c_{23}s_{13}e^{i\delta_{\mathrm{CP}}} & c_{23}c_{13} \end{pmatrix} \tag{1.10}$$

where $c_{ab} = \cos\theta_{ab}$ and $s_{ab} = \sin\theta_{ab}$. With this parameterization, $\mathcal{U}^D$ contains 4 parameters: the three mixing angles $\theta_{12}, \theta_{13}, \theta_{23}$ and the Dirac phase δ_{CP} linked to the amount of CP-violation in the neutrino sector.

If neutrinos prove to be Majorana particles, the PMNS matrix of Majorana neutrinos need to take two additional CP-violating phases, called Majorana phases. In this case, the Dirac PMNS matrix is thus multiplied by a diagonal unitary matrix D^M containing these two Majorana phases.

$$\mathcal{U}^M = \mathcal{U}^D D^M \tag{1.11}$$

Further explanations of the information presented here is provided in Appendix A.3.2.

The parameters of $\mathcal{U}$ can be found through the measurement of neutrino oscillation phenomenon. We will now derive the two-flavor neutrino oscillation situation to give the necessary physical intuition while keeping the calculation short, before presenting the three-flavor case.

Two-flavors neutrino oscillation

We consider here the oscillation phenomenon between the electron neutrino ν_e and the muon neutrino ν_μ with two mass eigenstates. In this case, the mixing matrix can be understood as a

---

[1] The ordering of neutrinos mass eigenstates is not known and can be either normal ($m_3 \gg m_2 > m_1$) or inverted ($m_3 \ll m_1 < m_2$). The neutrino mass ordering problem is detailed ch. 1.3.2

2D rotation of angle θ between the flavor-basis and the mass-basis:

$$U^{2\times 2} = \begin{pmatrix} \cos\theta & \sin\theta \\ -\sin\theta & \cos\theta \end{pmatrix} \tag{1.12}$$

The oscillation equations 1.9 becomes:

$$\begin{aligned} |\nu_e(t)\rangle &= \cos\theta|\nu_1(t)\rangle + \sin\theta|\nu_2(t)\rangle \\ |\nu_\mu(t)\rangle &= -\sin\theta|\nu_1(t)\rangle + \cos\theta|\nu_2(t)\rangle \end{aligned} \tag{1.13}$$

In order to highlight the neutrino oscillation, let us consider a neutrino generated in the electron flavor eigenstate: $|\nu_e(0)\rangle = |1\rangle$ and $|\nu_\mu(0)\rangle = |0\rangle$. Inverting Eq. 1.13, we get:

$$\begin{aligned} |\nu_1(0)\rangle &= \cos\theta|1\rangle - \sin\theta|0\rangle = \cos\theta|1\rangle \\ |\nu_2(0)\rangle &= \sin\theta|1\rangle + \cos\theta|0\rangle = \sin\theta|1\rangle \end{aligned} \tag{1.14}$$

Where the empty state $|0\rangle$ is removed because it represents nothing physically.
In the ultra relativistic domain $v \sim c$ and $p_i c \gg m_i c^2$, the neutrino state evolves as [29]:

$$|\nu_i(t)\rangle = e^{\frac{-iE_i t}{\hbar}}|\nu_i(0)\rangle \tag{1.15}$$

where $E_i = \sqrt{p_i^2c^2 + m_i^2c^4} \approx p_i c\left(1 + \frac{1}{2}\frac{m_i^2c^2}{p_i^2}\right)$.
Injecting Eq. 1.15 in the second equation of 1.13, the muon flavor state evolve as:

$$\begin{aligned} |\nu_\mu(t)\rangle &= -\sin\theta\, e^{\frac{-iE_1 t}{\hbar}}|\nu_1(0)\rangle + \cos\theta\, e^{\frac{-iE_2 t}{\hbar}}|\nu_2(0)\rangle \\ &= -\sin\theta\, e^{\frac{-iE_1 t}{\hbar}}\cos\theta|1\rangle + \cos\theta\, e^{\frac{-iE_2 t}{\hbar}}\sin\theta|1\rangle \\ &= \frac{1}{2}\sin(2\theta)\left(e^{\frac{-iE_2 t}{\hbar}} - e^{\frac{-iE_1 t}{\hbar}}\right)|1\rangle \end{aligned} \tag{1.16}$$

Using the Born rule, we can find the probability of measuring our neutrino in the muon flavor at time t:

$$P_{\nu_e\to\nu_\mu}(t) = |\langle\nu_e(0)|\nu_\mu(t)\rangle|^2 = \frac{1}{4}\sin^2(2\theta)\left|e^{\frac{-iE_2 t}{\hbar}} - e^{\frac{-iE_1 t}{\hbar}}\right|^2 = \sin^2(2\theta)\sin^2\left(\frac{E_2 - E_1}{2\hbar}t\right) \tag{1.17}$$

Injecting the expression of E_i for ultra relativistic neutrino, assuming $p_1 \approx p_2 = p$:

$$P_{\nu_e\to\nu_\mu}(t) = \sin^2(2\theta)\sin^2\left(\frac{m_2^2 - m_1^2}{4\hbar p}c^3 t\right) \tag{1.18}$$

At last, we substitute $L \approx ct$ and $p = \frac{E}{c}$ where E is the average neutrino energy, as well as injecting the constant's numerical values and using the system of units: $[m] = \frac{eV}{c^2}$, $[E] = GeV$ and $[L] = km$:

$$P_{\nu_e\to\nu_\mu}(L) = \sin^2(2\theta)\sin^2\left(1.27\frac{\Delta m^2 L}{E}\right) \tag{1.19}$$

where $\Delta m^2 = m_2^2 - m_1^2$ and θ are the 2-flavors neutrino oscillation parameters.
The probability of measuring the neutrino in the muon flavor varies periodically with the propagation distance L, as shown in Fig. 1.2 (with fixed energy and oscillations parameters).
Let us note that if $\theta = 0$ or $\Delta m^2 = 0$, $P_{\nu_e\to\nu_\mu}(L) = 0, \forall L$: we wouldn't observe neutrino oscillation. We can conclude that $\theta \neq 0$ which implies that the mass states must be different

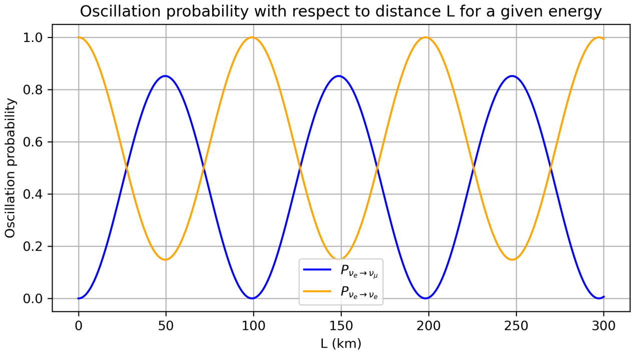

Figure 1.2: Plot of the 2-flavors oscillation probability from ν_e to ν_μ with the distance L (km). The parameters: $\theta = \theta_{12}$ and $\Delta m^2 = \Delta m^2_{21}$ are taken from Table 1.1 and $E = 3 \cdot 10^{-3}$ GeV.

from the flavor states and $\Delta m^2 \neq 0$ which implies that the mass states are different and thus at least one mass is different than zero.

Three-flavors neutrino oscillation

Now that we set the intuition of the neutrino oscillation phenomenon, we can calculate the three-flavors oscillation probability of a neutrino created in flavor α to be measured at distance L from the source, in the flavor β. We use the same formula but with the 3×3 PMNS matrix:

$$P_{\nu_\alpha \to \nu_\beta}(L) = |\langle \nu_\alpha(0) | \nu_\beta(t) \rangle|^2 = \left| \sum_{i=1}^{3} \mathcal{U}^*_{\alpha i} \mathcal{U}_{\beta i} e^{-i m_i^2 \frac{L}{2E}} \right|^2 \tag{1.20}$$

Since α and β can each take 3 values, a source emitting neutrinos of all flavors will be described by 9 oscillation probability equations. Because these equations have similar forms, we give the survival probability of the ν_e propagating at a distance L, to illustrate the phenomenon (using the same unit system as for Eq. 1.19 $[m] = \frac{eV^2}{c^4}$, $[E] = GeV$ and $[L] = km$) :

$$P_{\nu_e \to \nu_e}(L) = P_{\nu_e \to \nu_e}(L) = |\langle \nu_e(0) | \nu_e(t) \rangle|^2 = \left| \sum_{i=1}^{3} \mathcal{U}^*_{ei} \mathcal{U}_{ei} e^{-i m_i^2 \frac{L}{2E}} \right|^2 \tag{1.21a}$$

$$\begin{aligned} &= 1 - \sin^2(2\theta_{12}) \cos^4 \theta_{13} \sin^2 \left(1.27 \frac{\Delta m^2_{21} L}{E} \right) \\ &\quad - \sin^2(2\theta_{13}) \left[\cos^2 \theta_{12} \sin^2 \left(1.27 \frac{\Delta m^2_{31} L}{E} \right) + \sin^2 \theta_{12} \sin^2 \left(1.27 \frac{\Delta m^2_{32} L}{E} \right) \right] \end{aligned} \tag{1.21b}$$

From neutrino parameters measurements (cf. section 1.3), we can simplify the expression of Eq. 1.21b, using $\Delta m^2_{21} \ll \Delta m^2_{31}, \Delta m^2_{32}$, which allows to write the survival probability in terms of a fast oscillation $\Delta m^2_{31} \approx \Delta m^2_{32} = \Delta m^2_{\text{fast}}$ and a slow oscillation $\Delta m^2_{\text{slow}} = \Delta m^2_{21}$ (Eq. 1.22):

$$\begin{aligned} P_{\nu_e \to \nu_e}(L) &\approx 1 - \sin^2(2\theta_{12}) \cos^4 \theta_{13} \sin^2 \left(1.27 \frac{\Delta m^2_{\text{slow}} L}{E} \right) - \sin^2(2\theta_{13}) \sin^2 \left(1.27 \frac{\Delta m^2_{\text{fast}} L}{E} \right) \\ &= 1 - P_{\text{slow}} - P_{\text{fast}} \end{aligned} \tag{1.22}$$

These slow and fast components add up smoothly, as shown on Fig. 1.3.

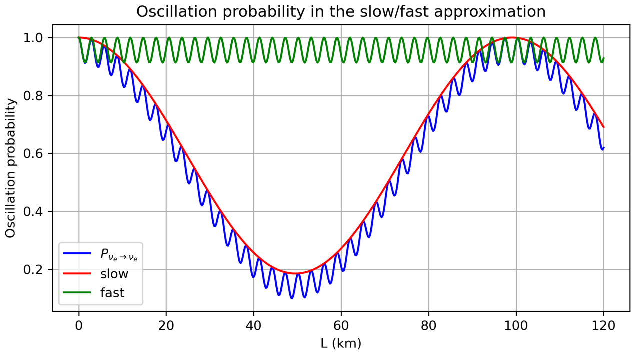

Figure 1.3: Plot of the survival probability of ν_e (Eq. 1.22) with the distance L (km). The parameters θ_{12}, θ_{13}, Δm^2_{21} and $\Delta m^2_{\text{fast}} = \Delta m^2_{32}$ are taken from Table 1.1 and $E = 3 \cdot 10^{-3} GeV$.

1.3 Actual knowledge on neutrino parameters

1.3.1 Neutrino oscillation parameters

There a 6 measurable neutrino oscillation parameters, including three mixing angles θ_{12}, θ_{13}, θ_{23}, two squared mass differences $\Delta m^2_{21} = \Delta m^2_{\text{slow}}$, $\Delta m^2_{32} \approx \Delta m^2_{\text{fast}}$ ($\Delta m^2_{31} = \Delta m^2_{32} + \Delta m^2_{21}$) and the Dirac phase δ_{CP} (the Majorana phases are global phases which cannot be measured through the oscillation probabilities). These parameters can be measured through the different neutrino sources of different energy ranges [30].

Nuclear reactor antineutrinos : θ_{13}
Electron antineutrinos $\bar{\nu}_e$ produced in nuclear reactors, mainly by β^- decay of fission product, have an energy of a few MeV and can be measured at very small distances. By measuring the antineutrino flux at some km of the source, the slow neutrino term P_{slow} can be neglected while it is possible to maximize the fast oscillation term P_{fast} to measure efficiently $\sin^2(2\theta_{13})$ and thus θ_{13} (see $P_{\bar{\nu}_e \rightarrow \bar{\nu}_e}(L)$ Eq. 1.22 and Fig. 1.3). Detectors like Double-Chooz [31], Daya Bay [32] and RENO [33] performed this method to precisely measure θ_{13}. It is for now the most accurately known oscillation parameter.

Atmospheric neutrinos : Δm^2_{fast} and θ_{23}
Neutrinos/antineutrinos (from electron and muon flavors) produced by cosmic rays interacting with Earth's atmosphere, of energies ∼100 MeV up to hundreds of TeV, travel ∼10 km up to 13 000 km, when going through the Earth. These distances and energy values make the fast oscillation significant while the slow contribution can be neglected, allowing the measurement of Δm^2_{fast} and θ_{23}. The most recent values of these parameters are given by the IceCube experiment [34] and the SK experiment [35].

Solar neutrinos : Δm^2_{slow} and θ_{12}
Solar neutrinos ν_e have a typical energy of ∼1-10 MeV and travel ∼150 million km to the Earth. These neutrinos allow long-distance oscillations studies through the slow oscillation part P_{slow}

which depend on Δm^2_{21} and θ_{12}. Solar neutrino experiment such as the SK [36], the SNO [37] and the Borexino experiment [38] have many years of data collection, to measure these parameters.

Accelerator neutrinos: δ_{CP}
Accelerators which produce neutrinos and antineutrinos (of electron and muon flavors) are used to measure the difference in their oscillations which depend on δ_{CP}. Accelerator like NOνA, and T2K [39] have constrained δ_{CP} through ν_e and $\bar{\nu}_e$ appearance and ν_μ and $\bar{\nu}_\mu$ disappearance. However, δ_{CP} is the less precisely known parameter, due to inconsistencies in the experiment results. More accurate measurement of δ_{CP} will be possible using DUNE and Hyper-Kamiokande experiments [40].

Values
The current values of the neutrino oscillation parameters are given at Table 1.1, for Normal Ordering (NO) and Inverted Ordering (IO) (see neutrino mass ordering ch. 1.3.2).

Parameter	Best fit	3σ interval
NO		
$\Delta m^2_{21}/10^{-5}$ [eV^2]	7.49	6.92 → 8.05
$\Delta m^2_{32}/10^{-3}$ [eV^2]	2.513	2.451 → 2.578
$\sin^2(\theta_{12})$	0.308	0.275 → 0.345
θ_{12} [°]	33.68	31.63 → 35.95
$\sin^2(\theta_{23})$	0.470	0.435 → 0.585
θ_{23} [°]	43.3	41.3 → 49.9
$\sin^2(\theta_{13})$	0.02215	0.02030 → 0.02388
θ_{13} [°]	8.56	8.19 → 8.89
δ_{CP} [°]	212	124 → 364
IO		
$\Delta m^2_{21}/10^{-5}$ [eV^2]	7.49	6.92 → 8.05
$\Delta m^2_{32}/10^{-3}$ [eV^2]	−2.484	−2.547 → −2.421
$\sin^2(\theta_{12})$	0.308	0.275 → 0.345
θ_{12} [°]	33.68	31.63 → 35.95
$\sin^2(\theta_{23})$	0.550	0.440 → 0.584
θ_{23} [°]	47.9	41.5 → 49.8
$\sin^2(\theta_{13})$	0.02231	0.02060 → 0.02409
θ_{13} [°]	8.59	8.25 → 8.93
δ_{CP} [°]	274	201 → 335

Table 1.1: Neutrino oscillation parameters: best fitted values and 3σ intervals for NO and IO. Values taken from [41].

Using the best fitted values of Table 1.1, assuming NO and setting $\delta_{\mathrm{CP}} = 0$, the PMNS matrix is expressed as :

$$\mathcal{U} \approx \begin{pmatrix} 0.823 & 0.548 & 0.149 \\ -0.489 & 0.549 & 0.678 \\ 0.290 & -0.631 & 0.720 \end{pmatrix} \tag{1.23}$$

1.3.2 Neutrino mass ordering

One of the unknowns neutrino property is the neutrino mass ordering. Indeed, from neutrino oscillation experiments, we know that $\Delta m^2_{21} > 0$, meaning $m_2 > m_1$, but the sign of Δm^2_{32} and Δm^2_{31} is not known. With these information, we cannot determine whether neutrinos follow a Normal Ordering (NO) $m_3 \gg m_2 > m_1$ or a Inverted mass Ordering (IO) $m_3 \ll m1 < m2$ (see Fig. 1.4). Therefore, experiments such as NOνA, T2K, SK (current experiments) and Hyper-K, ORCA, DUNE and JUNO (experiment in construction) aim to determine the Neutrino Mass Ordering (NMO) by measuring NMO-dependent differences in oscillation patterns.

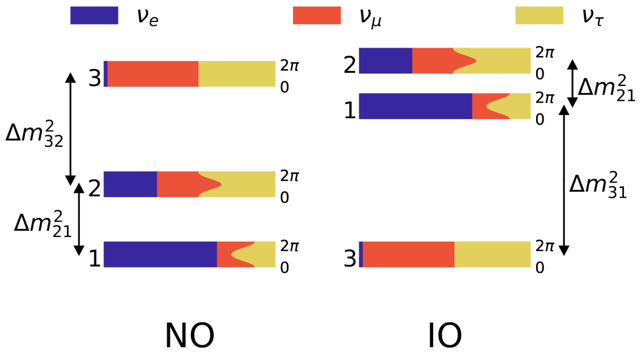

Figure 1.4: Neutrino normal and inverse ordering scheme, with the flavor distribution of each mass eigenstate. Taken from [42].

The sign of the mass differences Δm^2_{31}, Δm^2_{32} depend on the ordering

$$\begin{aligned}
\Delta m^2_{32} = m^2_3 - m^2_2 \quad &\Longrightarrow \quad \Delta m^2_{32} > 0, \quad \text{NMO} = \text{NO} \\
& \quad \Delta m^2_{32} < 0, \quad \text{NMO} = \text{IO} \\
\Delta m^2_{31} = m^2_3 - m^2_1 \quad &\Longrightarrow \quad \Delta m^2_{31} > 0, \quad \text{NMO} = \text{NO} \\
& \quad \Delta m^2_{31} < 0, \quad \text{NMO} = \text{IO}
\end{aligned}$$

The squared mass differences with a known NMO allows to calculate a lower bound for the total sum of neutrino masses $M_{\text{tot}} = m_1 + m_2 + m_3$ [43]:

$$\begin{aligned}
M_{\text{tot}} &\gtrsim 0.06 \text{ eV} \quad (\text{NO}) \\
M_{\text{tot}} &\gtrsim 0.1 \text{ eV} \quad\ \ (\text{IO})
\end{aligned} \tag{1.24}$$

Together with more and more precise upper bounds of neutrino mass presented before (section 1.2.3), the total sum of neutrino masses could eventually be fixed.

At the moment, there are 2 ways of measuring the NMO for neutrinos detectors:

1. Via matter effects, using atmospheric neutrinos crossing the Earth or long baseline experiments such as Noνa and T2K. [44]
2. Using the oscillation pattern difference from the sign of Δm^2_{32} and Δm^2_{31} with neutrinos propagating through vacuum (like the JUNO experiment). The difference between NO and IO is a small shift in the phase of the fast oscillations (see Fig. 1.5) [45].

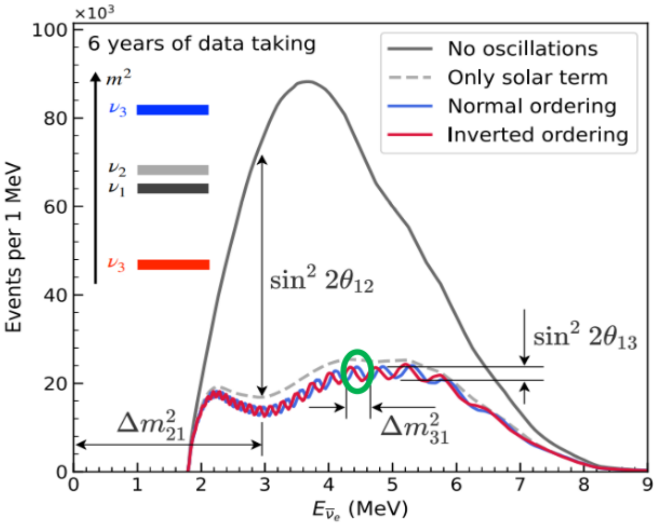

Figure 1.5: Small shift in the phase of the fast oscillation between both ordering.

Chapter 2

The Jiangmen Underground Neutrino Observatory

The second chapter focuses on the JUNO detector. It first details a general description of the characteristics, goals and architecture of the experiment followed by a picture of the main interactions in the detector.

2.1 The JUNO experiment

2.1.1 Overview

The Jiangmen Underground Neutrino Observatory (JUNO) is a large neutrino detector whose main goal is to determine the NMO. The main neutrino (more precisely electron antineutrino) sources of JUNO are two Nuclear Power Plants (NPP) situated at 53 km away : the Yangjian NPP and the Taishan NPP (Fig. 2.1). This location has been chosen because this distance gives the best NMO discrimination power when observing reactor antineutrinos [46]. Let us note that both NPP are at around the same distance of the detector to avoid interference effect due to the oscillation de-phasing [45].

Figure 2.1: JUNO experiment location. Taken from [47].

Typical neutrino detectors share the characteristic of having a large volume of interacting medium and are buried deep underground. The large volume compensates for the small interaction cross section of neutrinos while the underground characteristic is to shield other radiations which act as backgrounds. In the case of JUNO, it is buried $\sim$ 700 m underground and contains $\sim$ 1300 m^3 of neutrino interacting medium.

The promise of JUNO is to determine, after 6.5 years of data taking, the NMO with a 3σ level of confidence [48] and determine the parameters $\sin^2(2\theta_{12})$, Δm^2_{21}, and $|\Delta m^2_{32}|$ with a precision of 0.6% or better [47]. To achieve that, the big challenge is to reach an excellent energy resolution of less than 3% at 1 MeV [49] (the energy range of reactor antineutrinos is $\sim 1 - 12$ MeV). This implies constraints on the whole detector and in particular on the Photomultiplier Tubes (PMTs) coverage. To achieve this unprecedented precision, 4 complementary systems will be used to calibrate the detector and measure the energy [50].

2.1.2 Architecture of JUNO

JUNO detector is composed of two main parts (Fig. 2.2) :

1. The Central Detector (CD) : A spherical structure filled with Liquid Scintillator (LS) as the neutrino interaction target and placed at the center of the detector.
2. The veto detector, whose purpose is to eliminate background, composed of two sub-detectors : the water Cherenkov detector or Water Pool (WP), which is a ultra-pure water cylinder surrounding the CD and the Top Tracker (TT), a multi-layer plastic scintillator system located on top of the detector.

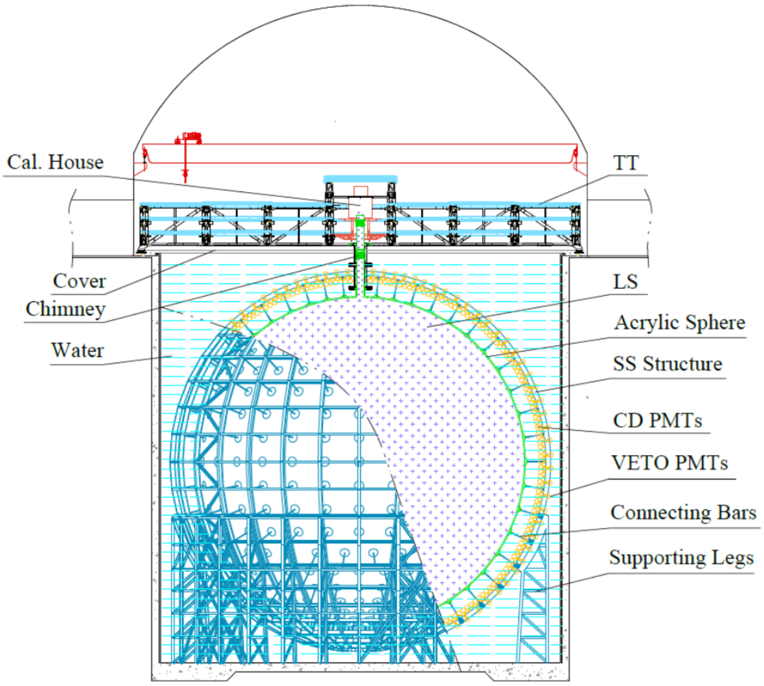

Figure 2.2: Schema of the JUNO detector. Taken from [47].

The central detector

The CD is made of an inner acrylic sphere with a diameter of 35.4 m, enclosed by an outer metallic sphere with a diameter of 37 m. The inner sphere will end up with 20 ktons of LS, making up around $1.4 \cdot 10^{33}$ target protons [45]. During the filling phase, both the CD and the WP were simultaneously filled with ultrapure water to equalize the pressure on both sides of the acrylic. When both were completely filled, the water in the CD was progressively replaced by the LS, being filled from the top. The detectors were already able to register data during the filling phase, which allow us to study the interaction properties in the water/LS and the veto detectors efficiency during this commissioning phase.

There are three components in the JUNO LS recipe: Linear Alkyl Benzene (LAB) used as the detection medium, due to its excellent transparency, high flash point, low chemical reactivity, and good light yield; 2,5-diphenyloxazole (PPO) as the fluor; and 1,4-bis(2-methylstyryl)benzene (bis-MSB) as the wavelength shifter. High quality of the LS chemicals is required to satisfy the strict energy resolution needed, which is achieved by a dedicated purification system and a radiopurity monitoring system called OSIRIS [47].

The outer spherical metallic structure is covered by PMTs looking towards the center of the sphere, through the acrylic. They are uniformly placed, with 17 612 20-inch PMTs and 25 600 smaller 3-inch PMTs filling the gaps, to cover to maximum area possible (Fig. 2.3). The larger PMTs are used to get the scintillation signal while the smaller PMT system serve as a calibration reference to reduce uncertainties, improve energy resolution and help event reconstruction. All PMTs of JUNO were tested and selected [47].

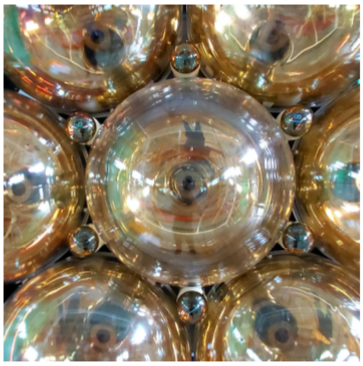

Figure 2.3: JUNO CD PMT system : large PMTs and smaller PMTs filling the gaps. Taken from [47].

The veto detector

As shown in Fig. 2.2, the WP is a cylindrical structure measuring 43.5 m in diameter and 44 m in height, filled with 35 ktons of ultrapure water. Ultrapure water is needed to minimize background noise from radioactive impurities. The WP serves both as an active Cherenkov detector and as a passive shield against terrestrial radioactivity. The Cherenkov light produced by muons going through the water (see ch. 2.2.2) is detected by 2400 20-inch Microchannel Plate Photomultiplier Tubes (MCP PMTs) which cover the outer surface of the CD. Additionally, the inner surface of the cylinder is covered with reflective foils to improve the detection of Cherenkov photons by the PMTs [47].

The TT is a plastic scintillator system designed to track atmospheric muons from cosmic rays. There are three layers, to reconstruct the trajectory of incoming muons, using the detection points at the three layers (Fig. 2.4). Each layers is made of several TT walls, each covering an area of 6.7 m × 6.7 m, arranged side by side with a 15 cm overlap to avoid dead zone (Fig. 2.5).

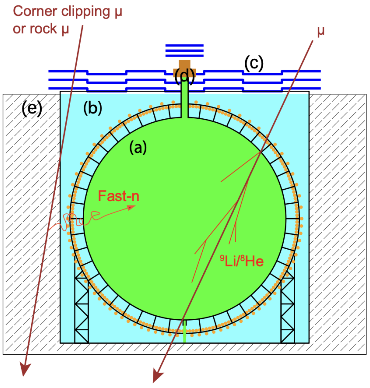

Figure 2.4: Schema of muon veto by the TT. Taken from [51].

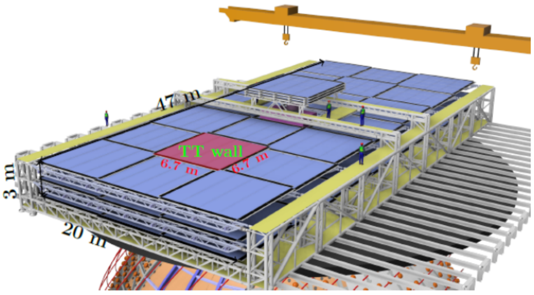

Figure 2.5: Schema of the Top Tracker architecture. Taken from [47].

These two veto systems are important to reduce atmospheric muons, which are a significant source of background to neutrino detection, as they are much more energetic than reactor antineutrinos and because they can produces radioisotope mimicking a $\bar{\nu}_e$ interaction. More details on the interactions of particles in JUNO are given at ch. 2.2.

2.1.3 Timing of JUNO

The underground laboratory construction happened in 2015-2022, and the CD installation was finalized in fall 2024. The water and LS filling phases started in December 2024 and in February 2025, respectively. The current status (11 august 2025 local time) of the detector filling is presented in Fig. 2.6. The start of the data taking with the detector in its final configuration is expected in September 2025.

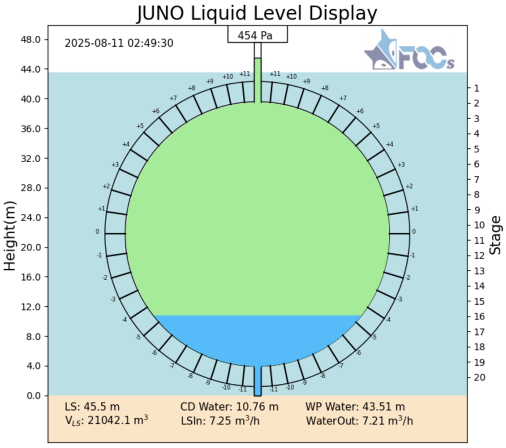

Figure 2.6: Current status of JUNO filling : almost 95% volume of LS.

2.2 Interactions with JUNO

Due to JUNO underground location, most of natural radiations are shielded. There are still three main expected detectable radiation : neutrinos, atmospheric muons and terrestrial radioactivity.

2.2.1 Neutrino interactions

While JUNO is optimized to measure reactor antineutrinos, other external sources of neutrinos contribute to the detection rate, such as CCSN, the Diffuse Supernova Neutrino Background (DSNB), solar neutrinos, atmospheric neutrinos and geoneutrinos. Each of those interacts via different processes, depending on their energy.

Source	**Energy range**
Reactor antineutrinos	0 – 12 MeV
CCSN	0 – 80 MeV
DSNB	10 – 40 MeV
Solar neutrinos	0 – 16 MeV
Atmospheric neutrinos	0.1 – 100 GeV
Geoneutrinos	0 – 3 MeV

Table 2.1: Energy range of various sources of neutrinos. Taken from [47].

Inverse Beta decay
The dominant interaction at MeV energies for which JUNO has been designed is the CC Inverse Beta decay (IBD) :

$$\bar{\nu}_e + p^+ \to n + e^+ \tag{2.1}$$

Each reaction between an electron-flavor antineutrino and a proton of the LS generates a neutron and a positron which will produce a characteristic signal. The neutron will thermalized after $\sim 200\mu$s and will be captured, mainly on a free proton (99% producing a 2.2 MeV γ ray) or rarely on a Carbon atom (1% producing a 4.95 MeV γ ray) [47]. On the other hand, the positron will quickly slow down, generating ionization-induced scintillation, and then annihilate with an electron of the medium, resulting in two $180°\gamma$ rays, each of 511 keV energy. The signature of this reaction is the prompt signal of a typical β^+ spectrum followed by a delayed signal of a γ peak at 2.2 MeV which is easily identifiable.
CCSN are also a source of $\bar{\nu}_e$ (see ch. 3.1.1), such that if one happens in our galaxy, at 10 kpc for example, we expect ~5000 IBD events in JUNO, within a few seconds. The DSNB flux however, is much lower: $\bar{\nu}_e$, produced by all CCSN throughout the universe, are expected to generate about 2-4 IBD events per year, depending on the model. Another source of $\bar{\nu}_e$ interacting via IBD are the geoneutrinos produced in the decay chain of ^{238}U and ^{232}Th in Earth's crust. JUNO may be able, through precise geoneutrino measurement, to constrain the Th/U ratio with good accuracy, an important parameter in the understanding of Earth's formation [47].

Inverse Beta decay-like interaction on Carbon
Neutrinos can also interact through CC with the Carbon nuclei of the LS :

$$\nu_e + {}^{12}\mathrm{C} \to {}^{12}\mathrm{N}^+ + e^- \qquad \bar{\nu}_e + {}^{12}\mathrm{C} \to {}^{12}\mathrm{B}^- + e^+ \tag{2.2}$$

The Carbon nucleus undergoes the transformation $n \leftrightarrow p$ and the resulting ionized nucleus quickly neutralizes with the other atoms of the LS. This interaction have an energy threshold of $\sim$ 14 MeV for $\bar{\nu}_e$ and $\sim$ 17 MeV for ν_e, making it accessible mainly by the atmospheric and CCSN neutrinos [52].

Elastic scattering
Neutrinos of all flavors can interact elastically with the LS via the electron Elastic Scattering (eES) and the proton Elastic Scattering (pES):

$$\text{eES} : \nu + e^- \rightarrow \nu + e^- \qquad \text{pES} : \nu + p^+ \rightarrow \nu + p^+ \tag{2.3}$$

ν_μ and ν_τ main detection channel is via NC interactions. Therefore, these NC elastic scattering interactions allow JUNO to be sensitive to other flavors than ν_e. JUNO can reconstruct the transferred energy from the interacting neutrino through the e^-/p recoil kinetics energy.
These interactions constitute the primary method for detecting solar neutrinos in the LS but it would also be triggered by high neutrino fluxes. For example, a CCSN happening at 10 kpc would trigger $\sim$ 300 eES events and $\sim$ 2000 pES events.
One of the secondary goals of JUNO is the more precise measurement of ^{7}Be and ^{8}Be solar neutrino fluxes which could bring a contribution to the solar metalicity problem [45, 53].

Other CC interactions
For atmospheric neutrino of high energy, more complex reactions are possible [54], such as :

$$\nu_\mu + e^- \rightarrow \mu^- + \nu_e \tag{2.4}$$

This kind of reactions will not be detailed here as it goes beyond the scope of this thesis and as these events are rare.

2.2.2 Atmospheric muons interactions

The Earth's atmosphere is continuously bombarded by astroparticles coming from cosmic phenomena, the so-called cosmic rays. When these high-energy particles interact with the nuclei of the atmosphere, they produce a cascade of secondary particles, including muons μ^- (and antimuon μ^+) which are called atmospheric muons. Atmospheric muons are highly penetrating due to their relatively large mass and ultra-relativistic energies. Like electrons, they also loose energy via bremsstrahlung [1], but their bigger mass reduces their braking, allowing them to travel long distances through matter. Therefore, if they are energetic enough, they can go through the rock above JUNO and can be detected in the CD. Atmospheric muons are one of the main background for neutrino detection and can interact with JUNO via different processes.

Ionization-induced scintillation
Ionization-induced scintillation occurs when charged particles, excite the molecules of the LS, which then deexcite by emitting photons. Because muons are charged particles, their primary interaction with JUNO is via ionization-induced scintillation. The associated signal which act as a background for neutrino detection can be removed thanks to the WP veto detector via the Cherenkov effect.

Cherenkov effect
When a charged particles is going faster than the velocity of light in a medium $v > c/n$, with the refractive index of the medium n, electromagnetic rays are generated via Cherenkov effect. This

---

[1] Bremsstrahlung (or braking radiation): electromagnetic radiation emitted when a charged particle is decelerated or deflected, often by the electric field of atomic nuclei.

phenomenon comes from the antisymmetric polarization in the medium induced by the charged particle [55].

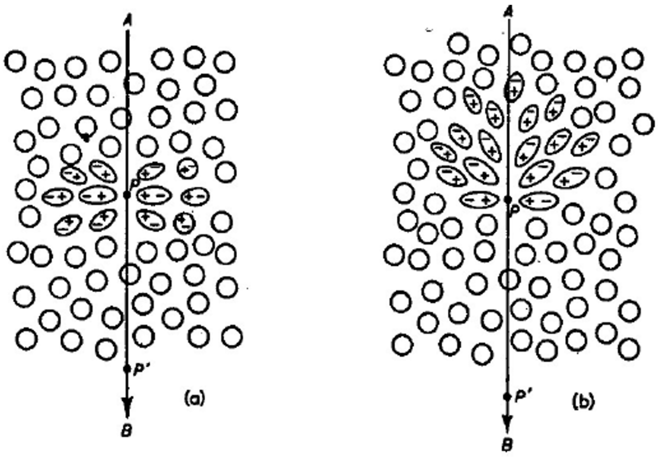

Figure 2.7: Illustration of the Cherenkov effect. At left (a), the charged particles velocity is below c/n: the polarization is symmetric. At right (b) the charged particle velocity is above c/n: the medium dipole are slower than the particle, making the polarization non symmetric. Taken from [55].

The light is then emitted through the antisymmetric deexcitation of the medium dipoles.
Atmospheric muons which are capable of going through the 700 m of rock above JUNO, have a velocity close to the velocity of light. Thus, atmospheric muons going through the water surrounding the CD generate light via the Cherenkov effect. This phenomenon is used by the WP detector to tag atmospheric muons and delete the corresponding scintillation signal in the CD. The Cherenkov effect also occurs in the LS but it only accounts for about 10% of the detected photons produced by muons.

Muon spallation
Muon spallation are the processes in which muons interact with the nucleus in/around the detector's medium (like water, LS or rock) and produce radioactive isotope. The most problematic spallation processes for neutrino detection are the ^{9}Li/^{8}He production which undergo $\beta - n$ decays

$$^9\text{Li} \to {}^8\text{Be} + e^- + \bar{\nu}_e + n \qquad {}^8\text{He} \to {}^7\text{Li} + e^- + \bar{\nu}_e + n \tag{2.5}$$

These decay processes mimic IBD interactions (prompt β signal followed by a delayed neutron capture), causing correlated background for reactor antineutrino analyses.
Based on the production cross section measured at the KamLAND detector, taking into account of the $\beta - n$ branching ratio of 51% for ^{9}Li and 16% for ^{4}He, the total expected rate of $\beta - n$ decays is 84/day. With some energy and time cut, this rate can be reduced to $\sim$ 71/day [56, 45].

Muon decay
Some atmospheric muons are stopped in the detector and undergo its standard weak decay

$$\mu^- \to e^- + \bar{\nu}_e + \nu_\mu \qquad \mu^+ \to e^+ + \nu_e + \bar{\nu}_\mu \tag{2.6}$$

with a mean lifetime of $\tau_{\mu^\pm} \approx 2.197\mu s$. This interaction is a particularly annoying background for low energy neutrino detection. Indeed, atmospheric muons with kinetic energies below the Cherenkov threshold $v < c/n$ are invisible to the WP veto detector and produce electrons which can mimic the prompt signal of IBD. In this context, it is important to apply correctly time-correlation cuts.
On the other hand, this interaction can be useful for calibration, due to the predictable spectrum of decay electrons (method used at SK) [57].

Muon spallation and muon decay are considered as secondary triggers, since they often occur shortly after the primary scintillation signal. These secondary triggers are subject of study on chapter 4.2.1.

2.2.3 Terrestrial radioactivity

Natural radioactivity from the surrounding rock is a significant source of low-energy background in JUNO. Thanks to the ultrapure water which acts as a shield, α and β radiation (which are low penetrating) will be absorbed before entering the CD, but we expect γ rays and neutrons to be able to go through. The decay chains of primordial radionuclides like ^{238}U, ^{232}Th, and ^{40}K emit γ rays and neutrons at relatively low energy. Currently, studies are in progress to determine which isotopes are inducing radiation detection in the CD [58].

While JUNO has been designed to measure neutrino oscillations parameters and the NMO, we saw that it can also be useful for other purposes. An interesting application is the detection of CCSN through neutrinos.

Chapter 3

Signal and background

We will now study the CCSN signal and its expected background. The chapter begins with a brief overview of the possible stellar evolution paths, providing information to understand the conditions that lead to collapse. This is followed by a qualitative description of the CCSN stages, with the associated neutrino emission and relevant simulations. The chapter concludes with a summary of the used runs from the data-taking period conducted with JUNO during the filling phase, which serves as a reference for the background.

3.1 Core-Collapse Supernovae

A Core-Collapse Supernova (CCSN) is one of the two main types of supernovae and occurs at the end of a massive star's life. The life of a star can be summarized as a continuous fight against gravitational collapse. Two main forces act to withstand gravity : heat pressure generated by nuclear fusion and degeneracy pressure from Pauli exclusion principle.

For stars with masses greater than about $8M_\odot$[1], this equilibrium eventually breaks down. After burning its nuclear fuel, the star's core becomes composed mostly of iron, which cannot undergo further fusion to produce energy. Once the core mass reaches the Chandrasekhar limit ($M_{\mathrm{Ch}} \sim 1.4M_\odot$), the electron degeneracy pressure is no longer sufficient, and the core collapses under its gravity.

This collapse of the star triggers a rebound shock wave expelling the star's outer layers in a supernova explosion. What is left of the star after the CCSN, called the remnant, is either going to be a neutron star or, if massive enough, a black hole.

3.1.1 Stellar evolution

This section is inspired by material from [16] and [59].

To understand how massive stars eventually collapse, it is essential to understand the forces governing their evolution.

Heat pressure

The heat generated by fusion increases the temperature of the core, generating outward thermal and radiative pressure. The heat pressure refers to both pressures combined.

---

[1] $M_\odot$: mass of the Sun.

Fusion is a nuclear process where two or more elements fuse into a new one. Fusion of light elements is an exothermic process : it generates energy via the difference in the binding energy per nucleon (see Fig. 3.1).

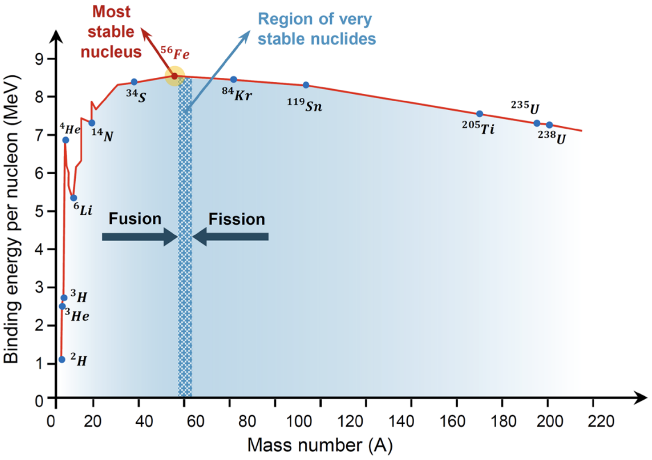

Figure 3.1: Binding energy per nucleon as a function of the mass number A. Taken from [60].

The maximum binding energy per nucleon is reached by Iron (^{56}Fe), which is thus the most stable nucleus, meaning that both its fusion and fission are endothermic processes.
The fusion of light elements requires extremely high temperatures ($\sim 10^7$ K or more) to overcome the Coulomb repulsion between the protons in the nuclei. In the case of a star, once the critical temperature is reached in the core, fusion becomes a self sustainable process, where the heat produced is in equilibrium with the energy lost through convection and radiation, maintaining the temperature in the interior of the star.

Degeneracy pressure

The degeneracy pressure comes from the Pauli exclusion principle which forbids fermions from occupying the same state in the phase space. This principle prevents the electrons from being too close to each other which generates outward pressure. When the outward pressure is dominated by electron degeneracy pressure, the star is called degenerated. There are two types of degeneracy pressure at play in stars: the electron degeneracy pressure and the neutron degeneracy pressure.
Stars, before collapse, can be modeled as an ionized plasma composed mainly of protons and electrons. At typical densities of these stars, the proton degeneracy pressure is negligible, and the degeneracy pressure is dominated by electrons. However, the electron degeneracy pressure has a limit: the Chandrasekhar mass $M_{\text{Ch}} \approx 1.4 M_{\odot}$. For example, a white dwarf, which is purely electron degenerated, cannot have a mass bigger than the Chandrasekhar mass limit without collapsing. This limit can be interpreted in two ways:

1. Limit of the degeneracy pressure against the gravitational pressure, the latter being proportional to the mass.
2. Limit of the number of electrons accessible states in the phase space (x, p) due top Heisenberg uncertainty principle $\Delta x \cdot \Delta p \geq \frac{h}{2}$ and the light velocity limit $v \leq c$.

On the other hand, in neutron stars, degeneracy pressure of neutrons, which is much stronger than electron's, is the primary outward force stopping the collapse. To illustrate the difference between the scopes of these two degeneracy pressures, a white dwarf is typically the size of the Earth, while a neutron star has a radius comparable to a city ($\sim$ 10 km), both having masses close to that of the Sun.

The possible paths of a star's life

The stellar evolution of a star depends mainly on its mass before the main sequence (sequence during which the star fuses H into ^{4}He), due to its link with the strength of the gravitational force. Stellar evolution can be classified as such (see Fig. 3.2):

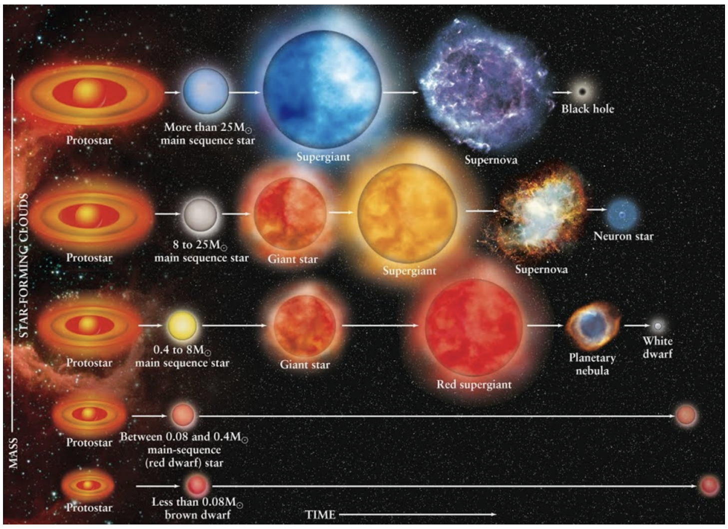

Figure 3.2: Stellar evolution for different star's mass. Taken from [61].

1. $M \lesssim 0.08 M_\odot$: At these small masses, the core will never compress and heat up enough to trigger fusion due to electron degeneracy pressure being stronger than gravity. These stars are called brown dwarfs and their structure nearly change over time.
2. $0.08 M_\odot \lesssim M \lesssim 0.4 M_\odot$: The mass of these stars is large enough to compress and heat up the core to trigger and maintain Hydrogen fusion through pp cycle, but very slowly. This configuration is called red dwarf and have an extremely long lifetime, typically about a trillion years, far exceeding the age of the universe.
3. $0.4 M_\odot \lesssim M \lesssim 8 M_\odot$: For these stars, the fusion of H into ^{4}He will happen more quickly than for the previous case, and the H atoms will progressively be replaced. Eventually, the core will consume most of the available H fuel and the heat pressure will decrease causing the core to compress under gravity. When the compression heats the core to a sufficient temperature, ^{4}He fusion into ^{12}C starts. This new fusion reaction generates a huge amount of energy and the star expands to equilibrate at a larger radius, becoming a red giant. During this period, the star expels part of its mass (this mass loss is still not fully understood), letting appear a planetary nebula around the star. The fusion of heavier elements will be possible depending on the mass, but at some point the core won't be able to contract enough to continue fusion. At the end of its life, the star will become a white

dwarf with varying compositions of ^{12}C,^{16}O, ^{20}Ne and ^{24}Mg, depending on its life's fusion reactions.

4. $M > 8M_\odot$: These massive stars will undergo a series of contraction and expansion, between the fusion stages ($H \rightarrow {}^4$He $\rightarrow {}^{12}$C $\rightarrow ... \rightarrow {}^{56}$Fe) due to the difference in temperature and density needed to trigger the next stage. The iron core of a massive star is entirely electron degenerated and can thus be seen as a white dwarf surrounded by the outer layers (showing a so-called onion structure, see Fig. 3.3). As ^{56}Fe accumulates, the total core's mass will inevitably reach the Chandrasekhar mass limit. At this point, the electron degeneracy cannot withstand gravity and the core collapses, producing a supernova explosion, hence named core-collapse supernova. After the explosion, what is left of the star, the remnant, is a Proto-Neutron Star (PNS) which will become a neutron star with time [62]. If the mass of the star was $M \gtrsim 25M_\odot$, the resulting neutron star remnant is likely to exceed the Tolman–Oppenheimer–Volkoff (TOV) limit (the analogue of the Chandrasekhar limit for white dwarf) [63], collapsing into a black hole.

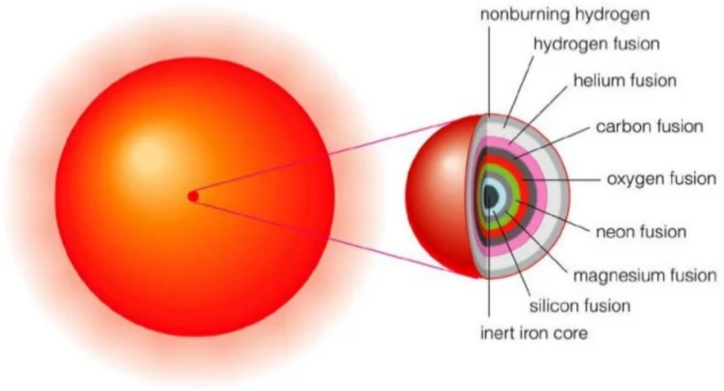

Figure 3.3: Core composition at the end of a massive ($M > 8M_\odot$) star's life. Taken from [64].

Some studies suggest that for extremely heavy stars ($M \gtrsim 40-130M_\odot$ depending on the metalicity), the collapse leads directly to the formation of a black hole, without an associated supernova explosion [64]. These configurations are called failed supernovae. Since this work focus on CCSN, we consider stars with masses $M > 8M_\odot$ leading to CCSN on the next sections.

3.1.2 Core-Collapse Supernovae : a neutrino driven explosion

This section describes the core-collapse mechanism and the following supernova explosion, focusing on the associated neutrino emission.
When the Iron core reaches the Chandrasekhar mass limit, the core and subsequently the outer layers collapse. The increase in density forces the electrons to get closer, increasing the Fermi energy. This increase of energy enables electrons to be captured by surrounding protons [65]. The electron capture happens mainly on free protons but some studies suggest that nucleus protons also play an important role on the electron capture rate during collapse [65, 66]. This capture results in Eq. 3.1 :

$$e^- + p^+ \rightarrow n + \nu_e \tag{3.1}$$

The collapse becomes a feedback loop process : electron captures reduce degeneracy pressure, which increases density and triggers even more captures. This process, called neutronization, stops when nuclear density is reached, at which point the strong force becomes repulsive.

However, the CCSN is not an instantaneous phenomenon and is currently believed to be composed of six phases (see Fig. 3.4). The following explanations of the CCSN steps are taken from [62, 67].
The initial phase (1) begins with the infall of matter, increasing rapidly the core's density and starting the neutronization. During this phase, neutrinos produced in the collapsing core are able to escape into space.

When the central density reaches the critical value, $\rho_c \sim 10^{12}$ g/cm^3, neutrino NC scattering on infalling nuclei becomes significant enough that the outward diffusion of neutrinos is slower than the accelerating collapse of matter. This phase is called neutrino trapping (2), during which neutrinos produced by electron capture accumulate. During this phase, the infalling matter can accelerate up to 30% of the velocity of light in the outer core region.

As the core reaches nuclear density $\rho_0 \approx 10^{14}$ g/cm^3, the collapse of the core suddenly stops, creating an outwards shock wave (3), called the prompt shock. At this point, the center of the dying star is composed of a uniform nuclear medium, marking the birth of the PNS.

The prompt shock propagation rapidly loses energy as it is met by the infalling matter (4). However, this shock decreases the density, allowing all the trapped ν_e to finally escape the star and get released in a big burst named the ν_e burst. On the other hand, infalling matter passing through the shock front is decelerated, heated, partly dissociated into free nucleons and accreting on the PNS surface.

Both of these phenomena decrease the energy of the front shock which typically stalls at around 100-200 km (5), still inside the collapsing Iron core (the radius of these massive stars before collapsing are in the range $\sim 2.1 \cdot 10^7$ - $7 \cdot 10^8$ km). At the same time, in the growing PNS, $\nu/\bar{\nu}$ and e^-/e^+ pairs are generated through thermal processes. These $\nu/\bar{\nu}$ escape the core while e^-/e^+ get captured by nucleons, generating additional $\nu/\bar{\nu}$. These $\nu/\bar{\nu}$ fluxes deposit energy via NC scattering in the region between the PNS and the stalled prompt shock. In this zone, called the gain layer, this energy deposition increases the outward pressure. Once enough energy accumulates, the pressure becomes sufficient to revive the shock wave, ultimately triggering the supernova explosion. Since the shock is revived by neutrinos, this CCSN mechanism, which was consolidated with SN1987A observation, is referred to as a neutrino-driven explosion. At this point, there is no further mass accretion on the proto-neutron star since the outer layers are expelled in a spectacular explosion.

After the explosion, the PNS cools down during which it emits a neutrino signal (6), detectable on earth for ~10 s. After the neutrino cooling phase, the PNS either stabilizes into a neutron star or collapses into a black hole if the TOV limit is reached.

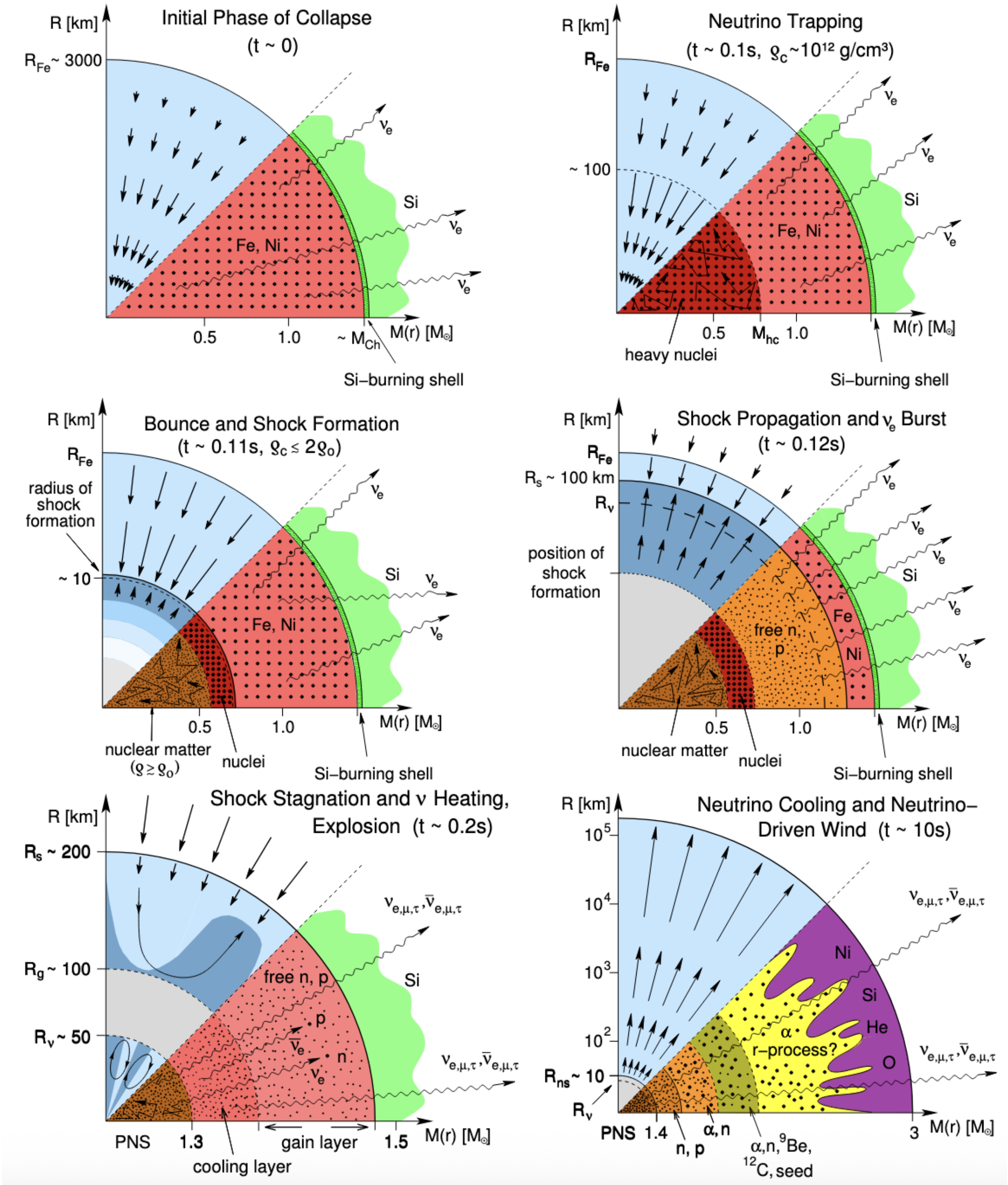

Figure 3.4: Six stages of the CCSN. In the lower halves of the plots, the composition of the stellar medium and the neutrino effects are sketched, while in the upper halves the flow of the stellar matter is shown by arrows. The horizontal axis gives mass information ($M_{\rm Ch}$ = Chandrasekhar limit, $M_{\rm hc}$ = mass of collapsing inner core) while the vertical axis show the different radii R_i (Fe = iron core radius, s = shock radius, g = gain radius, ns = neutron star radius, ν = neutrinosphere). Taken from [67]

If the CCSN happens accordingly to the description of this section, neutrino emission can be divided in three phases : the ν_e burst, the accretion phase and the PNS cooling. Each emission phase presents a distinct signature, providing complementary information about neutrinos and the underlying physical processes of the CCSN stages. An example of neutrino luminosity curve is given in Fig. 3.5, using the Garching model simulation.

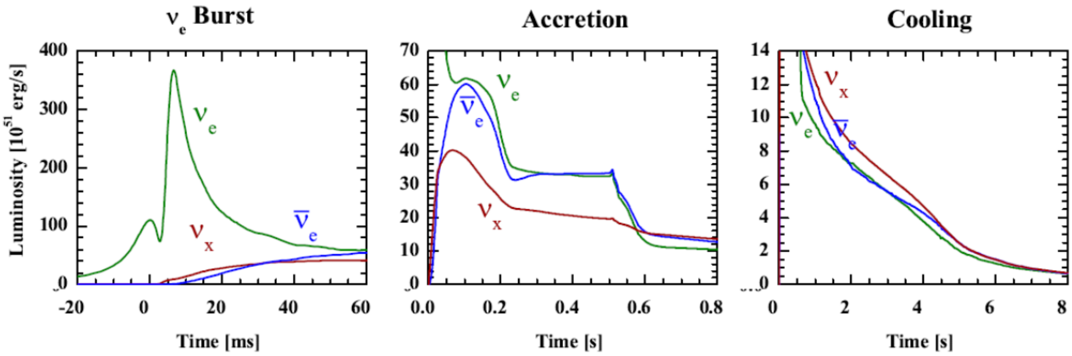

Figure 3.5: Garching model of a $27M_\odot$ CCSN neutrino luminosity curves for the three neutrino emission phases ($\nu_x = \nu_\mu, \nu_\tau$). Taken from [45].

There exists several models for CCSN simulation with different neutrino emission.

3.1.3 Core-Collapse Supernovae simulations

The last close CCSN, the SN 1987A located in the Large Magellanic Cloud at ~50 kpc was the only CCSN from which a neutrino burst was directly detected by neutrino detectors. At this time, the resolution of the detectors were not as good as today but ~25 events were recorded by 3 detectors, about 3 hours before any light signal could be seen [68, 69, 70]. Since then, CCSN are still not fully understood as they are very complex phenomena and are rare at an observable distance via neutrinos. Several CCSN numerical models have been developed, waiting for a CCSN to happen close enough to assemble a final model that accurately describes this phenomena. These models differ mainly through their assumptions, in particular in the choice of the Equation of State (EoS), the dimensionality of the simulation, and the neutrino transport model.

In the attempt to theoretically describe CCSN, the use of accurate EoS is essential. These equations describe the behavior of hot and dense nuclear matter in the stellar core. Three EoS models are widely used :

1. The Lattimer–Swesty EoS (LS EoS) [71] : based on the compressible liquid-drop model of nuclei [12] and does not account for relativistic effects.
2. The Shen EoS [72] : based on relativistic mean-field theory (nuclei described as interacting Dirac nucleons) [73] and the Thomas-Fermi approximation (poly-electronic systems modeled as a degenerate Fermi-Dirac gas) [74].
3. The Steiner, Fischer, and Hempel EoS (SFHo EoS) [75] : based on relativistic mean field theory calibrated with astrophysical observations of neutron star.

The dimensionality of the model is also an important parameter when constructing a CCSN simulation. For example, assuming spherical symmetry reduces the problem to one dimension, which results in a significant computational gain. This simplification enables more precise computation of the EoS solutions, but it does not capture multidimensional features like turbulences, convection and anisotropies.

Neutrino transport refers to the way neutrinos are produced, absorbed and scattered through the dense stellar matter and were originally inspired from neutron transport models in nuclear reactors. The computation of neutrino transport is especially important around the PNS and the gain region. Many neutrino transport approaches exist but a detailed description of them is beyond the scope of this work. For curious readers, the paper [76] details various neutrino transport models for CCSN.

Some models, using the EoS described above, are summarized in the Table 3.1, with a selection of key features (many additional features of each model are not discussed here).

Model	**Masses ($M_\odot$)**	**Dimension**	**EoS**	**Key Features**
Nakazato (2013)	13, 20, 30, 50	1D	LS220/Shen	Varying metalicity possible : Z=0.004 or Z=0.02
Tamborra (2014)	20, 27	3D	LS220	Highlight effects of hydrodynamic instability enhancing ν heating during shock revival (SASI) [77]
Sukhbold (2015)	9.6, 27	1D	LS220/SFHo	Calibration with SN 1987A and Crab SN
Bollig (2016)	11.2, 27	1D/2D/3D	LS220	Ray-by-ray-plus approximation for multidimensional ν transport [78]
Warren (2020)	9.0-100.0 (200 total)	1D	SFHo	Use of 1D turbulences simulation (STIR) and Adaptative Mesh Refinement (AMR) [79]
Fornax (2021)	9-27 (15 in total)	2D	LS220/Shen/SFHo	Assume axisymmetry, use of AMR and parallel computing

Table 3.1: Summary of the CCSN models. LS220 stands for the LS EoS with incompressibility $K = 220$ MeV. Information taken from [80, 2].

3.1.4 Context

The expected rate of CCSNe, close enough to detect them via neutrinos from the Earth, is less than ∼2 per century [81]. On the other hand, the number of neutrinos detected from a CCSN is highly dependent of its distance to the Earth. Indeed, since the neutrino emission

can be approximated to be isotropic in all directions, the CCSN neutrino flux decreases as $\frac{1}{d^2}$. Therefore, while JUNO is expected to detect around 5000/10 000 events for a CCSN happening at a distance of 10 kpc, it wouldn't be able to detect a CCSN via neutrinos for distances larger than about 300 kpc.
Let us now study the star clusters close to the Earth : the Local Group [82], knowing that, in first approximation, the CCSN rate in a galaxy is proportional to its stellar mass M_* [83].

- The Milky Way (MW) : Potential CCSN happening in our galaxy would be the best case for observation since it would be at relatively short distances (most within ∼23 kpc[2].). It is also the most probable source of CCSN with an expected CCSN rate of 1.63 ± 0.46/century [81].
- The Large Magellan Cloud (LMC) and Small Magellan Cloud (SMC) : satellite galaxies to the MW at a respective distance of 50 kpc and 61 kpc. These distances would allow us to detect CCSN through neutrinos but they present a smaller probability of occurrence. Indeed, the stellar mass of the LMC and the SMC is respectively around 40 and 130 times smaller than that of the MW [84, 82]. Nevertheless, the SN1987A originated from the LMC.
- The Andromeda galaxy (M31) : It is the closest galaxy to the MW at around 780 kpc. Its CCSN rate is approximately equivalent to the MW rate since they have a comparable stellar mass. However, the distance between the Earth and the stars in the Andromeda galaxy is too large to hope to detect CCSN neutrinos.

Other smaller clusters of star are orbiting the MW, but their combined stellar masses are small enough that we can neglect the probability of CCSN occurrences in these clusters.

On the other hand, neutrinos are not the only CCSN signal. Due to the movement of matter during the process, CCSN generates gravitational waves which can be detected on Earth. These two detection mechanisms are followed, after time (∼ 3h for the SN1987A), by an intense light emission which can be seen with the naked eye for the closer ones. The detectors aiming to detect CCSN before the light signal reaches the Earth are together part of the Supernova Early Warning System (SNEWS) [85].

Therefore, the goal of the real-time monitor presented in the last chapter is to detect CCSN, concomitantly with other detectors of the SNEWS, before the light signal arrival, so that the scientific community can be prepared to observe it.

3.2 Simulation and data set

3.2.1 Simulation

In this thesis, we will use the Nakazato model [86] with a progenitor mass of $13M_{\odot}$, at varying distances (20 kpc and 60 kpc) and LS filling (25%, 50% and 75%). In addition, a simulation is performed for $\bar{\nu}_e$ interactions with JUNO via IBD only, which is conservative since other interaction channels would increase the signal. Lastly a simulation of the JUNO electronics, including afterpulses and dark noise, is carried out.

---

[2] The sun is at ∼ 8.2 kpc to the center of the MW and the star-forming disk, where most CCSN occur, has a radius of ∼ 15 kpc

3.2.2 Data set

The filling period of JUNO is used to perform the detector commissioning, including detector calibration, trigger optimization, and background studies.

These months of data taking allow us to see the background to CCSN for different levels of LS filling, since they seemingly do not contain any traces of CCSN.

The trigger condition in JUNO was fixed, after weeks of tests as a relatively simple trigger that applies a multiplicity cut, i.e., a threshold on the number of detected hits (the nhits unit is explained in the next chapter) within a given time window. The width of the window is 180 ns and the threshold is at 200-300 nhits which is equivalent to an energy of ∼200-300 keV.

The Table 3.2 gathers the information of the data set used in the next chapters. The LS filling is measured with 2 sensors and the given value is the average of them. For a LS level under study, the data runs used are the stable ones, within a maximum LS deviation of ±2%.

Due to a breach in the CD (which has been handled since then) the LS filling has been stopped during ∼ 20 days. This delay, gives us access to ∼ 6 days of stable data runs with a non varying LS filling at around 76.7%.

The data runs that will be of use for the next chapters have a total duration of 3 days and 7 hours for ∼25% LS, 5 days and 4 hours for half LS and 5 days and 13 hours for 76.7% LS.

Run name	Date	Duration	LS filling (%)
∼25% LS			
5016, 5017, 5018	07/04/2025	∼11h	23%
5019, 5020, 5021, 5022, 5023	08/04/2025	∼15h50’	24%
5044, 5046, 5047, 5048	09/04/2025	∼12h49’	24.5%
5050, 5053, 5054	10/04/2025	∼9h13’	25%
5057, 5110 5111, 5115	11/04/2025	∼12h45’	25.8%
5116, 5117, 5119, 5120, 5121	12/04/2025	∼13h06’	26.1%
5122	13/04/2025	∼4h	27%
∼50% LS			
5946, 5947, 5956, 5957, 5958, 5959	19/05/2025	∼20h23’	48%
5961, 5963, 5965, 5970, 5971, 5972	20/05/2025	∼16h57’	49%
5977, 5985, 5989, 5993, 5994, 5995	21/05/2025	∼22h13’	49.5%
5996, 5999, 6007, 6009, 6010, 6011	22/05/2025	∼22h55’	50.4%
6012, 6042, 6043, 6044, 6045	23/05/2025	∼19h31’	51%
6046, 6050, 6051, 6052, 6053, 6054	24/05/2025	∼20h30’	51.9%
76.7% LS			
7097, 7099	30/06/2025	∼1h21’	76.7%
7137, 7145, 7146, 7147	01/07/2025	∼13h16’	76.7%
7148, 7246, 7247	02/07/2025	∼11h11’	76.7%
7302, 7317, 7318	03/07/2025	∼7h50’	76.7%
7341, 7359, 7360, 7361	04/07/2025	∼10h44’	76.7%
7366, 7373, 7375	05/07/2025	∼10h59’	76.7%
7377, 7378, 7379	06/07/2025	∼12h02’	76.7%
7450, 7451	08/07/2025	∼5h34’	76.7%
7602, 7603, 7604	11/07/2025	∼9h01’	76.7%
7688, 7689	13/07/2025	∼3h35’	76.7%
7714, 7715, 7716	14/07/2025	∼8h12’	76.7%
7786, 7787, 7788, 7789	15/07/2025	∼16h10’	76.7%
7790, 7880, 7883	16/07/2025	∼4h57’	76.7%
7886, 7897, 7901, 7903, 7906, 7908, 7909, 7910	17/07/2025	∼18h32’	76.7%

Table 3.2: Data sets of JUNO.

Chapter 4

Events selection tools

This chapter goes into the details of the different parameters to be optimized to enhance the detection efficiency of supernova event. As supernovae neutrinos, cosmic muons and rock radioactivity are coming from different physical processes, they show different energy distributions, that can be used to minimize the background. Two veto methods are shown, with their consequences on the rates of detection of neutrinos and background.

4.1 Energy and charge

The first thing that comes to mind when searching how to discriminate particles from different physical processes is the differences between their energy distributions. Plotting these energy distributions, should allow us to find an optimal range of energy where neutrinos are dominant. While it can be difficult to reconstruct the energy of particles interacting with JUNO, we have access to the deposited charge in the detector via two quantities: the number of hits and the number of photoelectron.

4.1.1 Number of hits

The number of hits (nhits) is an indirect measure of the PMT signal duration. The nhits is derived, by counting how many times the PMT signal is higher than a threshold, defined as 1.5RMS above the average.

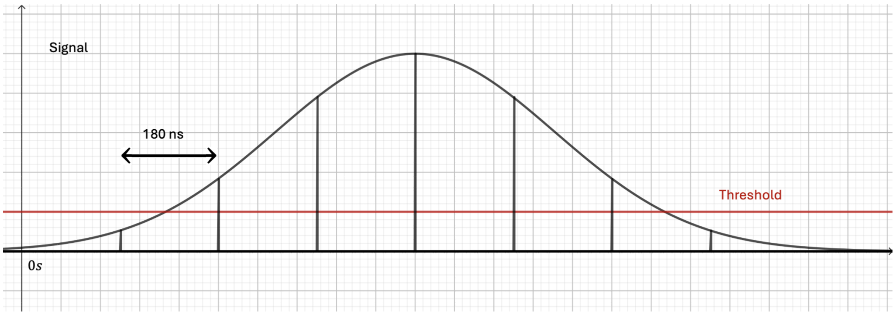

Figure 4.1: Example of how nhits is calculated from the signal received by the PMT.

In this example (Fig. 4.1), the threshold is represented by the red line and the time between two counts is 180 ns. Thus, nhits would be 5 for this particular PMT signal.
The nhits unit gives an immediate approximation of the deposited energy from the interacting particle but lack of precision as each registered hit counts for one, independently of the signal's amplitude.

4.1.2 Number of photo-electrons

On the other hand, the number of photoelectrons (npe) is a physical unit proportional to the total scintillation light detected by the PMTs, giving a correlation with the deposited energy in the detector. This is the unit that will be calibrated to get the precise energy resolution needed in JUNO. In order to reconstruct the npe from the signal, there are three possibles algorithms : COTI, convolution and machine learning.

COTI: Continuous Over-Threshold Integral
This methods consists in an integral calculation of the signal [87]. Let's see how it works. The average (baseline) and the root mean square (RMS) are computed from the last 32 points of the signal, called the buffer. The points above the threshold, defined as 1.5·RMS above the baseline, are considered as waveform points and are not registered in the buffer to keep a clean baseline. The waveform starts when there are 5 consecutive points over the threshold and ends when 3 consecutive points are back inside the threshold. The integral of the signal with respect to the baseline is then computed from the first to the last point above the threshold.

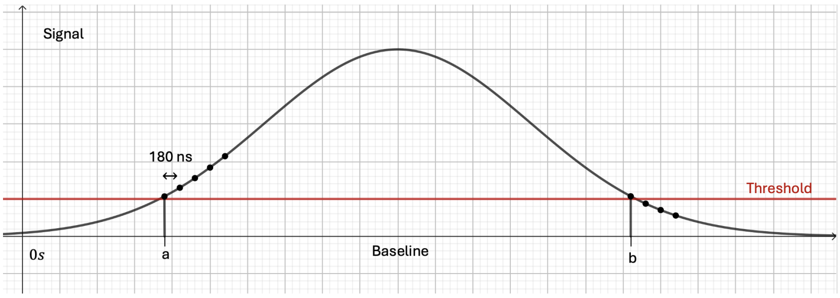

Figure 4.2: Example of how npe is calculated : integral of the signal between a and b.

The integration of the PMT signal should be proportional to the total charge collected. This is the method currently used in JUNO to reconstruct the npe but presents some flaws. First, a fluctuation of the baseline could bias the integral calculation and secondly, at large signal, the signal may become non linear with the npe. Other more accurate methods are thus in study.

Deconvolution method
This method uses the waveform model of the PMT electronics [88]:

$$w(t) = q(t) \otimes V_{PE}(t) + \epsilon(t) \tag{4.1}$$

Where $w(t)$ is the signal, $q(t)$ is the photoelectron distribution, $\otimes$ is the convolution symbol, $V_{PE}(t)$ is the response to a single photoelectron and $\epsilon(t)$ is the white noise. In order to have access to $q(t)$, we apply Lucy's iterative deconvolution algorithm. This method is not currently used because of hardware issues, but a viable hardware implementation is being tested.

Machine learning
The idea is to develop a neural network trained on waveforms from which the associated number of npe is known. This method is still in study.

4.1.3 Results

Using the CCSN simulation and the data runs detailed in the previous chapter, we can plot the superposition of the signal and the background nhits (Fig. 4.4) and npe distribution (Fig. 4.3), for half filling of LS.

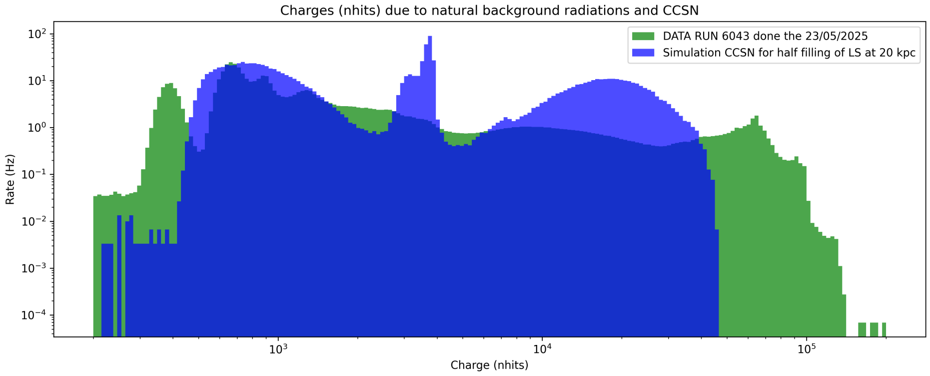

Figure 4.3: Histogram of the distribution of the nhits rate, in half LS for the data run (in green) and for a CCSN simulation at 20 kpc (in blue).

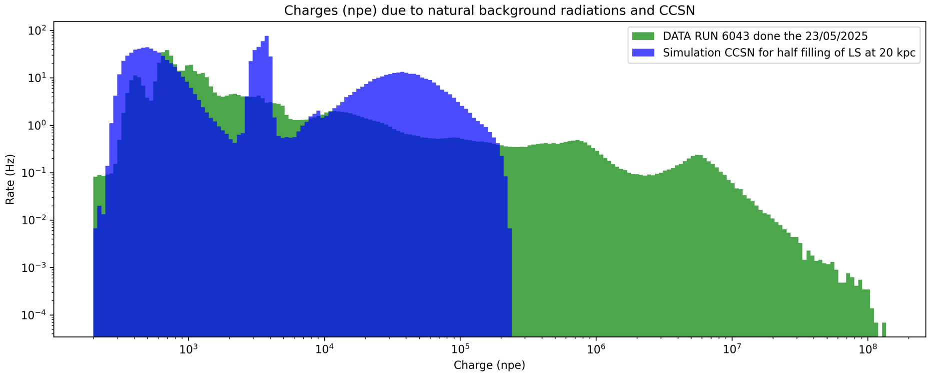

Figure 4.4: Histogram of the distribution of the npe rate, in half LS for the data run (in green) and for a CCSN simulation at 20 kpc (in blue).

These plots were computed using a mean rate of detection in order to reduce the variance. If we used ordinary counts in ordinate, due to the duration of a CCSN of some seconds, we would also have to take a data run of some seconds to compare them, which is highly sensitive to statistical fluctuations. Therefore, the data histogram is made of a large number of data runs, normalized by the total time of detection. For the CCSN simulation, the plot is normalized by the number of simulated CCSN (100) and by a duration of 3 seconds which should be conservative (see $\bar{\nu}_e$ peak Fig. 3.5).

4.1.4 Interpretation

It would be interesting here to discuss a little bit of the physical meanings of the plot above. While the nhits plot gives an immediate approximation of the deposited charge and is thus useful for real-time applications, the npe plot is directly correlated to the deposited charge and thus to the particle energy distribution but requires a time-demanding reconstruction algorithm. We will thus interpret the plots through the npe unit (Fig. 4.3), but the nhits plot will be useful later. Let us also note that half filling of LS plots are shown through this chapter, in order to see the characteristics of interactions in both water and LS (other plot with different filling of LS are shown in appendix A.4.2).

Link between npe and nhits

To better interpret the difference between the npe and nhits graphics, let us plot the link between them (Fig. 4.5).

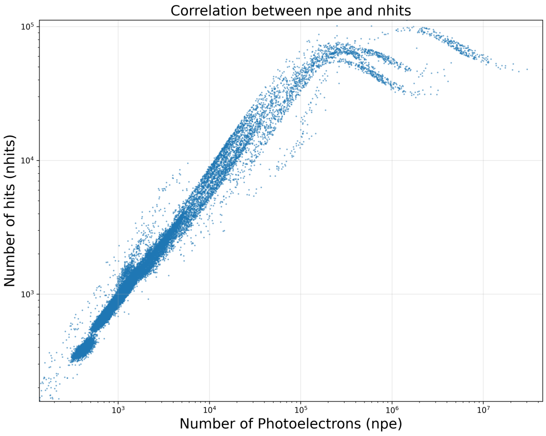

Figure 4.5: Relation between the npe and the nhits unit, each point being a recorded interaction in JUNO at half filling of LS, using data run 6043.

We see that both units are approximately linear at low energy but nhits saturates at higher energy. This is because the nhits unit records only one hit per event above the threshold, such that a high signal cannot be distinguished from a medium signal. This saturation explains the difference at high energy for the nhits plot (Fig. 4.4) and the npe plot (Fig. 4.4) : the second peak at higher energy is merged with the first one.

Data

For the data in half LS, we can identify three zones on the plot 4.4: the low npe peaks, two high npe peaks and the region between them.

The low energy peaks below 10^3 npe are caused by the PMT electronic noise.

Between the low energy peak and the high energy peaks are the secondary triggers of muons and the terrestrial radioactivity.

We identify that the peaks at around $8 \cdot 10^5$ npe and $6 \cdot 10^6$ npe correspond to the cosmic muon primary energy depositions during their passage in each medium : the LS and the water. The Fig. 4.6 illustrates one muon going through the LS part of the CD and another going through the water part of the CD. Due to the higher sensibility of the LS, both muons won't produce the same number of photoelectrons, explaining the two peaks of muons interactions.

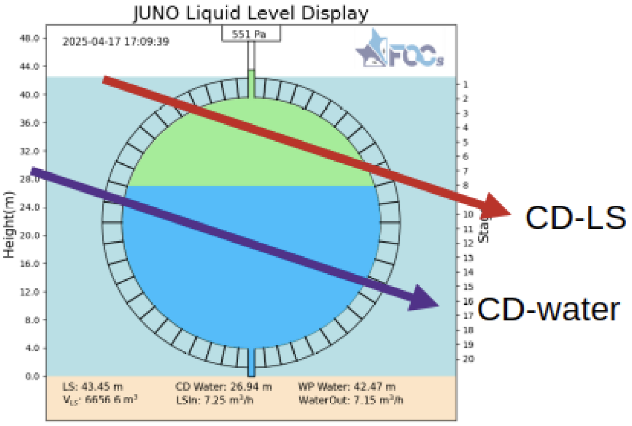

Figure 4.6: Schema of cosmic muons going through each medium in JUNO.

In order to confirm that, as the filling of LS happens from the top, the higher npe interactions should happen at the top of JUNO and the lower npe interaction at the bottom. Let us plot the height of interaction with the npe (Fig. 4.7).

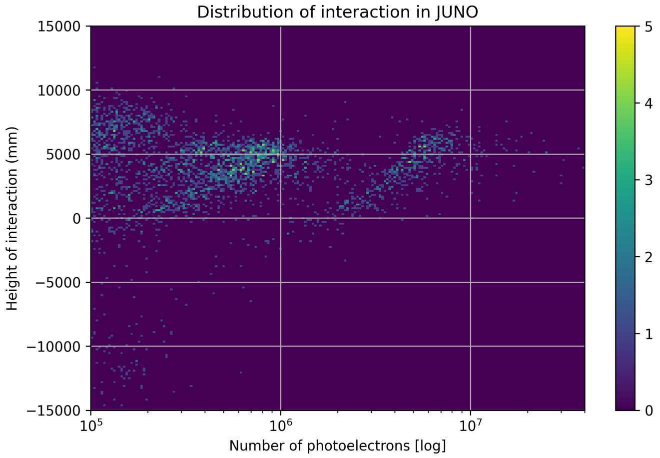

Figure 4.7: Relation between height of interaction and number of photoelectron with half filling of LS, using data run 6043.

From this plot (Fig. 4.7), we can conclude that the high npe peak is due to the primary muons signal in the LS zone (high npe, high height cluster) and that the peak at around $2 \cdot 10^5$ npe is composed of the cloud in the LS zone which seems to be some of the secondary triggers (low npe, high height cluster) and the primary muons signal in water (low npe, low height cluster). Since the interactions in LS generate much more signal than in water, this interpretation is better illustrated for smaller levels of LS filling (see Appendix A.4.1).

CCSN simulation
This part of the plot (still Fig. 4.4) is easier to interpret since it comes from our simulation. The CCSN $\bar{\nu}_e$ interact with the medium via IBD:

$$\bar{\nu}_e + p \rightarrow n + e^+ \tag{4.2}$$

Therefore, the plot is composed of three parts: the broad spectrum centered around $4 \cdot 10^4$ npe represents the energy deposited by the positron, which is the sum of the kinetic energy deposit and the annihilation ; the narrower peak centered around $3.5 \cdot 10^3$ is the neutron peak ; and the lower energy peak represents the afterpulses and secondary triggers. The interaction mechanisms of ν in JUNO are detailed in chapter 2.2.

4.2 Veto

A veto is a rule whose purpose is to suppress unwanted events. The implementation of two vetos allows to minimize the background while nearly not affecting the neutrino signal in the zone of interest. These vetos can be useful for other applications than the CCSN monitor.

4.2.1 First veto: secondary triggers

The first veto aims to suppress secondary triggers of muons (see section 2.2.2), to reduce the background in the neutrino signal region. To achieve that, when a high energy signal is recorded in the CD, the first veto suppresses any hits occurring shortly afterward, in a time window of 60μs after the first trigger [89].

Results
First veto results are presented in Fig. 4.8 and 4.9 in half LS.

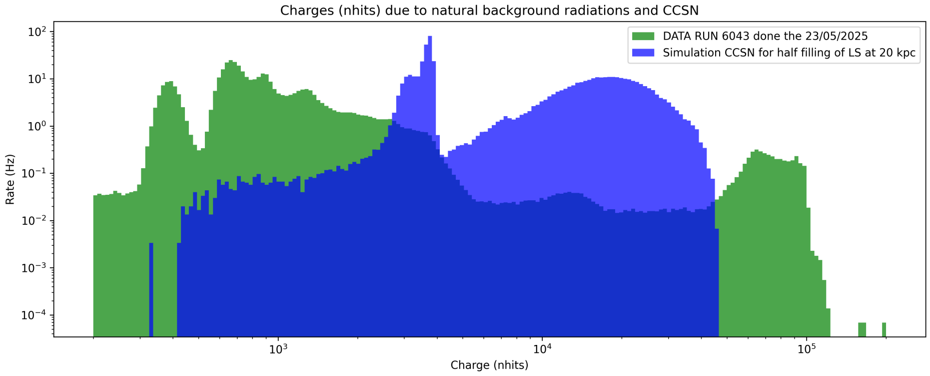

Figure 4.8: Histogram of the distribution of the nhits rate, in half LS, applying first veto, for the data run (in green) and for a CCSN simulation at 20 kpc (in blue).

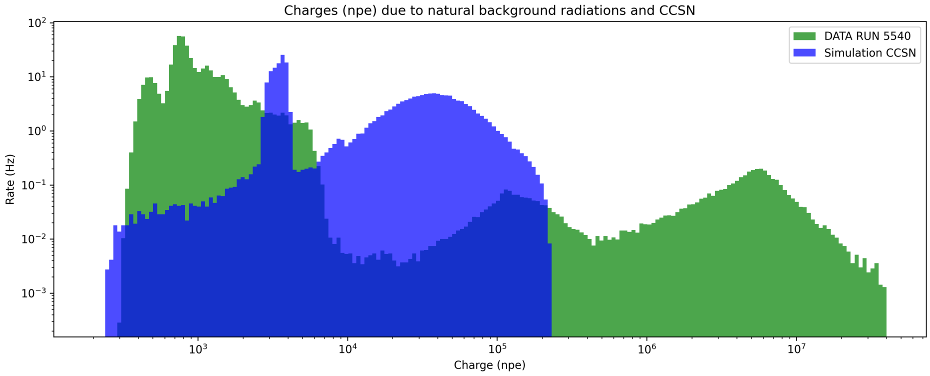

Figure 4.9: Histogram of the distribution of the npe rate, in half LS, applying the first veto, for the data run (in green) and for a CCSN simulation at 20 kpc (in blue).

Compared to the initial plots, we can see that the background is reduced in the neutrino energy range of interest while most of the lost neutrino signal is at lower energy. In addition, now we can see more clearly the peaks due to rock radioactivity between 10^3 npe and 10^4 npe (see chapter 2.2.3). Finally, plotting the height with the npe, with the first veto, should allow us to see where the primary interaction of muons happens and verify our interpretation (Fig. 4.10).

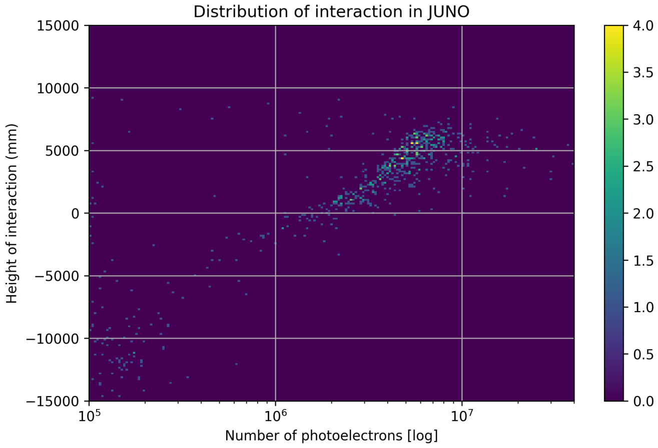

Figure 4.10: Relation between height of interaction and number of photoelectron with half filling of LS, applying the first veto, using the same data run as in Fig. 4.7.

As expected, removing the secondary trigger shows clearly that the peaks correspond to primary muons signal in each medium (once again it is better seen for smaller filling levels of LS Appendix A.4.1).

We can conclude from these charts that our implementation of the first veto works correctly.

4.2.2 Second veto: waterpool

As seen in chapter 2.1, the CD of JUNO is surrounded by the WP detector, used to tag muons. Muons going through JUNO are detected simultaneously in both the CD and WP while $\bar{\nu}_e$ IBD interaction can only happen in one detector at the time. Hence, if an event is registered in both the CD and the WP, we can conclude that it is most likely a cosmic muon and the event is suppressed.

Implementation
Implementing this method seems first to be straightforward, by comparing the timing of every event in the CD and in the WP : if $|t_{cd_i} - t_{wp_j}| < 20\ \mu s$, the event is deleted. The problem is that the number of events detected, over one data file, is in the CD around $n = 45000$ and in the WP, around $m = 18500$ events, meaning that comparing each event one by one would take $m.n = 45000.18500 = 832,5$ millions requests, per file which would take too much computational time.
One way of solving this problem is by understanding that most of these requests are useless, as the time interval between the first and the last event is of some seconds while the veto duration is 60 μs. Thus, dividing the WP file into sub-lists, corresponding to different parts of the time domain, allows to compare optimally the events. The CD list is virtually divided, setting the start and end time of each WP sub-list, with a window of 60 μs. An illustrative example is shown in Fig. 4.11, to help the reader's understanding.

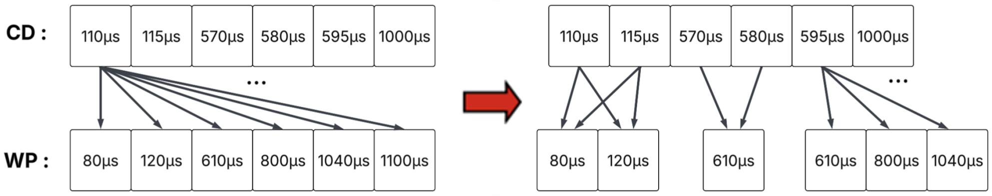

Figure 4.11: Illustrate how the waterpool events list is divided (red arrow) and how events are compared (black arrows).

In this example, both lists are made of 6 events and the file dividing number $n_{fd} = 3$, since the WP event lists is divided in three sub-lists. Therefore, each 2 CD events will be compared with a different sub-list of WP. The window of 60 μs allows the WP event 610 μs to belong in two different sub-lists to be compared with the events 570 μs, 580 μs and 595 μs.

As this method aims to reduce the time complexity of the second veto, let us try and estimate its complexity gain. If n is the length of CD events and m is the length of WP events, the original complexity was $n.m$. The subdividing list method consists in three steps : first, the computation of the WP index corresponding to the CD events, then the addition of all WP event in the proper sub-lists and lastly the comparison of the CD event to the associated sub-lists events. Therefore, the total complexity becomes $n_{fd} + m + \frac{n.m}{n_{fd}}$ which can be roughly approximated to $\frac{n.m}{n_{fd}}$ for typical values of n, m and n_{fd}. Therefore, the computational time is approximately divided by a factor n_{fd}. The file dividing number n_{fd} should thus be large. However, increasing it too close to the length of the lists would slow down the process, as subdividing too much produces sub-lists with redundant events to satisfy the 60 μs window constraint. Therefore n_{fd} is set to 1000, to be high but not too close from the length of the WP list.
In practice, this file dividing method reduces the simulation time from some hours to a few

minutes per file.

This file dividing method is only useful for the simulation which post processes big lists of events. When the CCSN detector's design is operational, the second veto will be applied on real-time events.

Results

The resulting spectra after applying the second veto are shown in Fig. 4.12 for nhits and Fig. 4.13 for npe.

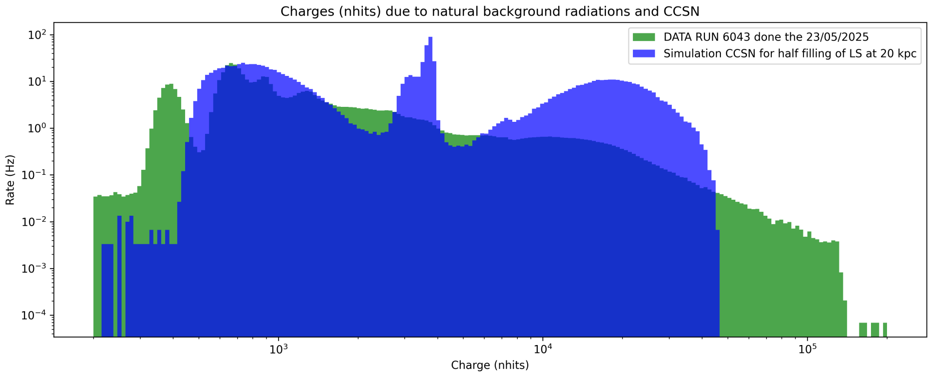

Figure 4.12: Histogram of the distribution of the nhits rate, in half LS applying the second veto, for the data run (in green) and for a CCSN simulation at 20 kpc (in blue).

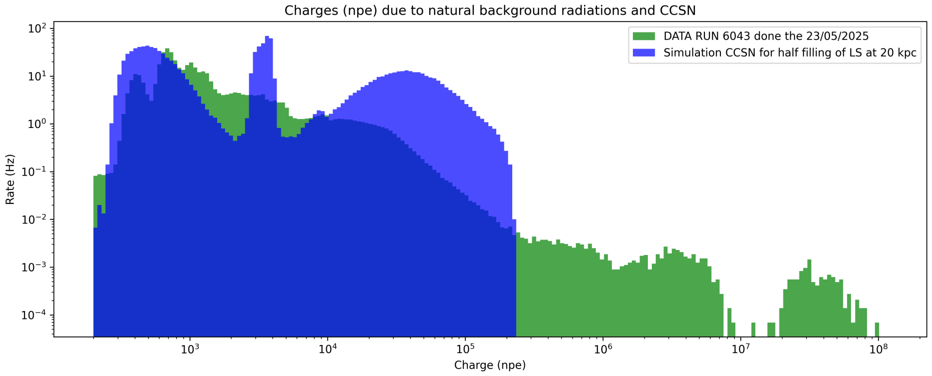

Figure 4.13: Histogram of the distribution of the npe rate, in half LS applying the second veto, for the data run (in green) and for a CCSN simulation at 20 kpc (in blue).

We can see that, in comparison to the previous plots, the background noise is reduced at high energy which corresponds to primary cosmic muons signal, while the neutrino signal was not

affected, as expected.
We conclude that the second veto is well implemented.

4.2.3 Both veto

Now that we saw the effects of both vetos and that we know their correct work, let's apply them together to see the resulting plots, still on half LS (Fig. 4.14 for nhits and Fig. 4.15 for npe).

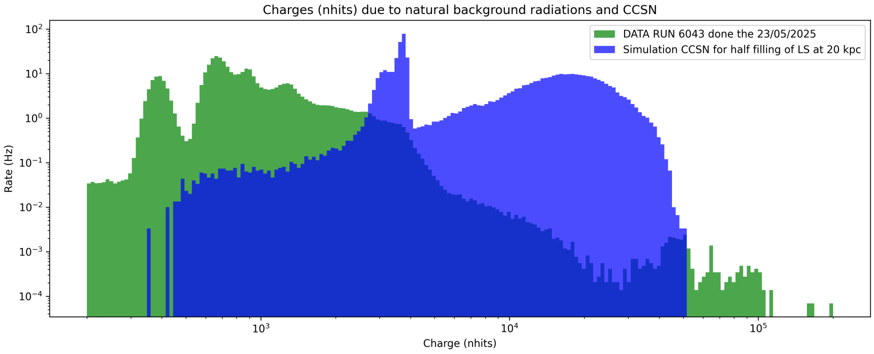

Figure 4.14: Histogram of the distribution of the nhits rate, in half LS applying both vetos, for the data run (in green) and for a CCSN simulation at 20 kpc (in blue).

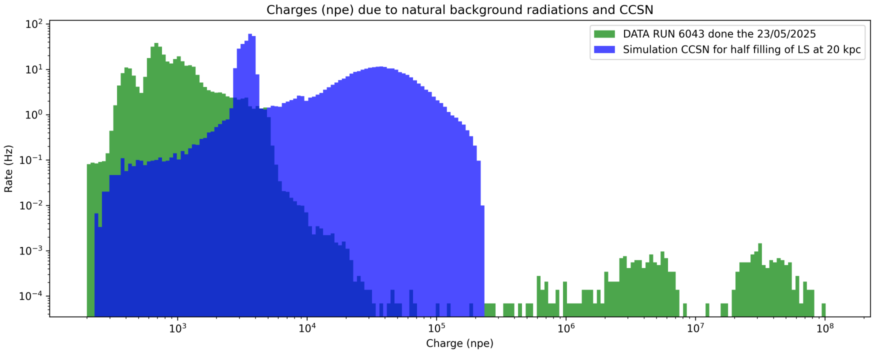

Figure 4.15: Histogram of the distribution of the npe rate, in half LS applying both vetos, for the data run (in green) and for a CCSN simulation at 20 kpc (in blue).

In comparison with the initial plot without veto, the background has been significantly decreased in the regions of interest, going from a bin rate of 1 Hz to bin rates in the range $10^{-4} - 10^{-2}$ Hz.

Chapter 5

Real time core-collaspe supernovae monitor

The last chapter concludes this work by studying the implementation of the real-time monitor of JUNO. The first section introduces two methods to evaluate the optimal nhits range for the monitor. Then, the difference in time characteristics of both the signal and the background is used to favor CCSN neutrinos, using a sliding window method. Lastly, the monitor results are shown and the maximum simultaneous number of events from the background in a month is estimated based on a regression model.

5.1 Optimal nhits range for the CCSN monitor

Based on the npe and nhits distribution plots shown in previous chapter, this section aims to determine an nhits range which favors the CCSN neutrino signal compared to the background for the real-time monitor. Let us remind that while the npe was a useful unit to interpret our results, its reconstruction requires a time-demanding algorithm, making it unsuitable for real-time applications. Therefore, we will now focus on the nhits unit, which is available nearly instantaneously.

This study will be conducted for a CCSN happening at a distance of 60 kpc, which is far enough to require optimal parameters for detection but close enough to detect it. This distance is also approximately the one of the SMC, which is the most distant star cluster, having a CCSN rate and an expected number of neutrino detections sufficient for detection.

5.1.1 Method

Building a method to select the optimal nhits range allows a systematic problem resolution and decreases potential biases. The method must be based on two optimization conditions : the nhits range chosen should maximize the number of detected neutrinos and minimize background events and particularly simultaneous events which could induce false CCSN alerts.

The threshold, designed to be triggered only by CCSN events, needs to be an upper bound of background events to avoid false CCSN alerts. The maximum number of background events in a bin is reached when multiple events are simultaneously detected within the same time window. By approximating the background events with a Poisson distribution, which is equivalent as assuming that the detector is perfect (no afterpulses, time window infinitely small, etc.) and assuming that the mean $\langle n \rangle$ is close to zero, the probability of having more than K events in a bin is :

$$P(X > K) = 1 - e^{-\langle n \rangle} \sum_{k=0}^{K} \frac{\langle n \rangle^k}{k!} \approx \frac{\langle n \rangle^{K+1}}{(K+1)!} \tag{5.1}$$

Therefore, minimizing the probability to have a coincidence of several events in a bin comes down to the minimization of the background rate.

Since several CCSN models with varying neutrino distributions exist, the method used here to find the optimal nhits range for the monitor only depends on background events. To minimize these events, we set an upper bound for the background detection rate. In practice, the range is composed of the nhits distribution bins in which

$$\text{Background rate of bin i} < \alpha \tag{5.2}$$

Our problem boils down to the choice of the parameter α which is not straightforward : if it is too large, only few bins will be taken in the range, meaning that too few neutrinos will be detected, and if it is too small, the background will induce too much simultaneous detections. Additionally, this parameter won't be the same for different fillings.
Several attempts have been made to build an algorithm that automatically chose the optimal α from the nhits distribution plots, but the results were chaotic (different solutions even within runs of the same filling) and not always efficient. We will thus determine it later, by plotting the real-time monitor resulting from different values of α and choosing the one which gives the best result.

Alternative method
When the next near CCSN occurs, its neutrino emission distribution will be measured with much greater precision and we can expect that a corresponding CCSN model will accurately represent reality. In such case, a natural optimization metric arises :

$$M = \frac{n_{\text{CCSN}\nu}}{n_{\text{background}}} \tag{5.3}$$

By taking the bins in which this metrics is maximum, the neutrino detection rate will be maximized while the background coincidences are minimized.
For now, this approach remains model-dependent, but let us still try to exploit this metric to prepare a method for future uses. For the CCSN, we will use the Nakazato model, already used throughout this work.
Similarly to the previous method, a way of building the optimal nhits range based on this metric is to take the bins satisfying the condition:

$$M_i (= \text{Optimization metric M in bin i}) > \beta \tag{5.4}$$

The problem boils down to the chose of the parameter β, which again cannot be too large if we want to have enough bins in the range. A possible solution to determine the optimal value of β is the maximization of both the total optimization metric M_{tot} and the number of bins in the range n_{bins}. With that in mind, let us plot $M_{\text{tot}} \cdot n_{\text{bins}}$ as a function of β (Fig. 5.1), for a CCSN happening at 60 kpc, with half filling of LS (25% and 75% of LS are shown appendix A.5.1).
The nhits range given by this method is optimal, for half filling of LS, when $\beta \approx 2.25 \cdot 10^4$.

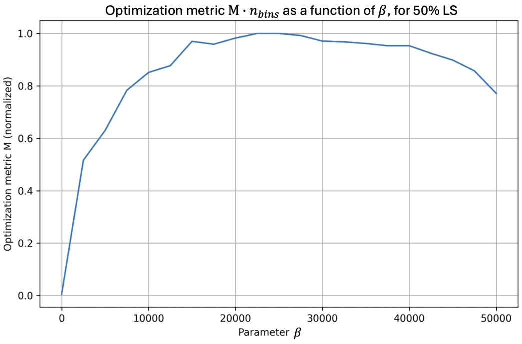

Figure 5.1: Metric $M_{\text{tot}} \cdot n_{\text{bins}}$ as a function of the parameter β, for half LS.

5.2 Time characteristics

Up to this point, the comparison between the signal and the background was only based on the mean detection rates, but for the real-time monitor, the temporal characteristics are of great importance. Therefore, we now perform a simulation of the real-time events detection, by processing the CCSN simulations (Fig. 5.2) and the data runs (Fig. 5.3), both for half filling of LS and a nhits range between 10^4 and $4 \cdot 10^4$ (this range, though not the most optimal one, better illustrate the dynamics of background real-time detection). The data runs used in this chapter to represent different level of LS filling are detailed in the Table 3.2.

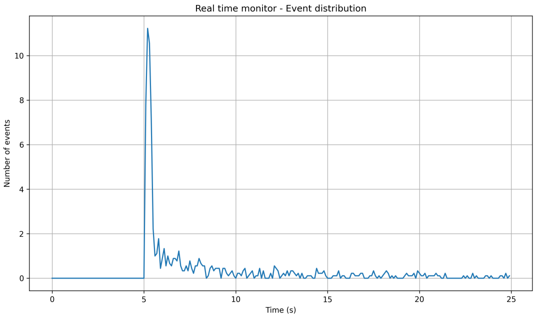

Figure 5.2: Simulation of the real time detection of 60 kpc CCSN $\bar{\nu}_e$ in half LS with a bin size of 100 ms.

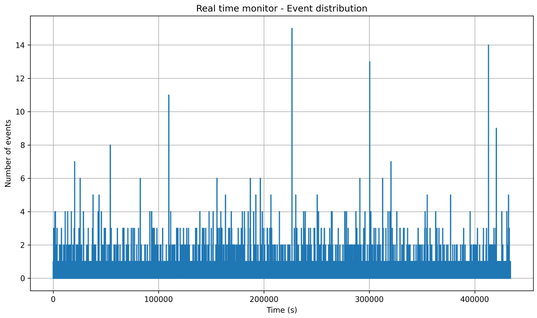

Figure 5.3: Real time detection of background from the data run 6043, in half LS with a bin size of 100 ms.

We immediately notice that these plots show differences in time characteristics. The simulation of the CCSN neutrinos shows a peaked behavior, with the vast majority of detection happening in about half a second. Background, on the other hand, presents discrete events which are subject to statistical fluctuations. Thanks to JUNO architecture and the vetos, the bins have most of the time ($\sim$ 98.9%) zero events.

The difference in time characteristics is due to the difference in the underlying physical processes: a CCSN blasts neutrinos during few seconds (see chapter 3.1.1) while the background is mostly made of independent events. For example, a background bin showing three events can be due to the simultaneous detection of 3 independent cosmic muons in the time window of the bin.

We would like to use this difference to favor neutrino signal compared to the background.

5.2.1 The sliding window method

Implementing a sliding window method can favor the specific behavior of a signal. The sliding window method operates as follows : at each time step, the number of events which occurred within the preceding time interval, called the window, is counted and added to the bin. For the next step, the window is slided forward, by a step size smaller than the window size.

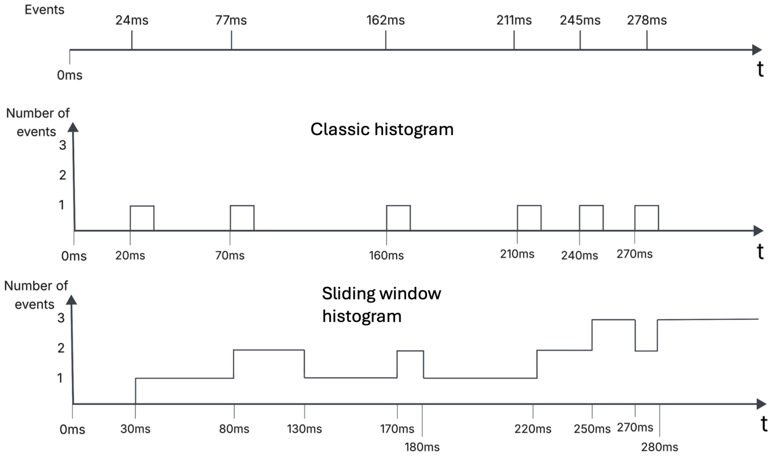

Figure 5.4: Schematic example of the sliding window method with a window size of 100 ms and a step size of 10 ms, compared with a classic histogram of 10 ms bin width.

Using this method, events following each other by a margin closer than the window size generates higher values on the histogram (secondary triggers are not favored since they have been eliminated by the first veto, see chapter 4.2.1). Therefore, with an appropriate choice of window size, this method can be used to favor the specific behavior of CCSN neutrino events.

We now have to choose the parameters of this method : the window and step size. As we saw previously, the probability to have coincident background detections is proportional to the background rate. With that in mind, we would like to choose the window size that maximize two ratio : $\frac{\text{max(signal)}}{\text{max(background)}}$ and $\frac{\text{max(signal)}}{\text{background rate}}$ (see Fig. 5.5). Maximizing the first one ensures that the CCSN neutrinos peak will be much higher than the coincidences due to background and maximizing the second one reduces the probability of occurrence of background peaks. Together, they result in fewer background peaks of lower intensity.
The objective is to select a window size that optimizes both ratios. However, since they increase in opposite directions, a compromise must be made. A window size of 0.225 seconds seems to be a good choice, after the significant increase of the first plot and just before the big downfall of the second plot. This window size value makes sense as it is approximately the duration in which most of neutrinos from CCSN are detected (see Fig. 5.2).
The step size which is the second sliding window parameter, doesn't have a significant impact on the maximum number of events for both the signal and the background. We choose the step size at one tenth of the window size.
Appendix A.5.3 shows an example of the sliding window method effect on the real-time monitor.

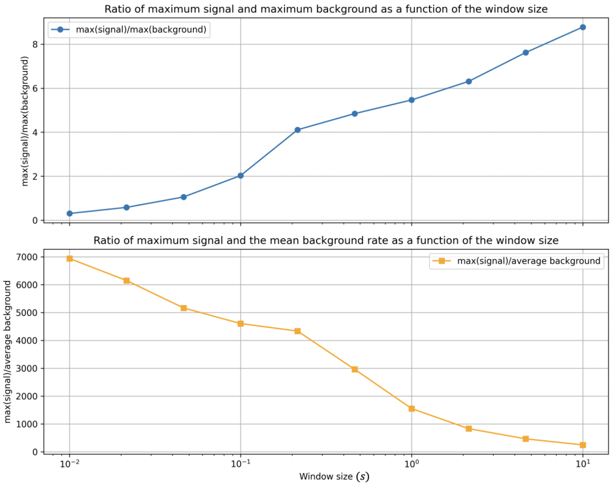

Figure 5.5: Ratio $\frac{\text{max(signal)}}{\text{max(background)}}$ (above) and ratio $\frac{\text{max(signal)}}{\text{background rate}}$ (below), for the half filling of LS data runs, as a function of the window size.

The real-time monitor simulation with the sliding window method takes huge amounts of computational time. In order to reduce it, a file-dividing method, similar to the one presented in Chapter 4.2.2, is used. This time reduction method may seem like a detail, but in practice, even after its implementation, the processing of long data runs still took hours. We can thus expect that without it, the same algorithm would have taken days or even weeks.

5.3 Results

Now that the sliding window method is implemented, we can plot the real-time monitor for different values of the parameter α and the associated nhits range (see appendix A.5.4). Fig. 5.6 shows the real-time monitor for the value of α which gives the best ratio $\frac{\text{max(signal)}}{\text{max(background)}}$ and Fig. 5.7 show the real-time monitor for the nhits range found with the metric M.

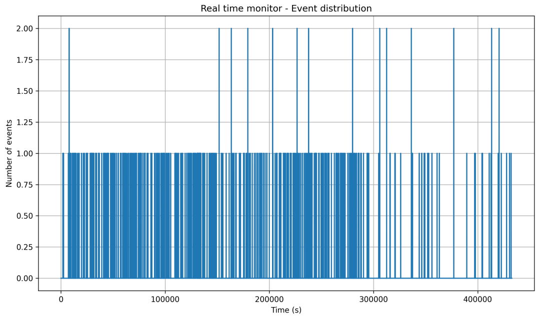

Figure 5.6: Real-time monitor with the background upper bound $\alpha = 10^{-4}$ Hz, in half LS, with background events only.

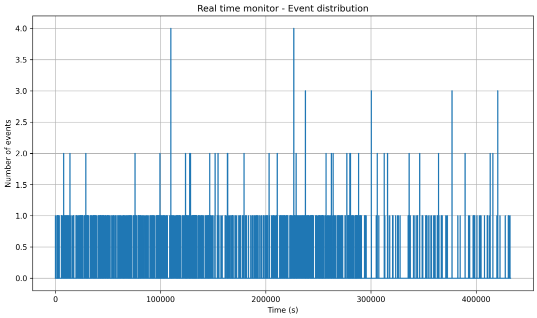

Figure 5.7: Real-time monitor with β optimized through the metric M, in half LS, with background events only.

The CCSN alert will be triggered when the number of events in a window events exceeds a threshold that we need to define. This section aims to find the optimal threshold, which must be low enough to detect CCSN up to 60 kpc, but high enough to avoid false CCSN alerts. Due to the statistical nature of background events, it is impossible to define a threshold that guarantees no false alert. We therefore decide to limit the number of false alert to one per month.

5.3.1 Estimation of the background maximum in a month

Ideally, one month of data runs would have been plotted to obtain its maximum. However, since the LS level is increasing during the commissioning phase, one month of data shows too much differences between the first and the last run.
One solution is to model the background events based on the statistical features of the data runs (for example 99% of bins have 0 events, 0.6% of bins have 1 event, etc.), for the three filling levels which each last a few days, and extend it to estimate the maximum number of background events in the sliding window in one month. Since we have $\frac{1}{0.0225} \cdot 3600 \cdot 24 \cdot 30 \approx 1.15 \cdot 10^9$ windows in a month, the probability that a bin reaches the threshold due to the background must be below $8.68 \cdot 10^{-10}$. To estimate the number of events in a window that corresponds to this probability, the initial approach was to model the number of events distribution by a statistical law. However, every attempts to fit the number of events distribution to a statistical model such as Poisson, Zero-Inflated Poisson or Zero-Inflated Negative Binomial gave inaccurate results and systematically underestimated the probabilities of occurrence of rare events. Therefore, we will perform a non linear regression of this distribution.

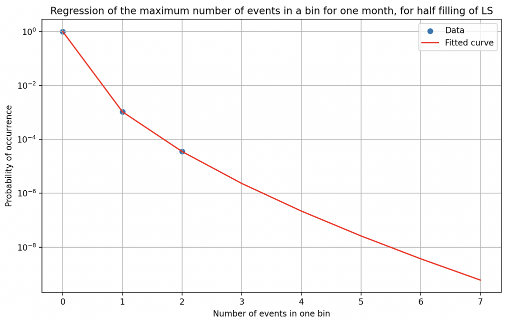

Figure 5.8: Non linear regression of the half filling monitor's data with the background upper bound $\alpha = 10^{-4}$ Hz (Fig. 5.6), to estimate the maximum number of events in a month.

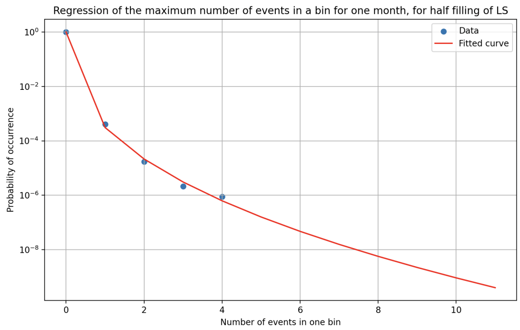

Figure 5.9: Non linear regression of the half filling monitor's data based on M (Fig. 5.7), to estimate the maximum number of events in a month.

Fig. 5.8 and Fig. 5.9 show the regression of the real-time monitor statistics from respectively Fig. 5.6 and Fig. 5.7, based on the regression function $e^{-a \cdot x^b}$ (selected from the observed behavior of the plots).
The regression automatically stops expending when it reaches the probability of one false alert in a month ($P = 8.68 \cdot 10^{-10}$). For the half filling level of LS, the maximum number of simultaneous events in a month is 7 (11 for the M plot). Due to the limited precision of this method, the threshold can be conservatively chosen above this limit, to 8 (12 for the M plot).
Similar regression has been done to evaluate the thresholds for the other LS fillings (see appendix A.5.6). The results of this work are summarized in Table 5.1, where (M) means that the range

has been calculated with the metric M and (α) that it has been determined with the upper bound α for the background rate.

Filling	nhits range (10^4)	CCSN alert threshold
25% LS	$[1.18, 4.15] \cup [4.24, 4.32]$ ($M = 400$)	25 events
25% LS	$[1.16, 1.18] \cup [1.23, 5.05]$ ($\alpha = 10^{-2}$)	27 events
Half LS	$[1.53, 1.56] \cup [1.59, 2.98]$ ($M = 2.25 \cdot 10^4$)	12 events
Half LS	$[1.72, 1.75] \cup [1.79, 1.82] \cup [1.89, 1.93]$ $\cup [1.97, 2.98]$ ($\alpha = 10^{-4}$)	8 events
75% LS	$[1.31, 3.56] \cup [3.64, 3.72]$ ($M = 10^3$)	26 events
75% LS	$[1.26, 1.28] \cup [1.31, 7.04]$ ($\alpha = 10^{-2.5}$)	20 events

Table 5.1: Results of the optimal monitor parameters and the associated CCSN alert threshold.

Analysis of longer stable data runs with full LS, when available, together with a cross-validation method should be conducted to avoid overfitting of the nhits range. Also, a statistical representations which capture the temporal patterns of background (such as a Hawkes model [90], for example) could yield more precise results.

5.3.2 CCSN signal

Let us now show the effect of the sliding window method and the nhits range on the monitor for a 60 kpc CCSN signal, again for half LS (Fig. 5.10 and Fig. 5.11).

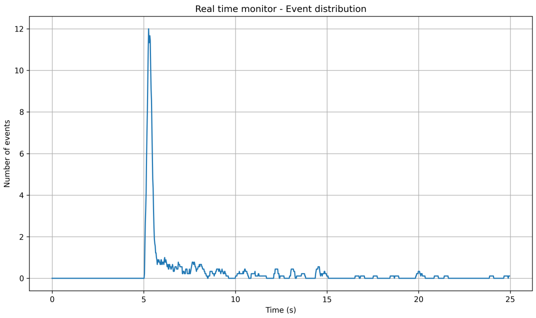

Figure 5.10: Real-time monitor based on $\alpha = 10^{-4}$ Hz, in half LS, for CCSN events only.

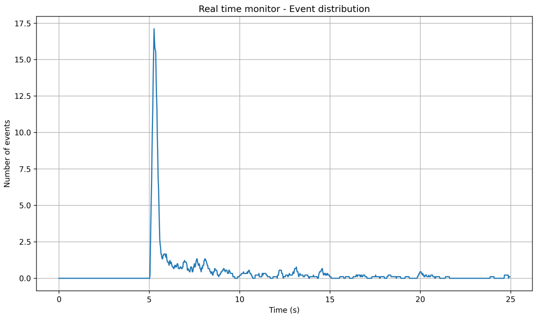

Figure 5.11: Real-time monitor based on $M = 2.25 \cdot 10^4$, in half LS, for CCSN events only.

We can conclude that, using the parameters and the threshold defined above, the monitor would be able to detect CCSN up to 60 kpc with half filling of LS. Let us also remind that the CCSN simulated signal is conservative since it only account for IBD, while elastic scattering also triggers a significant number of events.

This work is intended as a comprehensive guide to build the real-time monitor of JUNO. Since JUNO is still in its commissioning phase and not yet fully filled with LS, the whole analysis in this chapter must therefore be done again once JUNO's filling phase is over and sufficient data runs are available.

Conclusion

This thesis has shown an approach to optimize JUNO's real-time core-collapse supernova (CCSN) monitoring system, with the objective of maximizing the sensitivity to the CCSN neutrino bursts while reducing the events from background sources.

The first chapter has presented the current theory of neutrino physics, the actual knowledge on neutrino parameters and the open questions. After that, we introduced the neutrino observatory used to monitor CCSNe by describing JUNO's architecture and its primary interaction mechanisms. A brief stellar evolution description followed by the current CCSNe theory is addressed, especially in the neutrino emission point of view. These chapters have properly detailed the necessary information to understand the context in which this thesis takes place.

Then, we digged into the signal processing of CCSN neutrinos and JUNO's data runs. First the number of photoelectrons (npe) and the number of hits (nhits) variables were described, giving an understanding of how the energy of the interacting particles can be estimated. The distribution of nhits and npe were presented for the background through the data runs and for the CCSN simulation. These charts allowed us to better understand the link between npe and nhits but above all, they allowed us to see the effects of both vetos on the detection rate of the signal and the background. The first veto accurately removed the secondary triggers while the second one decreased the atmospheric muon rate thanks to the water Cherenkov pool system of JUNO. Due to the long duration of the simulations, a file dividing method was developed to optimize computational time within reasonable limits. After applying both vetos, the background rate significantly decreased while the CCSN signal was not affected too much. This chapter gave the necessary event selection tools to optimize the real-time monitor, but can also be of use in other signal processing applications of JUNO.

The last chapter uses the notions explained in the previous sections to finally build the real-time CCSN monitor. First, an optimal nhits range is calculated by two methods : the first one aims to reduce the background rate in the neutrino region to avoid the model dependency of CCSN neutrino emission, while the second one also maximizes the signal rate. We saw that another difference in signal and background that can be used is the temporal characteristics. A sliding window method implementation has shown to favor the specific behavior of CCSN neutrino blast. Lastly, the maximum number of events due to background in a month is estimates to define the CCSN alert threshold.
With the final detector filling expected to be completed in September 2025, this work ensure that JUNO will be ready to detect the next CCSN in real-time. In this way, the results of this thesis is a step toward maximizing the features of one of the largest neutrino experiments of this decade.

Appendix

A.1 Codes

The main part of the codes used for this work can be found on :
`https://github.com/felixlebg/Master-Thesis-IIHE`

A.2 List of Abbreviations

SM Standard Model

CCSN Core-Collapse Supernovae

CC Charged Current

NC Neutral Current

SK Super-Kamiokande

SNO Sudbury Neutrino Observatory

NMO Neutrino Mass Ordering

NO Normal mass Ordering

IO Inverted mass Ordering

JUNO Jiangmen Underground Neutrino Observatory

NPP Nuclear Power Plant

PMT Photomultiplier Tube

LS Liquide Scintillator

CD Central Detector of JUNO

WP Water Pool veto detector of JUNO

TT Top Tracker veto detector of JUNO

DSNB Diffuse Supernova Neutrino Background

IBD Inverse Beta Decay

PNS Proto-Neutron Star

EoS Equations of State

LS EoS Lattimer–Swesty EoS

SASI Standing Accretion Shock Instability

STIR Stimulated Turbulence in Reduced-Dimensionality

AMR Adaptive Mesh Refinement

SNEWS Supernova Early Warning System

MW Milky Way

LMC Large Magellanic Cloud

SMC Small Magellanic Cloud

npe number of photoelectrons

nhits number of hits

A.3 Standard model and neutrinos

A.3.1 Dirac and Majorana mass

The derivation presented here are inspired by [22]

Dirac mass
The Yukawa Lagrangian, describing how the leptons acquires mass in the SM formalism, is given by the expression :

$$\mathcal{L}_Y(x) = -\sqrt{2} \sum_{l_1, l_2} \bar{\psi}_{l_1 L}(x)\, Y_{l_1 l_2}\, l'_{2R}(x)\, \phi(x) + \text{h.c.} \tag{A.1}$$

where l_j are the flavors (e, μ, τ), $\psi_{l_1 L}(x)$ is the left-handed lepton doublet (containing the left-handed lepton field and the associated left-handed neutrino field), $l'_{2R}(x)$ is the right-handed lepton fields, $Y_{l_1 l_2}$ is the Yukawa coupling matrix and $\phi(x)$ is the Higgs field.

If neutrinos are Dirac particles, a correction of the SM must be done by admitting that neutrino have a sterile right-handed component $\nu'_{l_2 R}$. In this case, we have a similar Lagrangian than for the other leptons, replacing l'_{2R} by $\nu'_{l_2 R}$. The Lagrangian thus becomes, after spontaneous symmetry breaking :

$$\mathcal{L}_Y(x) \xrightarrow{SSB} \sum_{l_1, l_2} \bar{\nu}'_{l_1 L}(x)\, Y_{l_1 l_2}\, \nu'_{l_2 R}(x)(v + H(x)) + \text{h.c.} \tag{A.2}$$

where $H(x)$ is the field of the Higss boson and v is the Higgs vacuum expectation value (vev). Neutrinos in the flavor eigenstate are noted ν_l and in the mass eigenstate ν_i.
After diagonalization $Y = U_L^\dagger\, y\, U_R$, where y is the Yukawa constant of neutrinos, satisfying $y_{l'l} = y_l\, \delta_{l'l}$, we get :

$$\mathcal{L}_Y(x) = \sum_{i=1}^{3} m_i\, \bar{\nu}_{iL}(x)\, \nu_{iR}(x) - \sum_{i=1}^{3} y_i\, \bar{\nu}_{iL}(x)\, \nu_{iR}(x)\, H(x) \tag{A.3}$$

$$\nu_{iL}(x) = U_L^\dagger\, \nu_{lL}(x) \qquad \nu_{iR}(x) = U_R^\dagger \nu_{lR} \tag{A.4}$$

where $m_i = y_i\, v$ is the mass of the neutrino mass state i.
In the expression of the Lagrangian above (A.3), the first term is the mass giving term and the second one describes the interaction between the neutrinos and the Higgs boson. Therefore, the mass giving Lagrangian is :

$$\mathcal{L}_Y(x) = -\sum_{i=1}^{3} m_i \bar{\nu}_{iL}(x) \nu_{iR}(x) + \text{h.c.} \tag{A.5}$$

Majorana mass
If neutrinos are Majorana particles, the mass giving Lagrangian only depends on the left-handed neutrino field :

$$\mathcal{L}_\text{M} = -\frac{1}{2} \sum_{l', l} \bar{\nu}_{l'L}\, M^M\, \nu^c_{lL} \ + \text{h.c.} \tag{A.6}$$

After diagonalization $M^M = U m_M U^\dagger$, where m_M is the Majorana mass :

$$\mathcal{L}_\text{M} = -\frac{1}{2} \sum_{i=1}^{3} m_M\, \bar{\nu}_i\, \nu_i \tag{A.7}$$

$$\nu_i = \sum_{l'} U^\dagger_{il}\nu_{lL} + \sum_{l'} (U^\dagger_{il}\nu_{lL})^c \tag{A.8}$$

where ν^c is the charge conjugate of ν (transformation that switches all particles with their corresponding antiparticles).

A.3.2 The PMNS matrix

The derivation presented here are inspired by [28].
The expression of the PMNS matrix $\mathcal{U}$ can be derived from the weak interaction Lagrangian :

$$\mathcal{L}_W = \frac{g}{\sqrt{2}}\,\bar{l}_{iL}\gamma^\mu \nu_{l_i L} W_\mu + \text{h.c.} \tag{A.9}$$

Where g is the SU(2) coupling constant, γ^μ are the Dirac matrices, ensuring the correct Lorentz contraction between fields, and W_μ is the W boson field.
After the diagonalization of the lepton and the neutrino field, we get :

$$\mathcal{L}_W = \frac{g}{\sqrt{2}}\,\bar{l}_L V_L^\dagger U_L \gamma^\mu \nu_{iL} W_\mu + \text{h.c.} \tag{A.10}$$

where V is the diagonalization matrix of the lepton field and U is the diagonalization matrix of the neutrino field defined above.
We define the PMNS matrix as :

$$\mathcal{U} = V_L^\dagger U_L \tag{A.11}$$

Let us note that in the literature, we can find the PMNS matrix expressed as $\mathcal{U} = U_L$. In this case, the writer work in the flavor eigenstate which simplify the lepton diagonalization matrix $V_L = I$.
If neutrinos are Dirac particles, analogously to the quark mixing matrix, the PMNS matrix can be seen as a rotation in three dimensions, characterized by 3 angles called the mixing angles. In this case, the parametrization reads :

$$\mathcal{U}^D = \begin{pmatrix} c_{12}c_{13} & s_{12}c_{13} & s_{13}e^{-i\delta_{13}} \\ -s_{12}c_{23} - c_{12}s_{23}s_{13}e^{i\delta_{13}} & c_{12}c_{23} - s_{12}s_{23}s_{13}e^{i\delta_{13}} & s_{23}c_{13} \\ s_{12}s_{23} - c_{12}c_{23}s_{13}e^{i\delta_{13}} & -c_{12}s_{23} - s_{12}c_{23}s_{13}e^{i\delta_{13}} & c_{23}c_{13} \end{pmatrix} \tag{A.12}$$

where $c_{ab} = cos\theta_{ab}$ and $s_{ab} = sin\theta_{ab}$. With this parameterization, $\mathcal{U}$ contains 4 parameters : the three mixing angles $\theta_{12}, \theta_{13}, \theta_{23}$ and δ_{13} the CP-violating phase.
If neutrinos prove to be Majorana particles, the mass term Lagrangian A.7 is not invariant under the phase transformation (U(1) gauge symmetry breaking) $\nu_{lL} \rightarrow e^{i\phi}\nu_{lL}$ but in the quark mixing matrix, the assumption of U(1) gauge symmetry allowed to eliminate 2 CP-violating phases by a suitable phase transformation of the quark fields. Therefore, the PMNS matrix of Majorana neutrinos needs to take two additional CP-violating phases, called Majorana phases. In this case, the Dirac PMNS matrix is thus multiplied by a diagonal unitary matrix D^M containing the two Majorana phases.

$$\mathcal{U}^M = \mathcal{U}^D D^M \tag{A.13}$$

A.4 Events selection tools

A.4.1 Relation between height of interaction and number of photoelectrons

The plots of the relation between the height of interaction and the number of photoelectrons for 5% and 25% of LS, with and without the first veto are shown here to better see the interaction peak in water.

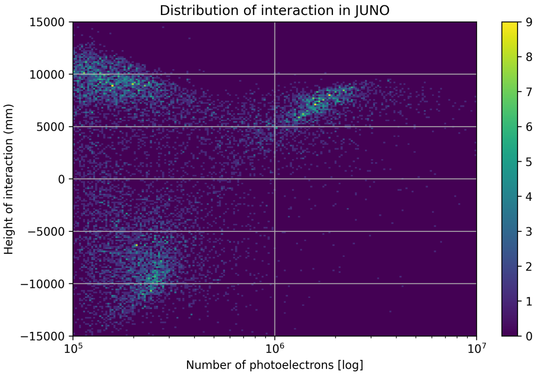

Figure 1: Relation between height of interaction and number of photoelectron with 5% of LS.

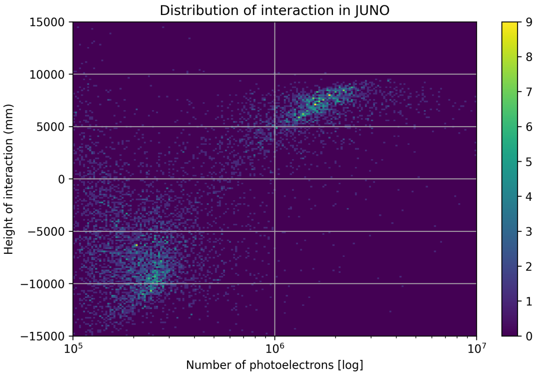

Figure 2: Relation between height of interaction and number of photoelectron with 5% of LS, applying the first veto.

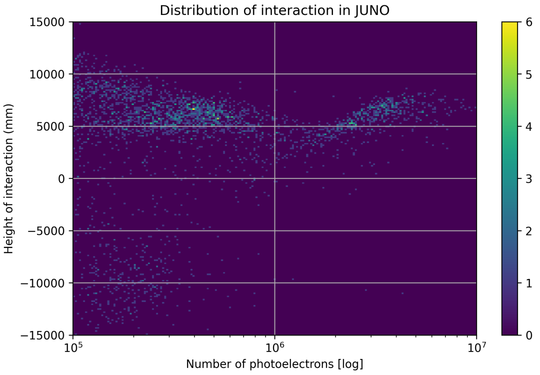

Figure 3: Relation between height of interaction and number of photoelectron with 25% of LS.

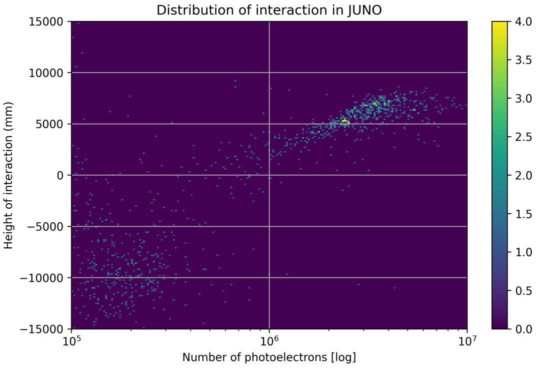

Figure 4: Relation between height of interaction and number of photoelectron with 25% of LS, applying the first veto.

A.4.2 Charge distribution plots

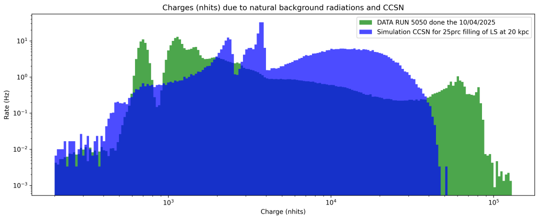

Figure 5: Histogram of the distribution of the nhits rate, with 25% of LS, without vetos

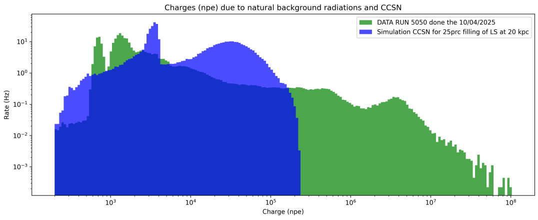

Figure 6: Histogram of the distribution of the nhits rate, with 25% of LS, without vetos.

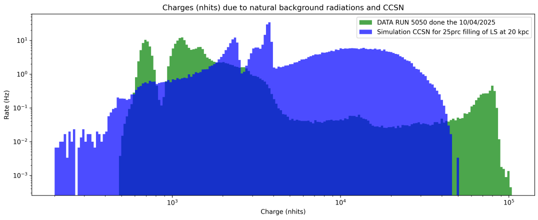

Figure 7: Histogram of the distribution of the nhits rate, with 25% of LS, applying the first veto.

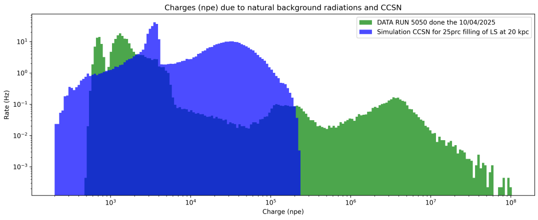

Figure 8: Histogram of the distribution of the npe rate, with 25% of LS, applying the first veto.

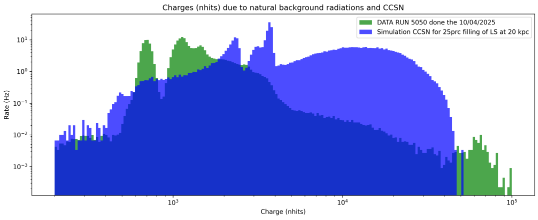

Figure 9: Histogram of the distribution of the nhits rate, with 25% of LS, applying the second veto.

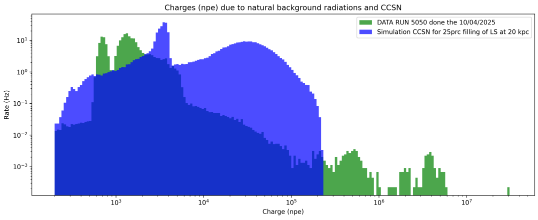

Figure 10: Histogram of the distribution of the npe rate, with 25% of LS, applying the second vetos

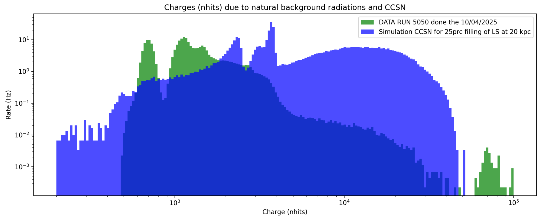

Figure 11: Histogram of the distribution of the nhits rate, with 25% of LS, applying both vetos.

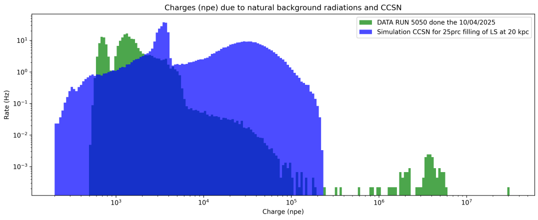

Figure 12: Histogram of the distribution of the npe rate, with 25% of LS, applying both vetos.

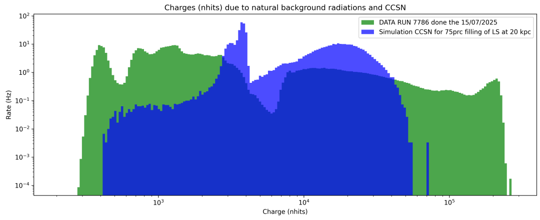

Figure 13: Histogram of the distribution of the nhits rate, with 75% of LS, without vetos

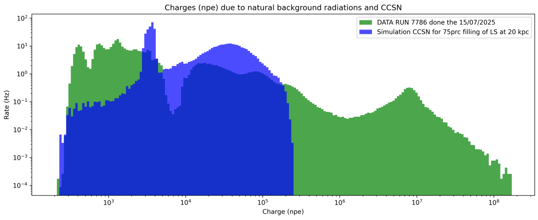

Figure 14: Histogram of the distribution of the nhits rate, with 75% of LS, without vetos.

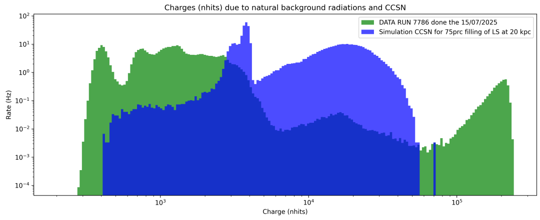

Figure 15: Histogram of the distribution of the nhits rate, with 75% of LS, applying the first veto.

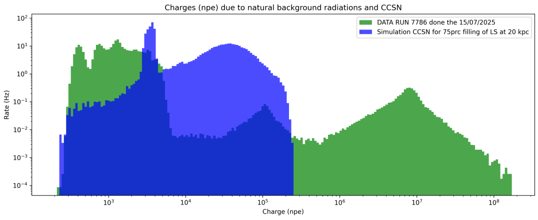

Figure 16: Histogram of the distribution of the npe rate, with 75% of LS, applying the first veto.

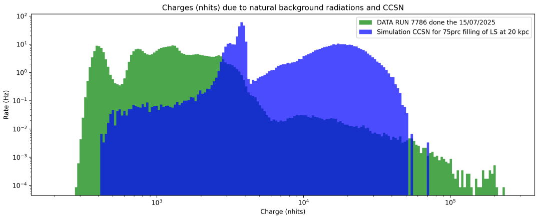

Figure 17: Histogram of the distribution of the nhits rate, with 75% of LS, applying the second veto.

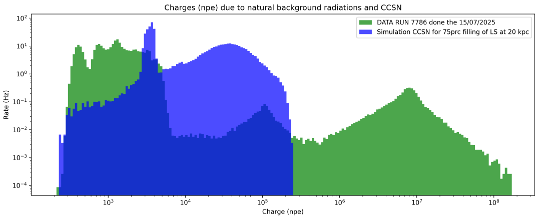

Figure 18: Histogram of the distribution of the npe rate, with 75% of LS, applying the second vetos

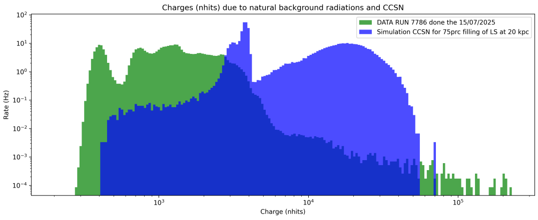

Figure 19: Histogram of the distribution of the nhits rate, with 75% of LS, applying both vetos.

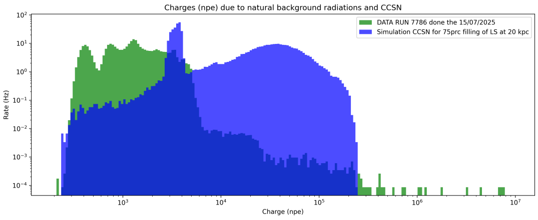

Figure 20: Histogram of the distribution of the npe rate, with 75% of LS, applying both vetos.

A.5 Real time core-collapse supernovae monitor

A.5.1 Optimization of the parameter β

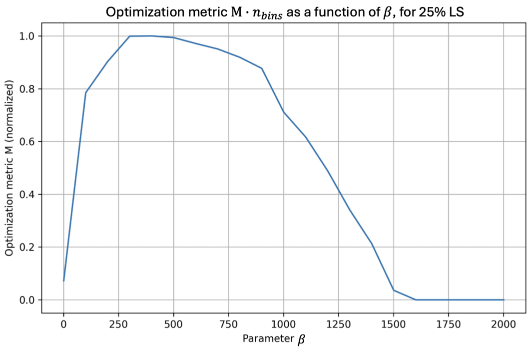

Figure 21: Metric $M \cdot n_{\text{bins}}$ as a function of the parameter β, for 25% LS, applying both vetos.

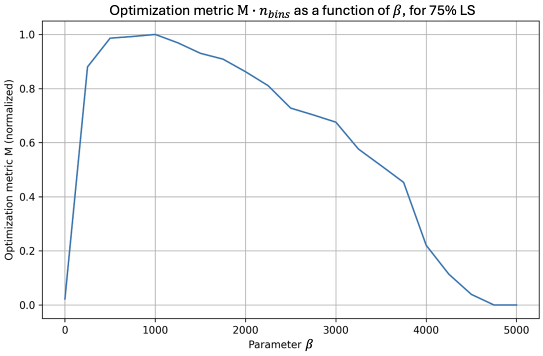

Figure 22: Metric $M \cdot n_{\text{bins}}$ as a function of the parameter β, for 75% LS, applying both vetos.

A.5.2 Window size

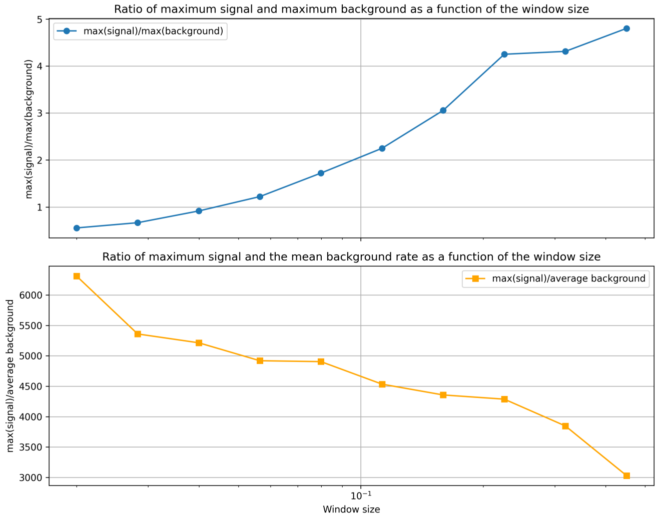

Figure 23: Ratio $\frac{\max(\text{signal})}{\max(\text{background})}$ (above) and ratio $\frac{\max(\text{signal})}{\text{background rate}}$ (below), for half filling background data, zoomed over the interesting values.

A.5.3 Effect of the sliding window method

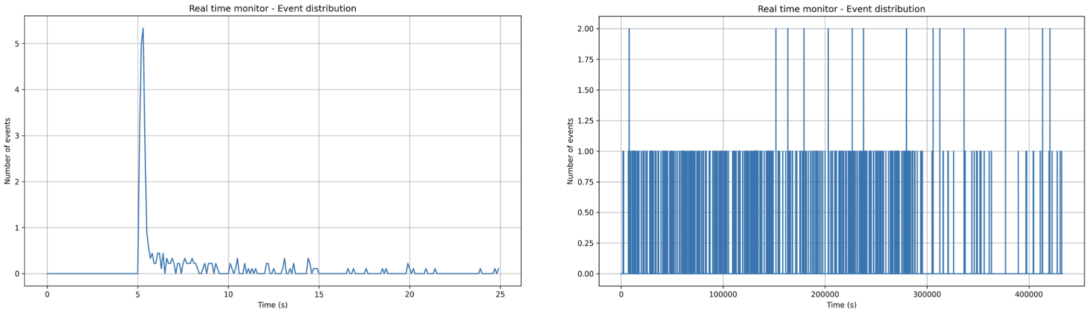

Figure 24: Real-time monitor with $\alpha = 10^{-3.5}$ Hz, for 50% LS, for CCSN and background events, without the sliding window method.

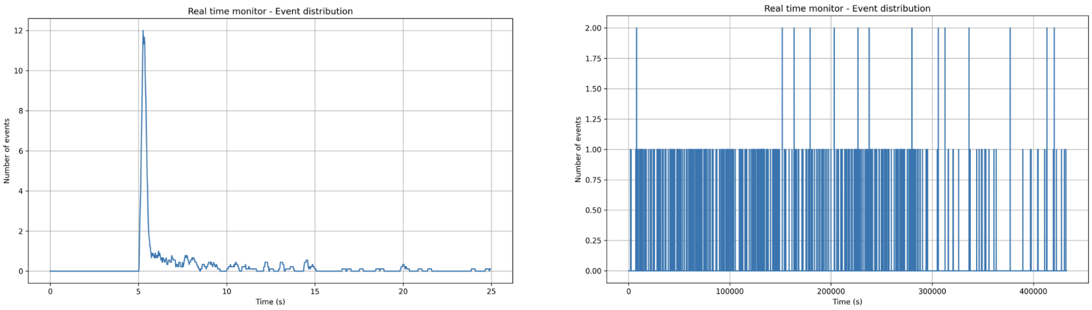

Figure 25: Real-time monitor with $\alpha = 10^{-3.5}$ Hz, for 50% LS, for CCSN and background events, with the sliding window method.

A.5.4 Choice of alpha

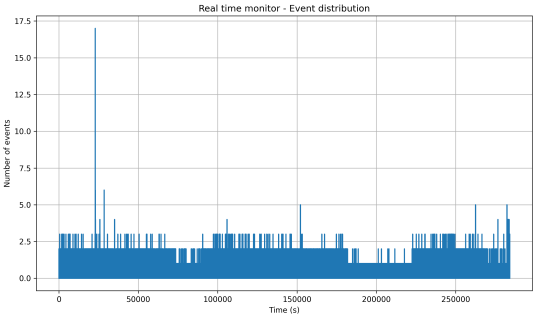

Figure 26: Real-time monitor with $\alpha = 10^{-2}$ Hz, for 25% LS, for background events only.

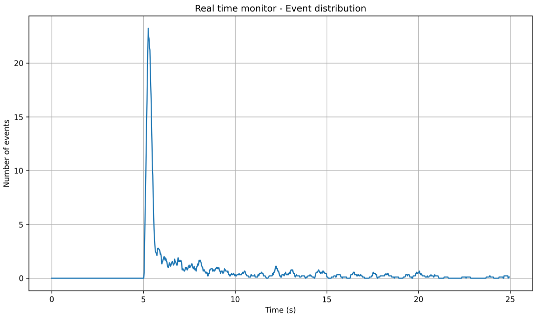

Figure 27: Real-time monitor with $\alpha = 10^{-2}$ Hz, for 25% LS, for CCSN events only.

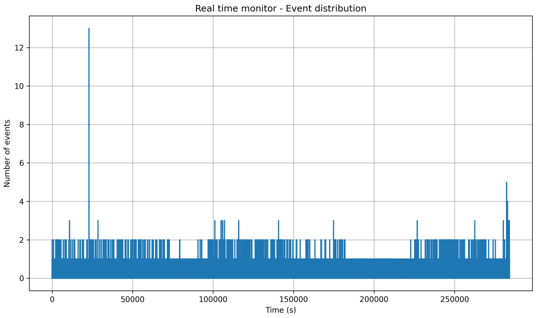

Figure 28: Real-time monitor with $\alpha = 10^{-2.5}$ Hz, for 25% LS, for background events only.

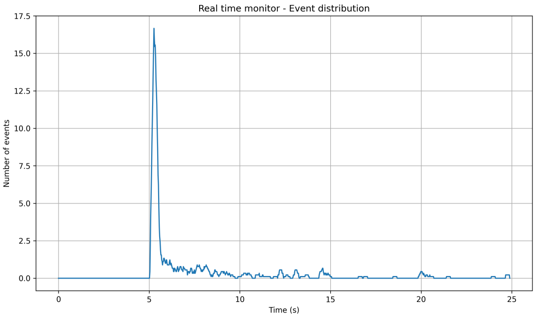

Figure 29: Real-time monitor with $\alpha = 10^{-2.5}$ Hz, for 25% LS, for CCSN events only.

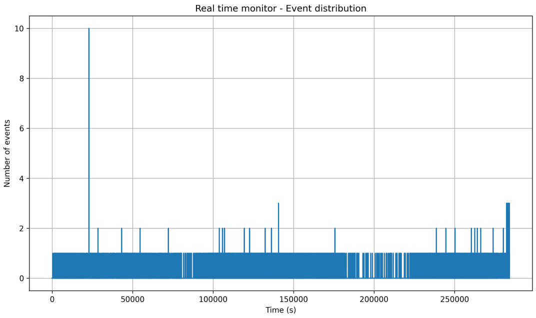

Figure 30: Real-time monitor with $\alpha = 10^{-3}$ Hz, for 25% LS, for background events only.

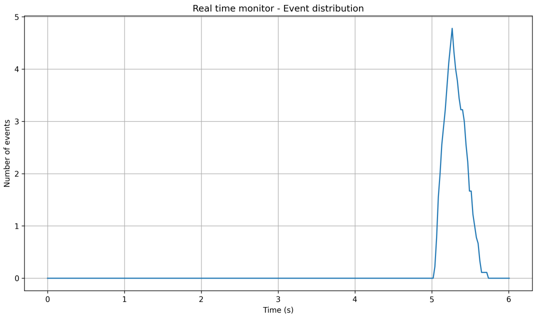

Figure 31: Real-time monitor with $\alpha = 10^{-3}$ Hz, for 25% LS, for CCSN events only.

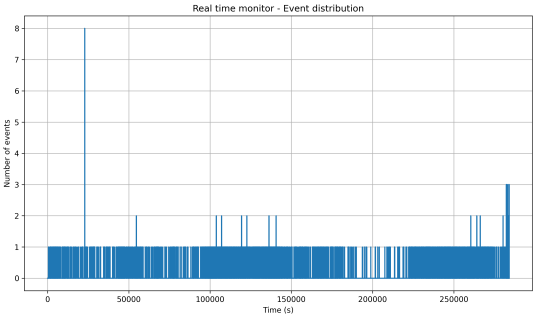

Figure 32: Real-time monitor with $\alpha = 10^{-3.5}$ Hz, for 25% LS, for background events only.

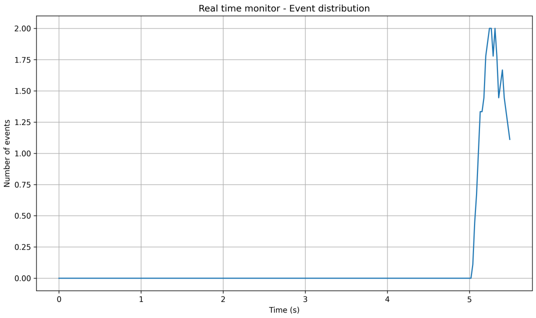

Figure 33: Real-time monitor with $\alpha = 10^{-3.5}$ Hz, for 25% LS, for CCSN events only.

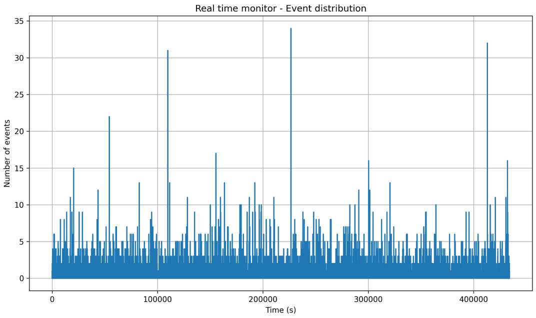

Figure 34: Real-time monitor with $\alpha = 10^{-2}$ Hz, for half LS, for background events only.

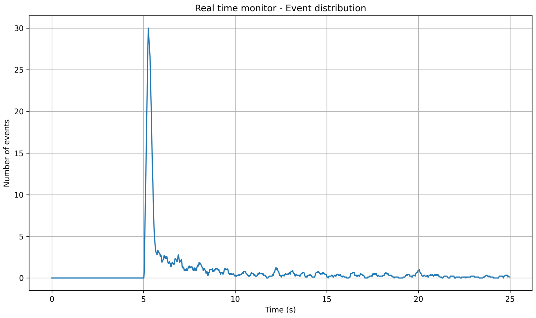

Figure 35: Real-time monitor with $\alpha = 10^{-2}$ Hz, for half LS, for CCSN events only.

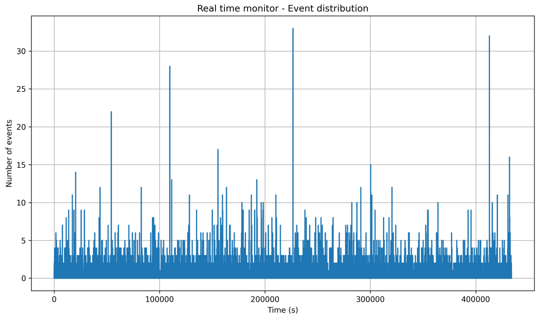

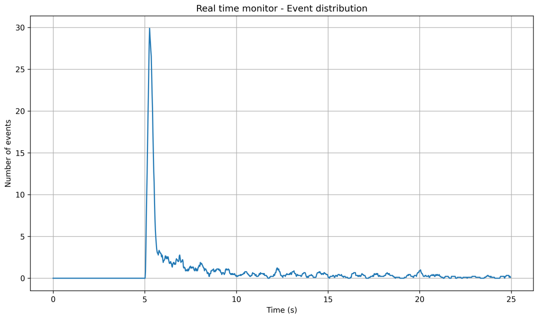

Figure 36: Real-time monitor with $\alpha = 10^{-2.5}$ Hz, for half LS, for background events only.

Figure 37: Real-time monitor with $\alpha = 10^{-2.5}$ Hz, for half LS, for CCSN events only.

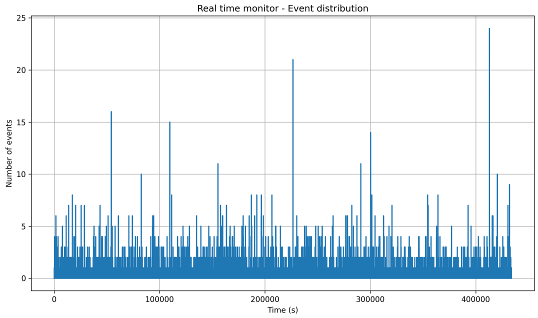

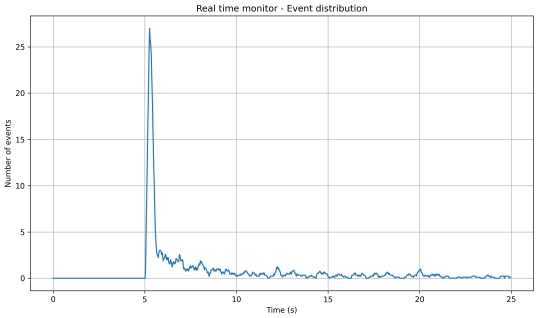

Figure 38: Real-time monitor with $\alpha = 10^{-3}$ Hz, for half LS, for background events only.

Figure 39: Real-time monitor with $\alpha = 10^{-3}$ Hz, for half LS, for CCSN events only.

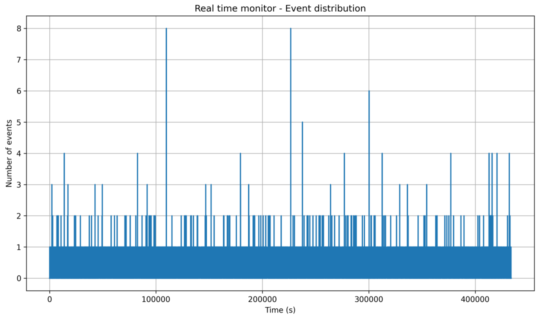

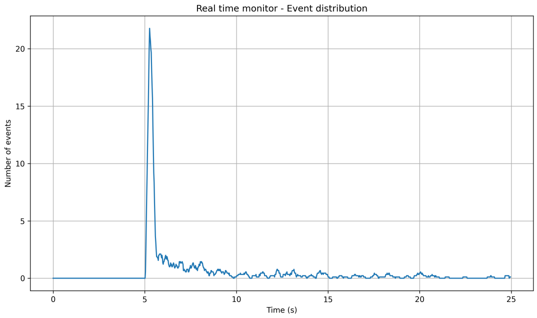

Figure 40: Real-time monitor with $\alpha = 10^{-3.5}$ Hz, for half LS, for background events only.

Figure 41: Real-time monitor with $\alpha = 10^{-3.5}$ Hz, for half LS, for CCSN events only.

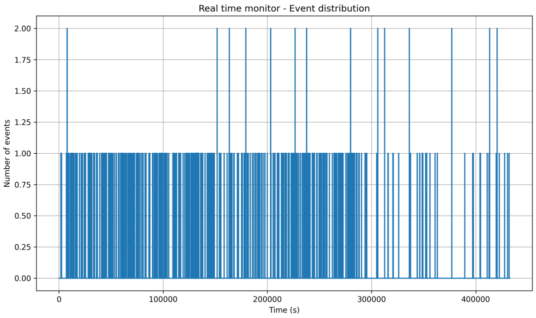

Figure 42: Real-time monitor with $\alpha = 10^{-4}$ Hz, for half LS, for background events only.

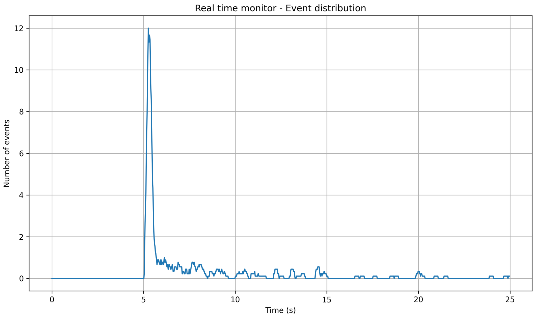

Figure 43: Real-time monitor with $\alpha = 10^{-4}$ Hz, for half LS, for CCSN events only.

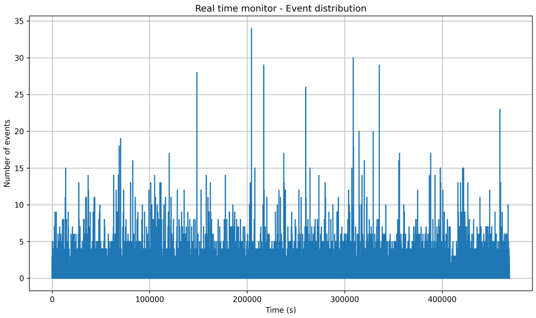

Figure 44: Real-time monitor with $\alpha = 10^{-2}$ Hz, for 76% LS, for background events only.

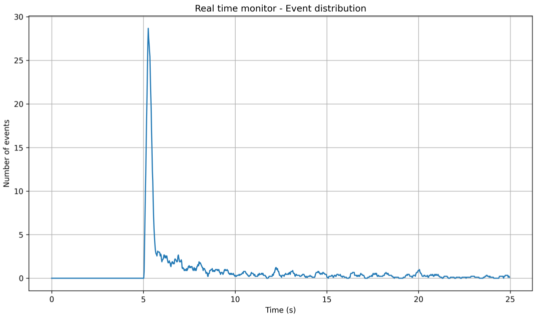

Figure 45: Real-time monitor with $\alpha = 10^{-2}$ Hz, for 76% LS, for CCSN events only.

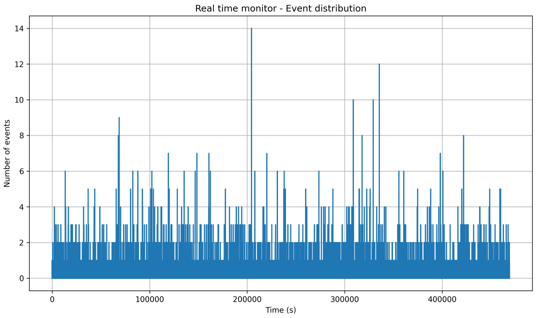

Figure 46: Real-time monitor with $\alpha = 10^{-2.5}$ Hz, for 76% LS, for background events only.

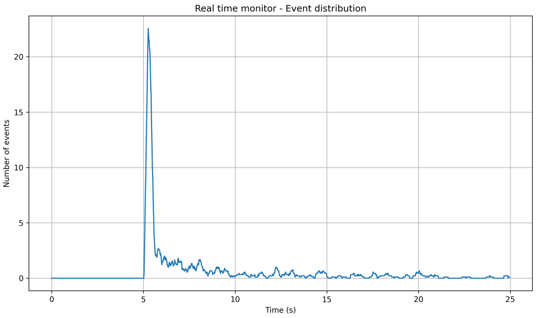

Figure 47: Real-time monitor with $\alpha = 10^{-2.5}$ Hz, for 76% LS, for CCSN events only.

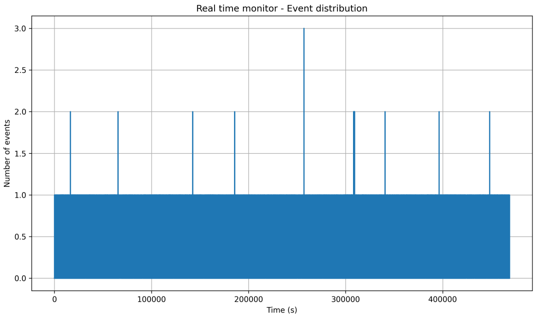

Figure 48: Real-time monitor with $\alpha = 10^{-3}$ Hz, for 76% LS, for background events only.

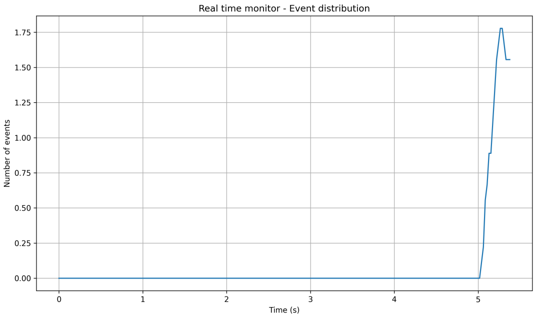

Figure 49: Real-time monitor with $\alpha = 10^{-3}$ Hz, for 76% LS, for CCSN events only.

A.5.5 Monitors with energy range from the metric M

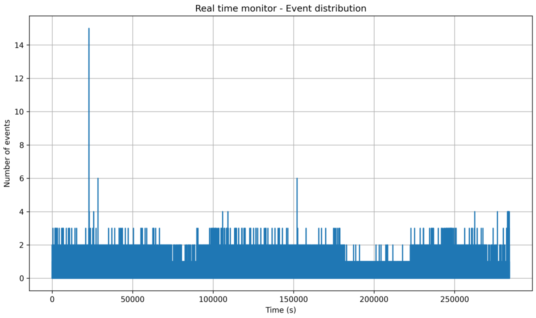

Figure 50: Real-time monitor with $\beta = 400$ optimized through the metric M, for 25% LS, for background only.

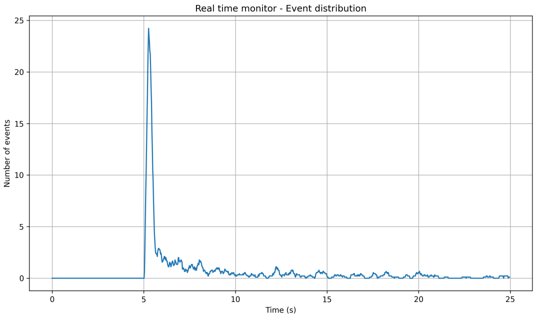

Figure 51: Real-time monitor with $\beta = 400$ optimized through the metric M, for 25% LS, for CCSN neutrinos only.

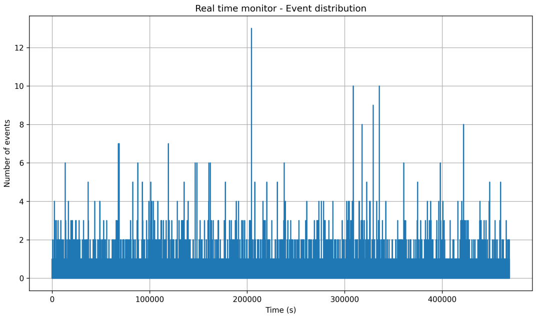

Figure 52: Real-time monitor with $\beta = 10^3$ optimized through the metric M, for 75% LS, for background only.

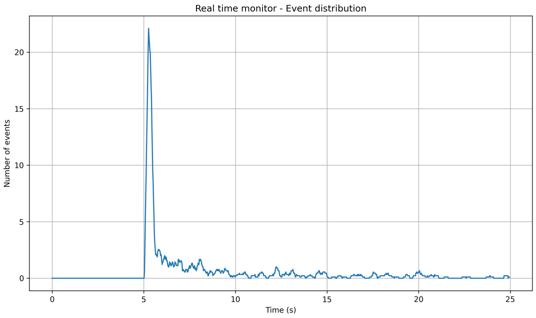

Figure 53: Real-time monitor with $\beta = 10^3$ optimized through the metric M, for 75% LS, for CCSN neutrinos only.

A.5.6 Regression

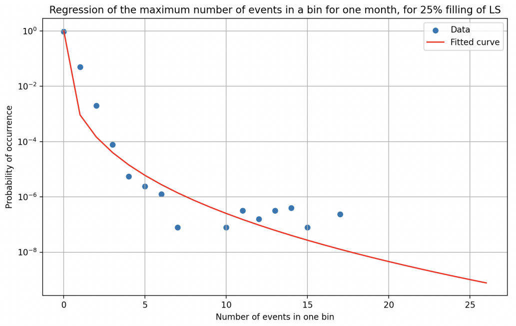

Figure 54: Non linear regression of the 25% filling monitor's data with the background upper bound $\alpha = 10^{-2}$ Hz, to estimate the maximum number of events in a month.

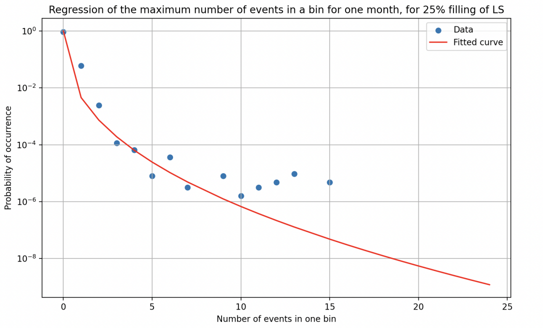

Figure 55: Non linear regression of the 25% filling monitor's data based on M, to estimate the maximum number of events in a month.

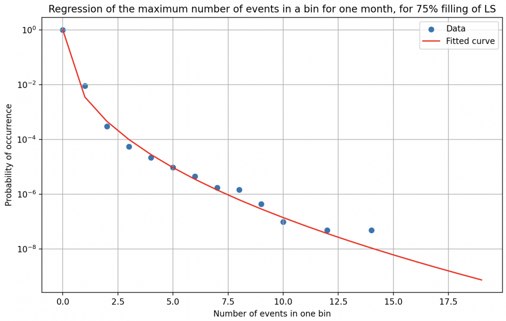

Figure 56: Non linear regression of the 75% filling monitor's data with the background upper bound $\alpha = 10^{-2.5}$ Hz, to estimate the maximum number of events in a month.

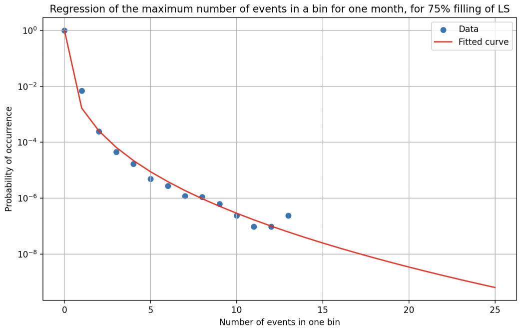

Figure 57: Non linear regression of the 75% filling monitor's data based on M, to estimate the maximum number of events in a month.

Due to the sliding window method, a window with a large number of events will most of the time be surrounded by several window with less events, which can modify the probability distribution. Removing this dispersion around rare events or using a statistical model based on temporal behavior of the data runs could remove this bias.

A.5.7 Flashers

Flashers in the PMTs inducing false muons signals, which have no corresponding signal in the WP. This additional background induces an artificial reduction in the detection efficiency of muons. As the JUNO team has tried different hardware conditions to avoid flashers, the muon detection efficiency has changed over the commissioning phase.

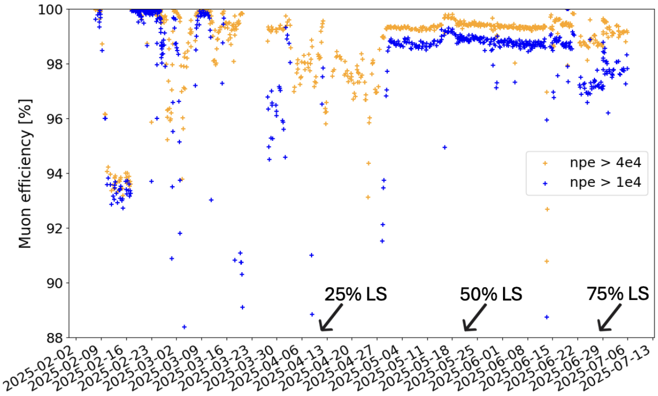

Figure 58: Muon detection efficiency as a function of the date.

Fig. 58 shows less efficiency in muon detection for 25% and 75% LS, which could be an explanation for the differences of the CCSN threshold in the Table 5.1.
Implementing a third veto which tracks flashers in the PMTs would reduce the background.

Bibliography

[1] Théo Guide. *Study of the JUNO experiment sensitivity to the determination of the neutrino mass ordering when observing neutrino signals from core-collapse supernovae.* Inter University Institute of High Energy, 2023. URL: `https://iihe.ac.be/sites/default/files/thesis-theo-guide-juno-master-2023pdf/thesis-theo-guide-juno-master-2023.pdf`.
Information about JUNO, CCSN and neutrino in the Standard Model.

[2] Pierre-Alexandre PETITJEAN. "Development and tests of JUNO electronics readout system and study of JUNO performance for core collapse supernova model discrimination". In: *Annalen der physik* (2024). URL: `https://iihe.ac.be/sites/default/files/thesis-pierre-alexandre-petitjean-juno-phd-2024pdf/thesis-pierre-alexandre-petitjean-juno-phd-2024.pdf`.
Neutrino and model standard informations.

[3] Wikipédia. *Standard model.* URL: `https://en.wikipedia.org/wiki/Standard_Model`.
Schema of the standard model particles.

[4] Ahmed Tarek Abouelfadl Mohamed. "The Standard Model of Particle Physics". In: *Measurement of Higgs Boson Production Cross Sections in the Diphoton Channel: with the full ATLAS Run-2 Data and Constraints on Anomalous Higgs Boson Interactions.* Cham: Springer International Publishing, 2020, pp. 3–35. ISBN: 978-3-030-59516-6. DOI: `10.1007/978-3-030-59516-6_1`. URL: `https://doi.org/10.1007/978-3-030-59516-6_1`.
Standard model.

[5] François Englert and Robert Brout. "Broken Symmetries and the Masses of Gauge Bosons". In: *Phys. Rev. Lett. 13, 321* (Aug. 1964). DOI: `https://doi.org/10.1103/PhysRevLett.13.321`. URL: `https://journals.aps.org/prl/abstract/10.1103/PhysRevLett.13.321`.
François Englert and Robert Brout paper about the Higgs mechanism.

[6] Peter W. Higgs. "Broken Symmetries and the Masses of Gauge Bosons". In: *Phys. Rev. Lett. 13, 508* (Oct. 1964). DOI: `https://doi.org/10.1103/PhysRevLett.13.508`. URL: `https://journals.aps.org/prl/abstract/10.1103/PhysRevLett.13.508`.
Peter W. Higgs paper about the Higgs mechanism.

[7] G. S. Guralnik, C. R. Hagen, and T. W. B. Kibble. "Global Conservation Laws and Massless Particles". In: *Phys. Rev. Lett. 13, 585* (Nov. 1964). DOI: `https://doi.org/10.1103/PhysRevLett.13.585`. URL: `https://journals.aps.org/prl/abstract/10.1103/PhysRevLett.13.585`.
Guralnik et al. paper on the Higgs mechanism.

[8] G. Aad et al. “Observation of a new particle in the search for the Standard Model Higgs boson with the ATLAS detector at the LHC”. In: *Physics Letters B* 716.1 (Sept. 2012), pp. 1–29. ISSN: 0370-2693. DOI: `10.1016/j.physletb.2012.08.020`. URL: `http://dx.doi.org/10.1016/j.physletb.2012.08.020`.
Higgs boson discovery at LHC CERN.

[9] Michael Altmann et al. *Neutrino Astrophysics*. Institute of High Energy Physics, Chinese Academy of Sciences and Tsinghua Uviversity, 1998. URL: `https://cds.cern.ch/record/345846/files/9801320.pdf`.
Compute a solar neutrino flux at Earth of about $6 \cdot 10^{10}\text{cm}^{-2}\text{s}^{-1}$ and the energy range of reactor antineutrinos, atmospheric neutrinos and solar neutrinos.

[10] S. Simon. *Radiation protection - Lecture notes*. Ecole Polytechnique de Bruxelles - ULB, 2020.
Information about natural radiations and stopping power of the electrons.

[11] Neutrino observatory IceCube. *Neutrino history*. URL: `https://icecube.wisc.edu/category/neutrino-history/`.
History of neutrinos.

[12] Pauly Nicolas. *Introductory Nuclear Physics - Lecture notes*. Ecole Polytechnique de Bruxelles - ULB, 2023.
Information about nuclear processes, especially Beta decay.

[13] Seth H. Neddermeyer and Carl D. Anderson. “Note on the Nature of Cosmic-Ray Particles”. In: *Physical Review, Volume 51, Issue 10* (1937), pp. 884–886. URL: `https://journals.aps.org/pr/abstract/10.1103/PhysRev.51.884`.
Discovery of muon in cosmic ray shower.

[14] M. L. Perl et al. “Evidence for Anomalous Lepton Production in $e^+ - e^-$ Annihilation”. In: *Physical Review Letters* 35 (22 1975), pp. 1489–1492. DOI: `10.1103/PhysRevLett.35.1489`. URL: `https://link.aps.org/doi/10.1103/PhysRevLett.35.1489`.
Discovery of tau at SLAC with SPEAR collider.

[15] Raymond Davis. *A Review of the Homestake Solar Neutrino Experiment*. Astronomy Department, Universityof Pennsylvania, 15hiladelphia, PA 19104-6394, U.S.A, 1994. URL: `https://www.sciencedirect.com/science/article/abs/pii/0146641094900043?fr=RR-2&ref=pdf_download&rr=94e9b4172fc6e288`.
Homestake experiment explanation.

[16] Jorissen Alain. *Astrophysique - Lecture notes*. Faculté de Physique - ULB, 2022.
Stellar evolution, main sequence and CCSN infromations.

[17] John N. Bahcall and Raymond Davis. *Solar Neutrinos: A Scientific Puzzle*. 1976, pp. 264–267. URL: `https://www.science.org/doi/10.1126/science.191.4224.264`.
Solar neutrino problem explanation.

[18] Bruno Pontecorvo. “Mesonium and anti-mesonium”. In: *Sov. Phys. JETP 6* (1957).
First idea of neutrino oscillation, where neutrino can transform into anti-neutrino.

[19] Bruno Pontecorvo. “Neutrino experiments and the problem of conservation of leptonic”. In: *Sov. Phys. JETP 26* (1968).
After the discovery of neutrino flavours, extension of the paper ”Mesonium and anti-mesonium” to flavour oscillation.

[20] Y.Fukudaa, T.Hayakawaa, and E.Ichiharaa. *Evidence for oscillation of atmospheric neutrinos.* The Super-Kamiokande Collaboration, 1998. URL: `https://ui.adsabs.harvard.edu/abs/1998PhRvL..81.1562F/abstract`.
Neutrino oscillation evidences.

[21] Nick Jelley, Arthur B. McDonald, and R.G. Hamish Robertson. *The Sudbury Neutrino Observatory.* Oxford University, Queen's University of Kingston, and University of Washington, 2002. URL: `https://www.annualreviews.org/content/journals/10.1146/annurev.nucl.55.090704.151550`.
Neutrino oscillation evidences.

[22] Samoil M. Bilenky. *Neutrinos : Majorana or Dirac?* Joint Institute for Nuclear Research, R-141980 Dubna, Russia and TRIUMF, 4004 Wesbrook Mall, Vancouver, BC V6T 2A3, Canada, 2020. URL: `https://www.mdpi.com/2218-1997/6/9/134`.
Discussion about the neutrino having a Dirac or a Majorana mass.

[23] A. Agrawal et al. "Improved Limit on Neutrinoless Double Beta Decay of neutrinoless Mo[100] from AMoRE-I". In: *Physical Review Letters* 134.8 (2025). ISSN: 1079-7114. DOI: `10.1103/physrevlett.134.082501`. URL: `http://dx.doi.org/10.1103/PhysRevLett.134.082501`.
Recent neutrinoless double beta decay research.

[24] G. Arnison et al. "Experimental observation of isolated large transverse energy electrons with associated missing energy at $\sqrt{s}$=540 GeV". In: *Physics Letters B* 122.1 (1983), pp. 103–116. ISSN: 0370-2693. DOI: `https://doi.org/10.1016/0370-2693(83)91177-2`. URL: `https://www.researchgate.net/publication/29514818_Experimental_observation_of_events_with_large_missing_transverse_energy_accompanied_by_a_jet_or_a_photon_S_in_pp_collisions_at_s_540_GeV`.
W boson discovery at CERN with the estimation of its mass.

[25] Larisa A. Thorne. *Neutrino mass experiments: current and future.* Johannes Gutenberg University Mainz, 2024. URL: `https://arxiv.org/html/2411.08542v1`.
Explain the main methods to estimate neutrino mass.

[26] M. Aker et al. *Direct neutrino-mass measurement based on 259 days of KATRIN data.* 2024. arXiv: `2406.13516 [nucl-ex]`. URL: `https://arxiv.org/abs/2406.13516`.
Direct measurement of the electron neutrino mass from the KATRIN experiment.

[27] A.G. Adame et al. "DESI 2024 VI: cosmological constraints from the measurements of baryon acoustic oscillations". In: *Journal of Cosmology and Astroparticle Physics* 2025.02 (Feb. 2025), p. 021. ISSN: 1475-7516. DOI: `10.1088/1475-7516/2025/02/021`. URL: `http://dx.doi.org/10.1088/1475-7516/2025/02/021`.
Cosmological constraint on the sum of neutrino masses.

[28] Carlo Giunti and Chung W. Kim. *Fundamentals of Neutrino Physics and Astrophysics.* Oxford, 2022, pp. 183–211.
Derive the PMNS matrix for Dirac and Majorana neutrinos.

[29] Robert Mann. *An Introduction to Particle Physics and the Standard Model.* Taylor & Francis, 2010. URL: `https://directory.doabooks.org/handle/20.500.12854/72208`.
Neutrino oscillation equations.

[30] Kai Zuber. *Neutrino physics.* Taylor & Francis, 2020. DOI: `10.1201/9781315195612`. URL: `https://library.oapen.org/viewer/web/viewer.html?file=/bitstream/handle/20.500.12657/101033/9781351764582.pdf?sequence=1&isAllowed=y`.
Energy range of solar neutrinos, atmospheric neutrinos and reactor antineutrinos.

[31] Y. Abe et al. "Indication of Reactor $\overline{\nu}_e$ Disappearance in the Double Chooz Experiment". In: *Phys. Rev. Lett.* 108 (13 Mar. 2012), p. 131801. DOI: `10.1103/PhysRevLett.108.131801`. URL: `https://journals.aps.org/prl/abstract/10.1103/PhysRevLett.108.131801`.

[32] Jinjing Li. "Daya Bay neutrino oscillation progress based on neutron captured on hydrogen". In: *Proceedings of 40th International Conference on High Energy physics — PoS(ICHEP2020).* Sissa Medialab, Jan. 2024, p. 207. DOI: `10.22323/1.390.0207`. URL: `http://dx.doi.org/10.22323/1.390.0207`.

[33] J.S. Park et al. "Production and optical properties of Gd-loaded liquid scintillator for the RENO neutrino detector". In: *Nuclear Instruments and Methods in Physics Research Section A: Accelerators, Spectrometers, Detectors and Associated Equipment* 707 (2013), pp. 45–53. ISSN: 0168-9002. DOI: `https://doi.org/10.1016/j.nima.2012.12.121`. URL: `https://www.sciencedirect.com/science/article/pii/S0168900213000168`.

[34] IceCube Collaboration. *Measurement of atmospheric neutrino oscillation parameters using convolutional neural networks with 9.3 years of data in IceCube DeepCore.* 2024. arXiv: `2405.02163 [hep-ex]`. URL: `https://arxiv.org/abs/2405.02163`.
IceCube values for atmospheric neutrinos oscillation parameter.

[35] T. Wester et al. "Atmospheric neutrino oscillation analysis with neutron tagging and an expanded fiducial volume in Super-Kamiokande I–V". In: *Physical Review D* 109.7 (2024). ISSN: 2470-0029. DOI: `10.1103/physrevd.109.072014`. URL: `http://dx.doi.org/10.1103/PhysRevD.109.072014`.
Super-Kamiokande values for atmospheric neutrinos oscillation parameter.

[36] Y. Suzuki. "The Super-Kamiokande experiment". In: *Eur. Phys. J. C 79, 298* (2019). URL: `https://doi.org/10.1140/epjc/s10052-019-6796-2`.
Super-Kamiokande values for solar neutrinos oscillation parameter.

[37] M.C. Chen. "The SNO Liquid Scintillator Project". In: *Nuclear Physics B - Proceedings Supplements* 145 (2005). NOW 2004, pp. 65–68. ISSN: 0920-5632. DOI: `https://doi.org/10.1016/j.nuclphysbps.2005.03.037`. URL: `https://www.sciencedirect.com/science/article/pii/S0920563205004755`.

[38] G. Bellini et al. "Final results of Borexino Phase-I on low-energy solar neutrino spectroscopy". In: *Phys. Rev. D* 89 (11 June 2014), p. 112007. DOI: `10.1103/PhysRevD.89.112007`. URL: `https://link.aps.org/doi/10.1103/PhysRevD.89.112007`.

[39] Tomáš Nosek. *The NOvA Experiment and Neutrino Oscillations.* 2022. URL: `https://indico.cern.ch/event/1154836/contributions/4849060/attachments/2433808/4168159/TNosek_NOvA_WUF_talk.pdf`.
Nova and T2K experiment, using accelerators for $/delta_{CP}$ measurement and NMO.

[40] Peter B. Denton. "Probing CP Violation with Neutrino Disappearance Alone". In: *Phys. Rev. Lett.* 133 (3 July 2024), p. 031801. DOI: `10.1103/PhysRevLett.133.031801`. URL: `https://link.aps.org/doi/10.1103/PhysRevLett.133.031801`. More recent method to measure $/delta_{CP}$.

[41] I. Esteban et al. *Nu-FIT6.0.* 2024. URL: `http://www.nu-fit.org/?q=node/294#label85`. Lattest numerical values of neutrino parameters.

[42] Pablo F. de Salas et al. "Neutrino Mass Ordering from Oscillations and Beyond: 2018 Status and Future Prospects". In: *Frontiers in Astronomy and Space Sciences* 5 (Oct. 2018). ISSN: 2296-987X. DOI: `10.3389/fspas.2018.00036`. URL: `http://dx.doi.org/10.3389/fspas.2018.00036`.

[43] Laura Herold and Marc Kamionkowski. "Revisiting the impact of neutrino mass hierarchies on neutrino mass constraints in light of recent DESI data". In: *Physical Review D* 111.8 (2025). ISSN: 2470-0029. DOI: `10.1103/physrevd.111.083518`. URL: `http://dx.doi.org/10.1103/PhysRevD.111.083518`.
Neutrino mass upper and lower constraint depending on the NMO.

[44] Anushree Ghosh, Tarak Thakore, and Sandhya Choubey. "Determining the neutrino mass hierarchy with INO, T2K, NOvA and reactor experiments". In: *Journal of High Energy Physics* 2013.4 (Apr. 2013). ISSN: 1029-8479. DOI: `10.1007/jhep04(2013)009`. URL: `http://dx.doi.org/10.1007/JHEP04(2013)009`.
NMO determination with matter effects.

[45] Fengpeng An et al. "Neutrino physics with JUNO". In: *Journal of Physics G: Nuclear and Particle Physics* (Feb. 2016), p. 030401. URL: `https://arxiv.org/pdf/1507.05613`.
Neutrino physics information in JUNO.

[46] T. Adam et al. *JUNO Conceptual Design Report.* 2015. arXiv: `1508.07166 [physics.ins-det]`. URL: `https://arxiv.org/abs/1508.07166`.
Contains information about JUNO design and the justification.

[47] JUNO Collaboration. *JUNO Physics and Detector.* JUNO Collaboration, 2021. URL: `https://arxiv.org/abs/2104.02565`.
Information about JUNO.

[48] Angel Abusleme et al. "Potential to identify neutrino mass ordering with reactor antineutrinos at JUNO". In: *Chinese Physics C* 49.3 (Mar. 2025), p. 033104. ISSN: 2058-6132. DOI: `10.1088/1674-1137/ad7f3e`. URL: `http://dx.doi.org/10.1088/1674-1137/ad7f3e`.
Statistics on the NMO determination with JUNO.

[49] Angel Abusleme et al. "Prediction of energy resolution in the JUNO experiment*". In: *Chinese Physics C* 49.1 (Jan. 2025), p. 013003. ISSN: 2058-6132. DOI: `10.1088/1674-1137/ad83aa`. URL: `http://dx.doi.org/10.1088/1674-1137/ad83aa`.
Energy resolution needed to achieve the goals of the JUNO experiment.

[50] Angel Abusleme et al. "Calibration strategy of the JUNO experiment". In: *Journal of High Energy Physics* 2021.3 (Mar. 2021). ISSN: 1029-8479. DOI: `10.1007/jhep03(2021)004`. URL: `http://dx.doi.org/10.1007/JHEP03(2021)004`.
Calibration system of JUNO.

[51] Angel Abusleme et al. "The JUNO experiment Top Tracker". In: *Nuclear Instruments and Methods in Physics Research Section A: Accelerators, Spectrometers, Detectors and Associated Equipment* (Dec. 2023), p. 168680. URL: `https://arxiv.org/abs/2303.05172`.
Top Tracker design.

[52] E. Kolbe, K. Langanke, and P. Vogel. *Weak reactions on Carbone 12 within the Continuum Random Phase Approximation with partial occupancies.* Institut für Physik, Universität Basel, Basel, Switzerland et al., 1999. URL: `https://arxiv.org/pdf/nucl-th/9903022`.
Weak interaction reactions of muons and neutrinos with Carbone 12 which is the main component in the organic LS.

[53] Francesco L. Villante et al. "The chemical composition of the sun from helioseismic and solar neutrino data". In: *The Astrophysical Journal* 787.1 (Apr. 2014), p. 13. ISSN: 1538-4357. DOI: `10.1088/0004-637x/787/1/13`. URL: `http://dx.doi.org/10.1088/0004-637X/787/1/13`.
Explain how the different neutrino fluxes values can be used to constraint the metalicity of the sun.

[54] William J Marciano and Zohreh Parsa. "Neutrino–electron scattering theory". In: *Journal of Physics G: Nuclear and Particle Physics* 29.11 (Oct. 2003), pp. 2629–2645. ISSN: 1361-6471. DOI: `10.1088/0954-3899/29/11/013`. URL: `http://dx.doi.org/10.1088/0954-3899/29/11/013`.
NC and CC neutrino-electron elastic scattering interactions.

[55] Pauly Nicolas. *Nuclear measurement techniques - Lecture notes.* Ecole Polytechnique de Bruxelles - ULB, 2023.
Information about Cherenkov effect.

[56] S. Abe et al. "Production of radioactive isotopes through cosmic muon spallation in KamLAND". In: *Physical Review C* 81.2 (Feb. 2010). ISSN: 1089-490X. DOI: `10.1103/physrevc.81.025807`. URL: `http://dx.doi.org/10.1103/PhysRevC.81.025807`.
^{9}Li/^{8}He production cross section at the KamLAND detector.

[57] Bei Zhou and John F. Beacom. "First detailed calculation of atmospheric neutrino foregrounds to the diffuse supernova neutrino background in Super-Kamiokande". In: *Physical Review D* 109.10 (May 2024). ISSN: 2470-0029. DOI: `10.1103/physrevd.109.103003`. URL: `http://dx.doi.org/10.1103/PhysRevD.109.103003`.
Muon decay impact on neutrino detector.

[58] Davide Basilico et al. *Update on single events spectrum analysis.* 2025.
Research on the soil adioactivity peaks measured by JUNO.

[59] Amanda I. Karakas. "Low- and Intermediate-Mass Stars". In: *Handbook of Supernovae.* Ed. by Athem W. Alsabti and Paul Murdin. Cham: Springer International Publishing, 2017, pp. 461–481. ISBN: 978-3-319-21846-5. DOI: `10.1007/978-3-319-21846-5_117`. URL: `https://doi.org/10.1007/978-3-319-21846-5_117`.
Stellar evolution of low and intermediate-mass stars.

[60] Behnaz Nouhi et al. "The fusion–fission optimization (FuFiO) algorithm". In: *Scientific reports* (2022). URL: `https://doi.org/10.1038/s41598-022-16498-4`.
Bindinge enrgy of nuclei to highlight fusion/fission.

[61] Jason Kendall - Full Member of the American Astronomical Society. *Stellar evolution overview.* 2018. URL: `https://images.app.goo.gl/MZkEeF7Af4zH5V699`.
Schema of the different paths of a star's life, depending on the mass.

[62] H. A. Bethe. "Supernova mechanisms". In: *Rev. Mod. Phys.* 62 (4 Oct. 1990), pp. 801–866. DOI: `10.1103/RevModPhys.62.801`. URL: `https://link.aps.org/doi/10.1103/RevModPhys.62.801`.
CCSN physics.

[63] J. R. Oppenheimer and G. M. Volkoff. "On Massive Neutron Cores". In: *Phys. Rev.* 55 (4 Feb. 1939), pp. 374–381. DOI: `10.1103/PhysRev.55.374`. URL: `https://link.aps.org/doi/10.1103/PhysRev.55.374`.
TOV limit for neutron star before collapsing into a black hole.

[64] Chris Impey. *Astronomy - State of the Art - Stars.* 2014. URL: `https://www.slideshare.net/chrisimpey1/4-slidesstars`.
Core composition schema for massive stars at end of life.

[65] K. Langanke et al. "Electron Capture Rates on Nuclei and Implications for Stellar Core Collapse". In: *Physical Review Letters* 90.24 (June 2003). ISSN: 1079-7114. DOI: `10.1103/physrevlett.90.241102`. URL: `http://dx.doi.org/10.1103/PhysRevLett.90.241102`.
Electron capture mechanisms in CCSN.

[66] Chris Sullivan et al. "The sensitivity of Core-Collapse Supernovae to nuclear electron capture". In: *The Astrophysical Journal* 816.1 (Dec. 2015), p. 44. ISSN: 1538-4357. DOI: `10.3847/0004-637x/816/1/44`. URL: `http://dx.doi.org/10.3847/0004-637X/816/1/44`.
Electron capture mechanism in CCSN and its sensitivity to the different models.

[67] Hans-Thomas Janka. "Neutrino Emission from Supernovae". In: *Handbook of Supernovae.* Springer International Publishing, 2017, pp. 1575–1604. ISBN: 9783319218465. DOI: `10.1007/978-3-319-21846-5_4`. URL: `http://dx.doi.org/10.1007/978-3-319-21846-5_4`.
CCSN neutrino emission and CCSN steps.

[68] K. Hirata et al. "Observation of a neutrino burst from the supernova SN1987A". In: *Phys. Rev. Lett.* 58 (14 Apr. 1987), pp. 1490–1493. DOI: `10.1103/PhysRevLett.58.1490`. URL: `https://link.aps.org/doi/10.1103/PhysRevLett.58.1490`.
Neutrino detection of SN1987A by the Kamiokande detector.

[69] R. M. Bionta et al. "Observation of a neutrino burst in coincidence with supernova 1987A in the Large Magellanic Cloud". In: *Phys. Rev. Lett.* 58 (14 Apr. 1987), pp. 1494–1496. DOI: `10.1103/PhysRevLett.58.1494`. URL: `https://link.aps.org/doi/10.1103/PhysRevLett.58.1494`.
Neutrino detection of SN1987A by the IMB detector.

[70] R.V. Novoseltseva, M.M. Boliev, and I.M. et al. Dzaparova. "The search for neutrino bursts from supernovae with Baksan underground scintillation telescope." In: *Phys. Part. Nuclei* 47 (2016), pp. 968–974. DOI: `https://doi.org/10.1134/S1063779616060198`.
Neutrino detection of SN1987A by the Baskan detector.

[71] James M. Lattimer and F. Douglas Swesty. "A generalized equation of state for hot, dense matter". In: *Nuclear Physics A* 535.2 (1991), pp. 331–376. ISSN: 0375-9474. DOI: `https://doi.org/10.1016/0375-9474(91)90452-C`. URL: `https://citeseerx.ist.psu.edu/document?repid=rep1&type=pdf&doi=f868767049c047d232cc05e4adb90201964eae86`.
Article presenting the Lattimer-Swesty EoS for CCSN.

[72] H. Shen et al. "Relativistic equation of state of nuclear matter for supernova and neutron star". In: *Nuclear Physics A* 637.3 (July 1998), pp. 435–450. ISSN: 0375-9474. DOI: `10.1016/s0375-9474(98)00236-x`. URL: `http://dx.doi.org/10.1016/S0375-9474(98)00236-X`.
Article presenting the Shen EoS for CCSN.

[73] P -G Reinhard. "The relativistic mean-field description of nuclei and nuclear dynamics". In: *Reports on Progress in Physics* 52.4 (Apr. 1989), p. 439. DOI: `https://iopscience.iop.org/article/10.1088/0034-4885/52/4/002/pdf`. URL: `https://link.springer.com/article/10.1007/BF02845972`.
Article presenting the RMF theory used by the LS EoS.

[74] N.H. March. "The Thomas-Fermi approximation in quantum mechanics". In: *Advances in Physics* 6.21 (1957), pp. 1–101. DOI: `https://doi.org/10.1080/00018735700101156`.
Article presenting the Thomas-Fermi approximation used by the LS EoS.

[75] A. W. Steiner, M. Hempel, and T. Fischer. "Core-Collapse Supernova equations of state based on neutron star observations". In: *The Astrophysical Journal* 774.1 (Aug. 2013), p. 17. ISSN: 1538-4357. DOI: `10.1088/0004-637x/774/1/17`. URL: `http://dx.doi.org/10.1088/0004-637X/774/1/17`.
Article presenting the SFHo (Steiner, Fischer, and Hempel) EoS.

[76] Adam Burrows, David Radice, and David Vartanyan. "Physical, numerical, and computational challenges of modeling neutrino transport in core-collapse supernovae". In: *Living Reviews in Computational Astrophysics* 6.1 (2020), p. 4. DOI: `10.1007/s41115-020-00010-8`. URL: `https://doi.org/10.1007/s41115-020-00010-8`.
Neutrino transport model in CCSN.

[77] Irene Tamborra et al. "Neutrino emission characteristics and detection opportunities based on three-dimensional supernova simulations". In: *Physical Review D* 90.4 (Aug. 2014). ISSN: 1550-2368. DOI: `10.1103/physrevd.90.045032`. URL: `http://dx.doi.org/10.1103/PhysRevD.90.045032`.
Tamborra model for CCSN neutrino: explanation of the SASI.

[78] Alessandro Mirizzi et al. "Supernova Neutrinos: Production, Oscillations and Detection". In: *La Rivista del Nuovo Cimento* 39.102 (Feb. 2016), pp. 1–112. ISSN: 0393697X, 0393697X. DOI: `10.1393/ncr/i2016-10120-8`. URL: `https://doi.org/10.1393/ncr/i2016-10120-8`.
Bollig model for CCSN neutrino: explanation of the ray-by-ray-plus approximation for multidimensional treatment.

[79] MacKenzie L. Warren et al. "Constraining Properties of the Next Nearby Core-collapse Supernova with Multimessenger Signals". In: *The Astrophysical Journal* 898.2 (July 2020), p. 139. ISSN: 1538-4357. DOI: `10.3847/1538-4357/ab97b7`. URL: `http://dx.doi.org/10.3847/1538-4357/ab97b7`.
Warren model for CCSN neutrino: explanation of the AMR.

[80] Amanda L. Baxter et al. *SNEWPY: A Data Pipeline from Supernova Simulations to Neutrino Signals.* 2021. arXiv: `2109.08188 [astro-ph.IM]`. URL: `https://arxiv.org/abs/2109.08188`.
Recapitulative table of CCSN models and their characteristics.

[81] Karolina Rozwadowska, Francesco Vissani, and Enrico Cappellaro. "On the rate of core collapse supernovae in the milky way". In: *New Astronomy* 83 (Feb. 2021), p. 101498. ISSN: 1384-1076. DOI: `10.1016/j.newast.2020.101498`. URL: `http://dx.doi.org/10.1016/j.newast.2020.101498`.
CCSN rate in the Milky Way.

[82] Alan W. McConnachie. "The observed properties of dwarf galaxies in and around the Local Group". In: *The Astronomical Journal* 144.1 (2012), p. 4. DOI: `10.1088/0004-6256/144/1/4`. URL: `https://doi.org/10.1088/0004-6256/144/1/4`.
Local group documentation: list of clusters around the Milky Way. Table 2 gives the distance and Table 4 gives the mass of the clusters.

[83] Or Graur, Federica B. Bianco, and Maryam Modjaz. "A unified explanation for the supernova rate-galaxy mass dependence based on supernovae detected in Sloan galaxy spectra". In: *Monthly Notices of the Royal Astronomical Society* 450.1 (Apr. 2015), pp. 905–925. ISSN: 1365-2966. DOI: `10.1093/mnras/stv713`. URL: `http://dx.doi.org/10.1093/mnras/stv713`.
Detailed explanation of the dependency between the CCSN rate of a galaxy and its stellar mass.

[84] Timothy C. Licquia and Jeffrey A. Newman. "Improved estimates of the Milky Way's stellar mass and star formation rate from hierarchical Bayesian meta-analysis". In: *The Astrophysical Journal* 806.1 (June 2015), p. 96. ISSN: 1538-4357. DOI: `10.1088/0004-637x/806/1/96`. URL: `http://dx.doi.org/10.1088/0004-637X/806/1/96`.
Stellar mass of the Milky Way.

[85] *SuperNova Early Warning System (SNEWS2).* Accessed: 2025-08-10. 2025. URL: `https://snews2.org/`.
Website of the SNEWS.

[86] Ken'ichiro Nakazato et al. "Supernova neutrino light curves and spectra for various progenitor stars: from core-collapse supernova to proto-neutron star cooling." In: *The Astrophysical Journal Supplement Series* 205.1 (Feb. 2013), p. 2. DOI: `10.1088/0067-0049/205/1/2`. URL: `https://dx.doi.org/10.1088/0067-0049/205/1/2`.
Details the 2013 Nakazato model for CCSN.

[87] Jiaxi Liu. *Continuous Over-Threshold Integral (COTI) Waveform Reconstruction Algorithm Tutorial.* JUNO Collaboration, 2022. URL: `https://jupyter.ihep.ac.cn/ioLMytjlQo-6HX-qKD0deg`.
Explains how the COTI reconstruction method works.

[88] Yuyi Wang, Aiqiang Zhang, and Benda Xu. *Fast deconvolution method for waveform analysis.* JUNO CollaborationDepartment of Engineering Physics, Tsinghua University, 2023.
Explains how the deconvolution reconstruction method works.

[89] Marta Colomer Mollá, Amina Kathun, and Barbara Clerbaux. *Muons analysis with 4 months of JUNO commissioning data.* 2025.
Research on the effects of temporal and energy cut on the data runs of JUNO.

[90] Patrick J. Laub, Thomas Taimre, and Philip K. Pollett. *Hawkes Processes.* 2015. arXiv: `1507.02822 [math.PR]`. URL: `https://arxiv.org/abs/1507.02822`.
Explain the Hawkes processes.

[91] Huiling Li et al. *Real-time Monitor for the Next Core-collapse Supernova in JUNO.* Institute of High Energy Physics, Chinese Academy of Sciences and Tsinghua Uviversity, 2022.
Previous work on CCSN real-time monitor for JUNO.